ORNL/TM-2023/3115

Data-Driven Optimization of the Processing Window for 316H Components Fabricated Using Laser Powder Bed Fusion

Caleb Massey et al.

September 2023

M2CR-22OR0403061

OAK RIDGE National Laboratory

ORNL IS MANAGED BY UT-BATTELLE LLC FOR THE US DEPARTMENT OF ENERGY

ORNL/TM-2023/3115

Advanced Materials and Manufacturing Technologies Program

DATA-DRIVEN OPTIMIZATION OF THE PROCESSING WINDOW FOR 316H COMPONENTS FABRICATED USING LASER POWDER BED FUSION

Caleb Massey
Peeyush Nandwana
Holden Hyer
Selda Nayir
Josh Kendall
Chase Joslin
Ryan Duncan
David Collins
Tim Graening
Fred List III
Luke Scime
Zackary Snow
Amir Ziabari
Thomas Butcher
Ryan Dehoff

September 2023

M2CR-22OR0403061

Prepared by
OAK RIDGE NATIONAL LABORATORY
Oak Ridge, TN 37831
managed by
UT-BATTELLE LLC
for the
US DEPARTMENT OF ENERGY

under contract DE-AC05-00OR22725

CONTENTS

LIST OF FIGURES iv
LIST OF TABLES v
ABBREVIATIONS vii
ACKNOWLEDGMENTS viii
EXECUTIVE SUMMARY ix
1. INTRODUCTION 1
1.1 THE CHALLENGE OF QUALIFYING ADDITIVELY MANUFACTURED COMPONENTS 1
1.2 A MULTI-INSTITUTIONAL APPROACH TO OPTIMIZING LASER POWDER BED FUSION 316H 2
2. MATERIALS AND METHODS 3
2.1 FEEDSTOCK MATERIAL AND AVAILABLE AM UNITS 3
2.2 DESIGN OF EXPERIMENTS 5
2.3 CHARACTERIZATION METHODS 9
2.3.1 In Situ Data Analysis 10
2.3.2 X-ray Computed Tomography Data Analysis 12
2.3.3 Microscopy and Mechanical Testing 15
3. RESULTS AND DISCUSSION 18
3.1 THE USE OF IN SITU DATA AS A QUALITY ASSURANCE TOOL 18
3.2 POROSITY ANALYSIS 20
3.2.1 Concept Laser Builds 20
3.2.2 Renishaw Builds 24
3.3 FACTORS AFFECTING MICROSTRUCTURE 30
3.3.1 Effect of Composition 30
3.3.2 Effect of Energy Density 34
3.3.3 Effect of Build Geometry 37
3.3.4 Ramifications on Mechanical Properties 38
4. FUTURE WORK 41
4.1 FUTURE OPTIMIZATION AND ROUND-ROBIN TESTING 41
4.2 LARGER BUILDS FOR CAMPAIGN TESTING 41
5. REFERENCES 43
Appendix A: PRINTING PARAMETERS AND POROSITY MEASUREMENTS 45

LIST OF FIGURES

Figure 1. Schematic showing available and printed powder/machine combinations at each of the three national laboratories engaged in LPBF process optimization. 4
Figure 2. Visual representations of (a, b) factorial and (c) central composite designs (CCDs). 5
Figure 3. Schematic showing design philosophy for Concept Laser DOE prints. 6
Figure 4. Examples of (a) concept laser build and (b) a Zeiss specimen with labeled features of interest. 8
Figure 5. Sequential filtering framework used to optimize processing conditions for 316L/H prints. 9
Figure 6. Representative examples of each of the five data modalities captured on a given layer for the Renishaw AM400. 11
Figure 7. Breakdown of the high-throughput rapid automated characterization process developing under the AMMT Program. 12
Figure 8. Procedure from scanning to analysis. 13
Figure 9. ORNL reconstruction (top) of a 20 min scan of Zeiss metal part made of 316H against standard reconstruction (bottom). 14
Figure 10. Kakapo segmentation vs. standard segmentation on CAD-DLMBIR reconstruction. 14
Figure 11. SSJ3 (left) and SST (right) nominal geometries; both are flat dog bone–type specimens. 16
Figure 12. Comparison of representative SSJ3 (green) and SST (blue) tensile response for various wrought nuclear-relevant materials included. 17
Figure 13. Tensile specimen harvesting strategy for SSJ3 and SST specimens. 17
Figure 14. 2D prevalence maps of three classes of characteristic anomalies identified through in situ data collection in three Concept Laser M2 builds (DOE1, DOE2, and DOE5). 19
Figure 15. Comparison of all 316L (AM316L-1) and 316H (AM316H-3) specimen porosity using the Kakapo segmentation algorithm for XCT data. 20
Figure 16. Comparison of all 316L (AM316L-1) and 316H (AM316H-3) specimen porosity (Kakapo segmentation) with aggregated print quality as measured by in situ data. 21
Figure 17. Optical micrographs of (a, b) 316L and (c, d) 316H samples given as (a, d) high magnification and (b, c) entire cross-section images. 22
Figure 18. Reconstructed pore size distribution bulk and fins section of (a) 316L and (b) 316H builds produced with 43 J/mm^3, 71 J/mm^3, and 135 J/mm^3 energy densities. 23
Figure 19. General mean bulk porosity trends for 316L (AM316L-2) and 316H (AM316H-3) builds performed on the Renishaw. 24
Figure 20. General mean bulk porosity trends for 316L (AM316L-2) and 316H (AM316H-3) build PB performed on the Renishaw. 26
Figure 21. General mean bulk porosity trends for 316L (AM316L-2) and 316H (AM316H-3) build PG performed on the Renishaw. 26
Figure 22. The statistical effect of various input parameters on porosity in Renishaw printed specimens. 28

Figure 23. Normalized stability values for all printed 316L (AM316L-2) and 316H (AM316H-3) samples printed using the Renishaw. 28
Figure 24. Histograms detailing the values for (a) laser power, (b) point distance, and (c) dwell time found in the Zeiss samples with the most stable parameter combinations for both SS316L and SS316H. 29
Figure 25. Optical images of grain structures revealed through electrolytic etching of 316L (AM316L-1, top) and 316H (AM316H-3, bottom) specimens printed with different energy densities on the concept laser. 30
Figure 26. SEM+EDS analysis revealing characteristic elemental segregation in fish scale cellular structure in 316L (AM316L-1) samples printed on the concept laser. 32
Figure 27. SEM+EDS analysis revealing characteristic elemental segregation in fish scale cellular structure in 316H samples printed on the concept laser. 32
Figure 28. Powder composition of 316L, 316H, and Renishaw prints was overlayed using Scheil–Gulliver methods to predict the fast solidification phases. 33
Figure 29. Variation of grain structure and orientation as a function of increasing energy density for 316L and 316H specimens printed on the concept laser within regions of acceptable porosity. 35
Figure 30. Variation of grain structure and orientation as a function of increasing energy density for 316H (AM316H-3) specimens printed on the Renishaw. 36
Figure 31. STEM+EDS maps of Cr enrichment along cells in (a) M2B5-P24, (b) M2B5-P35, and (c) M2B5-P7. 36
Figure 32. Grain morphology and texture changes within a single 316H (AM316H-3) sample printed on the concept laser (energy density ~52 J/mm3). 37
Figure 33. Collection of tensile results of 316L and 316H builds printed on both the concept laser and Renishaw tested using SSJ3 and SST tensile specimen geometries. 39
Figure 34. Subsized mechanical property data from SST specimens machined from the body of Zeiss specimens in the vertical (build direction) and horizontal (transverse direction) for samples printed with increasing energy density on the Concept Laser M2 from 316H powder (AM316H-3). 39
Figure 35. Hardness results for bulk and fin regions were given for (a) 316L and (b) 316L builds. 40
Figure 36. Optical images of build "Tensile Blocks 01" from the (a) top view and (b) isometric view. 42

LIST OF TABLES

Table 1. The ASTM specifications [11] for 316SS and the measured feedstock powder chemistry for the powders used in this study. 3
Table 2. Parameter ranges investigated within each build of the Concept Laser DOE 6
Table 3. Parameter ranges investigated within each build of the Renishaw DOE. 8
Table 4. Range of acceptable values for the most influential parameters laser power, point distance, dwell time, and hatch spacing when printing SS316L or SS316H. 30
Table 5. Material allocations from initial large builds 42

Table A-1: Complete list of concept laser print parameters A-1
Table A-2: Complete list of Renishaw print parameters A-3
Table A-3: XCT porosity analysis summary (Concept Laser M2) A-6
Table A-4: XCT porosity analysis summary (Renishaw) A-10

ABBREVIATIONS

AF	austenitic-ferritic mode of solidification
AM	additive manufacturing
AMMT	Advanced Materials and Manufacturing Technologies
ANL	Argonne National Laboratory
ASME	American Society of Mechanical Engineers
ASTM	American Society for Testing and Materials
CAD-DLMBIR	Computer-Aided Design Deep Learning Model-Based Image Reconstruction
CCD	central composite design
DOE	design of experiments
DMSCNN	dynamic multilabel segmentation convolutional neural network
EBSD	electron backscatter diffraction
EDM	electrical discharge machining
EDS	energy-dispersive x-ray spectroscopy
FY	fiscal year
FIB	focused ion beam
HV	Vickers hardness
LANL	Los Alamos National Laboratory
LPBF	laser powder bed fusion
MDDC	multidimensional data correlation
MTEX	Materials TEXture Analysis Toolbox
NIR	near infrared
ORNL	Oak Ridge National Laboratory
SEM	scanning electron microscope
SSJ3	Subsize Specimen 3 (Japan designation)
SST	Subsize Specimen Teeny
SS	stainless steel
SS316H	Stainless Steel 316H
SS316L	Stainless Steel 316L
SSJ3	Specimen Support for Japanese-3
TCR	Transformational Challenge Reactor
XCT	x-ray computed tomography

ACKNOWLEDGMENTS

This research was sponsored by the US Department of Energy Office of Nuclear Energy's Advanced Materials and Manufacturing Technologies Program under contract DE-AC05-00OR22725 with UT-Battelle LLC. The authors thank Dr. David Hoelzer and Mr. Ben Garrison for their thoughtful review of this report before publication. Additional appreciation is given to Kevin Hanson and Cody Taylor for assistance with specimen heat treatments and sectioning. The microscopy assistance of both Andres Marquez Rossy and Amy Godfrey helped this team tremendously. Finally, the authors acknowledge the hard work of the metallography team, including Jim Horenburg and Daniel Newberry.

EXECUTIVE SUMMARY

The Advanced Materials and Manufacturing Technologies Program is focused on accelerating the development and deployment of advanced materials and components fabricated via additive manufacturing with a specific focus on laser powder bed fusion (LPBF). As an initial case study, the program has selected 316H stainless steel (SS) as an initial material around which to develop a code case development strategy. This strategy involves two parallel approaches: (1) an equivalency approach whereby round-robin testing across multiple collaborating laboratories demonstrates repeatability in processing and direct comparisons with conventional wrought 316H material and (2) a revolutionary approach to code qualification combining in situ data collection and high-fidelity modeling to capture, predict, and bound the performance of LPBF 316HSS components. As part of this campaign, this work package has initiated an extensive process optimization campaign across three laboratories, each printing variations of LPBF 316HSS using three different LPBF units (Concept Laser, EOS, and Renishaw).

In FY23, ORNL has focused on unique experimental designs spanning wide ranges in energy inputs and turning knobs such as scan speed, laser power, hatch spacing, layer thickness, spot size, scan rotation, and more. On the Concept Laser M2, 72 different combinations of processing variables were investigated with duplicate samples and different powder compositions. In total, 252 samples were printed with combined in situ sensing data. A parallel design of experiments was conducted on the Renishaw AM400 with an additional 390 printed specimens for analysis. All 642 miniature specimens, each with unique features included in each print to capture geometry-related heterogeneity, were subjected to high-throughput x-ray computed tomography (XCT) analysis to enable the downselection of specific processing parameters of interest. Then, using electrical discharge machining (EDM), miniature tensile specimens were extracted for mechanical testing and microscopy investigations.

From the analysis performed in FY23, it was found that powder composition drastically affects the resulting microstructure and mechanical performance of 316SS. Specifically, changing from 316L to 316HSS powder results in a wide range of grain sizes with varying degrees of preferred grain orientation, which increases as a function of energy density. It was also found that due to stored heat in thin fin–type features, large microstructural differences can be seen within one part printed with one set of processing parameters. These variations in microstructure features, including grain size, the nanoscale dislocation structure, and grain texture, will all affect the irradiation performance and high-temperature mechanical performance of LPBF 316HSS parts.

Two sets of concept laser processing parameters, spanning both refined and columnar grain structures, were scaled to print larger 316H builds for campaign testing (high-temperature creep and irradiation). In addition, at least two optimized processing parameter sets were identified for the Renishaw AM400 for round-robin testing in FY24 with Argonne National Laboratory. Future work includes printing samples using identical parameters identified by partner institutions, providing material for corrosion and high-temperature mechanical testing, and continuing evaluations of heterogeneity in larger printed parts.

1. INTRODUCTION

1.1 THE CHALLENGE OF QUALIFYING ADDITIVELY MANUFACTURED COMPONENTS

As part of the Advanced Materials and Manufacturing Technologies (AMMT) Program's mission to lead innovation in both materials and manufacturing technologies for nuclear energy applications, one of the key goals is to establish a rapid qualification framework for relevant additively manufactured materials to be deployed in advanced reactors. This is a grand challenge because to date there are only six materials approved for use in Section III, Division 5 of the ASME Boiler and Pressure Vessel Code overseeing the realm of elevated temperature nuclear structural materials. In addition, current qualification approaches, even for a conventionally produced material, take a decade to fully implement. Therefore, a rapid qualification of new additively manufactured materials is necessary to accelerate their nuclear application and enable advanced reactors to deploy in a more reasonable timeframe.

Laser powder bed fusion (LPBF) has been identified as a key additive manufacturing (AM) technology to fabricate components for nuclear applications owing to its ability to make high-resolution near-net-shape components. However, its widespread use is limited by the variability in microstructure and material properties that can be a result of the powder feedstock [1], process parameters [2], geometry [3], or the AM system used [4]. In the case of LPBF, the material undergoes layer-by-layer deposition and is fused by small melt pools, each of which undergoes very high cooling rates of the order of 10^5−10^6 K/s [5]. Such repeated thermal cycles result in heterogeneous hierarchical microstructures but can also enable superior properties for AM material compared with their conventionally processed counterparts. In the case of 316LSS, a low–interstitial content variant of 316SS (carbon <0.04 wt %), LPBF results in a dislocation substructure that gives comparable strength and significantly higher elongation to failure compared with conventional 316LSS, especially at room temperature [6, 7]. At the same time, LPBF also causes significant partitioning of chromium and nickel, also called *solute partitioning*, that can potentially affect other properties such as creep and corrosion in the extreme environments experienced in nuclear applications [8]. A homogenizing heat treatment can be used to minimize the extent of solute partitioning but will also annihilate the beneficial dislocation substructures that may serve as potential defect sinks during irradiation [9]. Similarly, for 316HSS that contains a higher amount of carbon in the range 0.04–0.1 wt %, a direct aging heat treatment can be used to obtain a high number density of finer carbides on the dislocation structure from LPBF compared with a conventional homogenization and aging treatment. For example, in the case of grade 300 maraging steel, precipitation-strengthened material such as 316HSS, direct aging has been shown to be beneficial [10]. Therefore, it is important to control the variables such as feedstock chemistry and process settings such that repeatable material properties are obtained in as-fabricated condition for 316SS.

In short, the spatial variations in microstructure create heterogeneities in LPBF components that invalidate the fundamental premise of conventional code qualification (i.e., that a series of select specimens harvested from a larger heat of material will provide representative performance metrics for all remaining portions of the same part). It follows that a fundamentally different qualification approach is needed for additively manufactured components. Current approaches to ameliorate this issue include postprocessing to minimize heterogeneities and/or the use of either modeling or in situ data to attest to the quality of additively manufactured parts.

This work explores ways to establish an optimal processing window for LPBF materials with a specific focus on one popular alloy—316H stainless steel (SS)—as a case study. The results of this process optimization aim to provide input toward prerequisite decisions necessary for a code qualification campaign, to inform modeling efforts to predict artifacts associated with the LPBF technique, and to develop processing-structure-property-performance relationships necessary to predict part performance.

1.2 A MULTI-INSTITUTIONAL APPROACH TO OPTIMIZING LASER POWDER BED FUSION 316H

Three national laboratories, including Oak Ridge National Laboratory (ORNL), Argonne National Laboratory (ANL), and Los Alamos National Laboratory (LANL), are collaborating to develop a machine-agnostic methodology for 316SS process optimization. Specifically, the three labs are printing various 316H stainless steel powder compositions on three different additive manufacturing units. Both ORNL and ANL have access to a Renishaw AM400, ORNL and LANL have access to an EOS 290, and ORNL is continuing to use the Concept Laser M2 unit that was heavily leveraged during the prior Transformational Challenge Reactor (TCR) campaign.

Although the overarching goal of this process optimization work package is the same for all three labs, each lab has the freedom to pursue its own design of experiments in this initial fiscal year. This way, confirmation bias cannot affect the outcome of these parallel optimization initiatives, and each lab is free to develop its own "optimal" printing parameters. This approach was purposeful because it is first important to evaluate whether two parallel teams (or vendors if applied in the industrial space), given the same feedstock powder and LPBF unit, will co-optimize to the same set of optimized parameters or whether a more rigid framework is necessary to prescribe. Ideally, the methodology used for process optimization should be machine agnostic to avoid difficulties in translating machine-specific processing parameters within general engineering standards.

As such, this report focuses specifically on ORNL's approach to optimize 316H processing conditions using two different additive manufacturing units. For the purposes of this work, the definition of *optimized* comprises the envelope of most influential processing parameters that results in minimized porosity (<0.1% in the as-printed condition), minimized porosity spread within complex parts (measured using the standard deviation of porosity in various segmented locations within a printed part), and a predictable microstructure conducive for use in components with a prescribed irradiation temperature, dose, and loading condition.

2. MATERIALS AND METHODS

2.1 FEEDSTOCK MATERIAL AND AVAILABLE AM UNITS

The powder feedstock chemistry of 316SS-L and H powders procured from Praxair Surface Technologies Inc., Renishaw, and Powder Alloy Corporation is summarized in Table 1 and compared with the ASTM specifications. The powder feedstock chemistry ranges used for LPBF are based on compositions developed for conventionally processed material, such as ASTM International's ASTM A240 specification for rolled 316SS plate material [11]. The powders had a nominal size distribution of 15–45 μm.

Of the different powders used across the three laboratories, powder AM316L-1 and AM316H-3 were printed in FY23 on the Concept Laser M2, while AM316L-2 and AM316H-3 were printed on the Renishaw AM400. The Concept Laser M2 is an LPBF printer with a total build volume of 245 mm × 245 mm × 350 mm. This system has two 400 W continuous lasers that can each reach the entire print area. The build chamber is filled with Ar to provide an inert printing atmosphere. The other system used in this work is a Renishaw AM400 unit, which uses a pulsed 400 W laser across the same build volume used for the concept laser. These prints are also performed under inert Ar atmosphere.

As illustrated in Figure 1, not all powders were printed on all units or at all collaborative institutions, but there is overlap to ensure effective interlaboratory collaboration. As of the writing of this report, power/unit combinations in green have been printed, while those in black are possible to incorporate into the future work scope.

Table 1. The ASTM specifications [11] for 316SS and the measured feedstock powder chemistry for the powders used in this study. The compositions are in weight percent based on reported data from Dirats Laboratories.

Material		316LSS	316LSS	316HSS	316HSS	316HSS	ASTM Specification
Vendor		Praxair*	Renishaw**	Praxair	Praxair	PAC	
Lot #		30, 31 & 32	21D0502	2	3	AMP316H1001E	
Designation		AM316L-1	AM316L-2	AM316H-2	AM316H-3	AM316H-4	
Composition (wt %)	Fe	balance	balance	balance	balance	balance	balance
	Cr	16.86	16.76	17	17	16.94	16.0–18.0
	Ni	12.07	12.5	11.73	11.98	10.88	10.0–14.0
	Mo	2.5	2.29	2.56	2.44	2.23	2.00–3.00
	Mn	1.1	0.48	1.13	1.06	1.02	<2.00
	Si	0.48	0.62	0.48	0.15	0.37	<1.00
	Al	0	0.01	0.01	0.02	0.01	n/a
	N	0.006	0.085	0.01	0.012	0.05	n/a
	O	0.056	0.044	0.034	0.03	0.048	n/a
	P	0.005	0.016	0.005	0.006	0.031	<0.045
	S	0.005	0.006	0.003	0.003	0.001	<0.03
	C	0.005	0.014	0.06	0.08	0.043	<0.03 (L) 0.04–0.10 (H)
* Measured composition of a mixture of three prior heats of powder remaining from TCR program							
** Full Chemical Analysis of Powder of Renishaw 316L powder is not available on the date of reporting, so the average composition of 10 printed parts is used as an approximation							

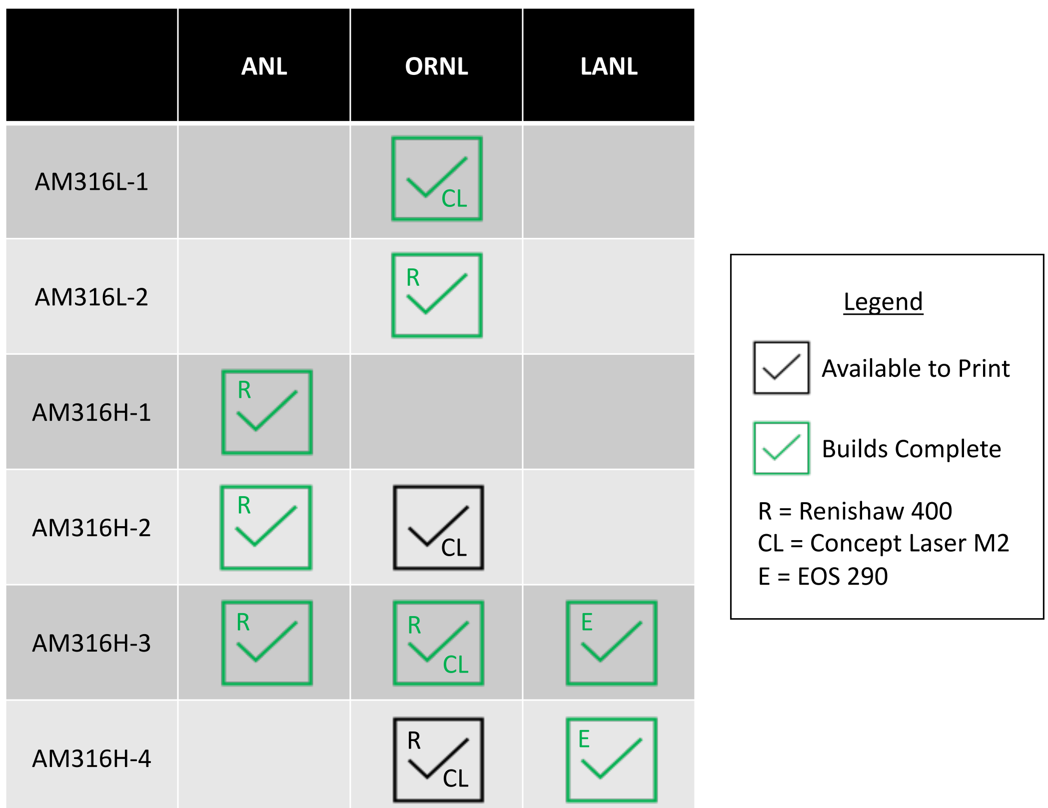

Figure 1. Schematic showing available and printed powder/machine combinations at each of the three national laboratories engaged in LPBF process optimization.

2.2 DESIGN OF EXPERIMENTS

Design of experiments (DOE) is a statistical method used for screening and downselecting parameters for a given process. Using DOE for parameter optimization removes potential human bias and complete randomization (i.e., guess and check), giving the user a starting point to examine and learn what parameters are most influential. The most common DOE method is a factorial design in which given parameters are established, each having variable levels, often bounded by only a single high and low value, taking the form of L^k where the number of runs is determined by the number of factors (k) to be varied and by (L) the number of levels the user desires (typically 2, ergo 2^k). A visual interpretation of a factorial design is shown in Figure 2(a, b). For example, if only two factors are being study, a high and low value are set by the user, resulting in four possible combinations, 2^2, of parameters, as shown in Figure 2(a). As one would imagine, adding an additional factor would double the number of runs, 2^3, as shown in Figure 2(b).

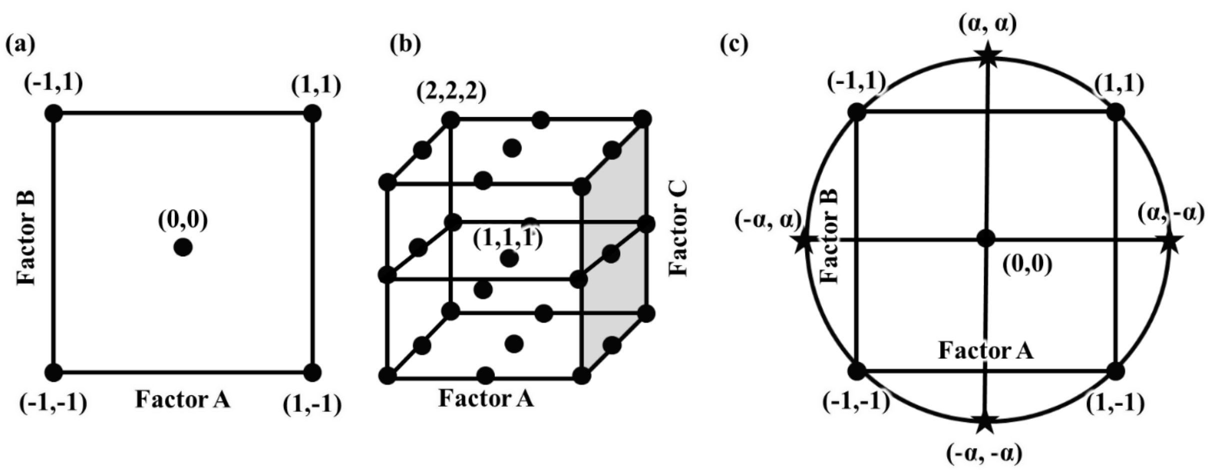

Figure 2. Visual representations of (a, b) factorial and (c) central composite designs (CCDs).

Factorial designs are useful but only evaluate the effects between two different levels, resulting in only a linear regression type fitting to any response data. A central composite design (CCD) is a modified form of the factorial design that explores the curvature of a factorial design by inscribing the factorial design in a circle, as shown in Figure 2(c). Curvature allows for additional runs to be explored at parameters above and below the set 2-level (i.e., high and low) conditions in the factorial design while still maintaining an orthogonal design (independence between specific variables). For each factor explored, the users set a high and low value. The CCD then computes the curvature points (α) based on factorial design:

$$\alpha = [2^k]^{\frac{1}{4}}. \tag{1}$$

The curvature lets the user understand interactions between the desired parameters more easily and detect differences over a broader range of values. Therefore, a CCD strategy was used for all the DOE builds on the Concept Laser and Renishaw units at ORNL.

The AM community has historically struggled to develop a unified measure enabling the comparison of parts printed using different processing parameters. This is because of the significant number of available knobs one can turn during the printing process and variability in solidification behavior from material to material. The most influential parameters include laser power, scan speed, hatch spacing, layer thickness, spot size, scan rotation, directing scan path, and more. One measure that has shown promise in relating some of the more parameters is the volumetric energy density (E_d), which is defined as

$$E_d = \frac{P}{v \times h \times t}, \tag{2}$$

where P is the laser powder, v is the beam velocity, h is the hatch spacing, and t is the layer thickness.

For the concept laser builds, a simple CCD comprising builds of 18 different parameters spanning 3 major processing parameters—scan velocity, hatch spacing, and laser power—was developed. To potentially capture differences in part properties as a function of print location, the 18 specimens were duplicated on each build plate to provide replication of build parameters in the DOE. The design philosophy comprised an initial build spanning a wide range of volumetric energy density to identify a suitable region in which optimal parameters may exist. A second build was then designed with a narrower processing space in an attempt to potentially find additional processing regions that may have been overlooked by the larger parametric step size used in the initial DOE build. Finally, to confirm the results and to evaluate the outer feasible printing envelope, a final build was performed with an expanded design window. A schematic of this approach is shown in Figure 3.

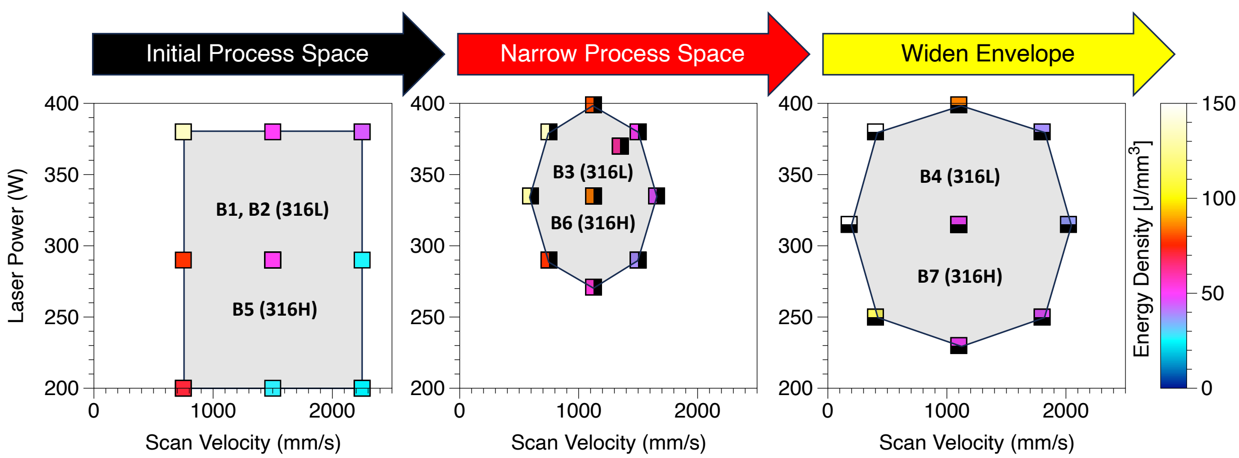

Figure 3. Schematic showing design philosophy for Concept Laser DOE prints.

Table 2. Parameter ranges investigated within each build of the Concept Laser DOE

Build	Power (W)		Hatch Space (mm)		Velocity (mm/s)		Layer Thickness (um)	Spot Size (um)	Energy Density (J/mm^3)	
	Min	Max	Min	Max	Min	Max			Min	Max
(DOE1, DOE2) 316L, (DOE5) 316H	200	380	75	125	750	2250	50	125	14	135
(DOE3) 316L, (DOE6) 316H	271	399	70	105	595	2021	50	125	39	135
(DOE4) 316L, (DOE7) 316H	230	399	52.1	117.9	179	2021	50	125	25	414

Since the Concept Laser was used to quickly iterate through parameters based on previous work from TCR, a larger DOE study was performed on the Renishaw to study the effects of other influential parameters besides the energy density terms (i.e., laser power, scan speed, hatch spacing, and layer thickness). Other influential parameters identified include the laser spot size, the width of each stripe that acts as a bounding area for rastering, the scan rotation between consecutive layers, and the offset between the hatch spacing between adjoining stripe patterns. Moreover, the Renishaw is equipped with a pulsed laser; therefore, the scan speed is calculated as a function of the laser jumping distance, known as *the point distance*, and the total dwell time of the laser at each point:

$$Scan\ Speed = \frac{Point\ Distance}{Dwell\ Time + Delay\ Time}. \tag{3}$$

Additionally, the delay time between jumps is accounted for in the scan speed, which is 10 µs for the Renishaw. Therefore, the point distance and dwell must be studied equivalently to study effects of scan speed.

Introducing eight unique factors into a CCD would propagate lots of error because each added factor can adversely affect others. Moreover, a CCD of that magnitude would require 250 unique sample combinations, which cannot possibly fit into one build, and separating the single CCD into multiple builds would add unknown error into the study (i.e., variability between prints, samples, etc.). Therefore, seven builds were designed, each varying four parameters, keeping the total number of sample combinations to 30. The linear variation of the energy density term, $E_d = P/v$, is often used in welding practices because these two parameters are the most influential toward the melt pool formation and solidification. Consequently, the most influential parameters in energy density, namely laser power, point distance, and dwell time, were varied in each build along with an additional parameter. The reason is that energy density terms could be related to other influential parameters in each build.

The input high/low values for each build, labeled *Processing A* (PA), through PG are reported in Table 3. A full table of all parameters used is available upon request but is omitted in this report for brevity. The first build, labeled as *PA*, was designed to be an extreme build, pushing the limits of the energy density parameters including the laser power, point distance, dwell time, and hatch spacing. Subsequent build PB was used to narrow down the window of these parameters to limit the number of extreme parameter combinations that may adversely affect neighboring samples, propagating uncertainty and error. Each consecutive build, PC to PG, was then processed with the same laser power, point distance, and dwell time values as used in PB.

Table 3. Parameter ranges investigated within each build of the Renishaw DOE. Also shown are the Renishaw recommended parameters for reference.

	Laser Power (W)		Point Distance (µm)		Dwell Time (µs)		Hatch Spacing (µm)		Layer Thickness (µm)		Energy Density (J/mm^3)		Spot Size (µm)	Stripe Width (mm)	Scan Rotation (°)	Hatch Offset (µm)
Study	Low	High	Low	High	Low	High	Low	High	Low	High	Low	High				
PA	75	375	55	10	10	190	10	190	50	50	10	428	70	5	67	60
PB	160	320	25	85	50	170	40	120	50	50	51	350	70	5	67	60
PC	160	320	25	85	50	170	20	60	20	60	64	437	70	5	67	60
PD	160	320	25	85	50	170	80	80	50	50	64	288	75-135	5	67	60
PE	160	320	25	85	50	170	80	80	50	50	64	288	70	1-9	67	60
PF	160	320	25	85	50	170	80	80	50	50	64	288	70	5	10-90	60
PG	160	320	25	85	50	170	80	80	50	50	64	288	70	5	67	20-100
Rec.	200		60		80		110		50		54		70	5	67	60

For all builds (Concept Laser and Renishaw), ORNL has adopted the use of a miniaturized specimen for high-throughput evaluations of process parameters and build geometry. This specimen, initially developed by Zeiss (and as such is termed *the Zeiss specimen* in this work), comprises a 15 mm diameter, 10 mm tall cylinder with various features printed atop it. These features, as illustrated in Figure 4, include vertical fins of various widths (0.5, 1, and 2 mm), inclined structures with various overhang angles (15°, 30°, and 45°), and vertical rods of various diameters (0.5, 1, 2, and 3 mm). This specimen thus provides a variety of complex geometries to probe variations in porosity and microstructure as a function of process variables.

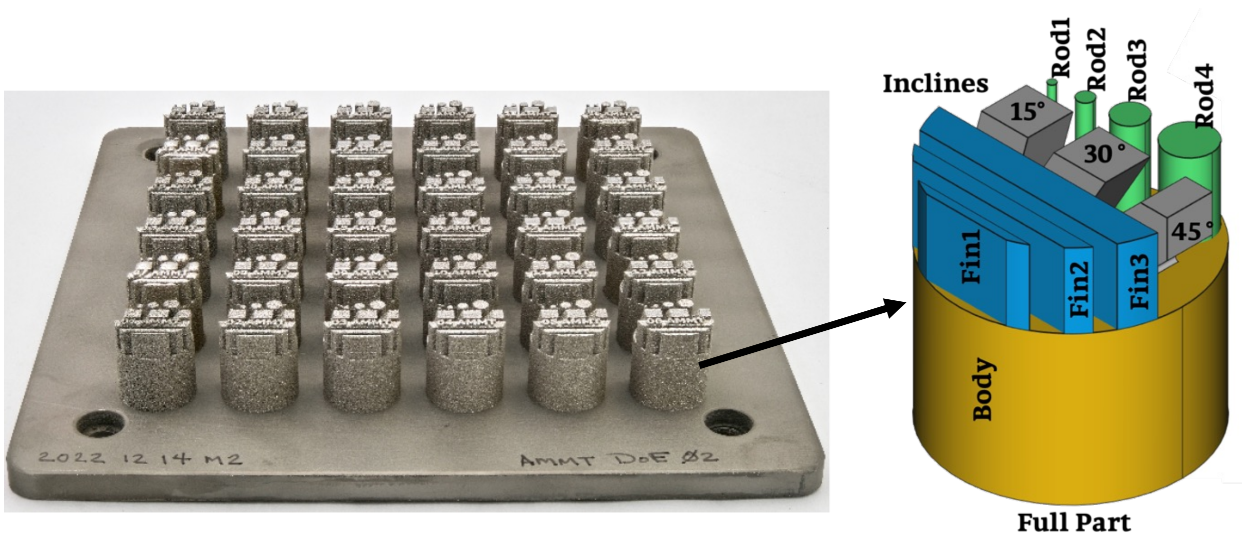

(a) (b)

Figure 4. Examples of (a) concept laser build and (b) a Zeiss specimen with labeled features of interest.

2.3 CHARACTERIZATION METHODS

The optimization framework used in this work involved three sequential characterization steps, as shown in Figure 5. First, in situ data were collected during builds (when possible) to ensure that the printed parts accurately represent the desired inputted print geometries. It is possible that during printing, an otherwise acceptable part may experience an artifact that could inadvertently affect downstream measurements used for part downselection. Thus, for a qualification campaign, it is prudent to use in situ data when possible to (1) identify builds that should be reperformed based on anomalous print behavior and to (2) identify parameters that produce the fewest artifacts during printing, thereby alluding to a potential processing window with stable print conditions.

Following in situ data filtering, high-throughput characterization in the form of x-ray computed tomography (XCT) is used to identify trends in porosity (part density) as a function of processing parameters. For samples with minimized part porosity and minimal spread in porosity between regions in each miniature Zeiss specimen, select specimens of interest are identified and sectioned for mechanical property evaluations and microscopic examination. In the following sections, the specific methods used in these sequential steps are described.

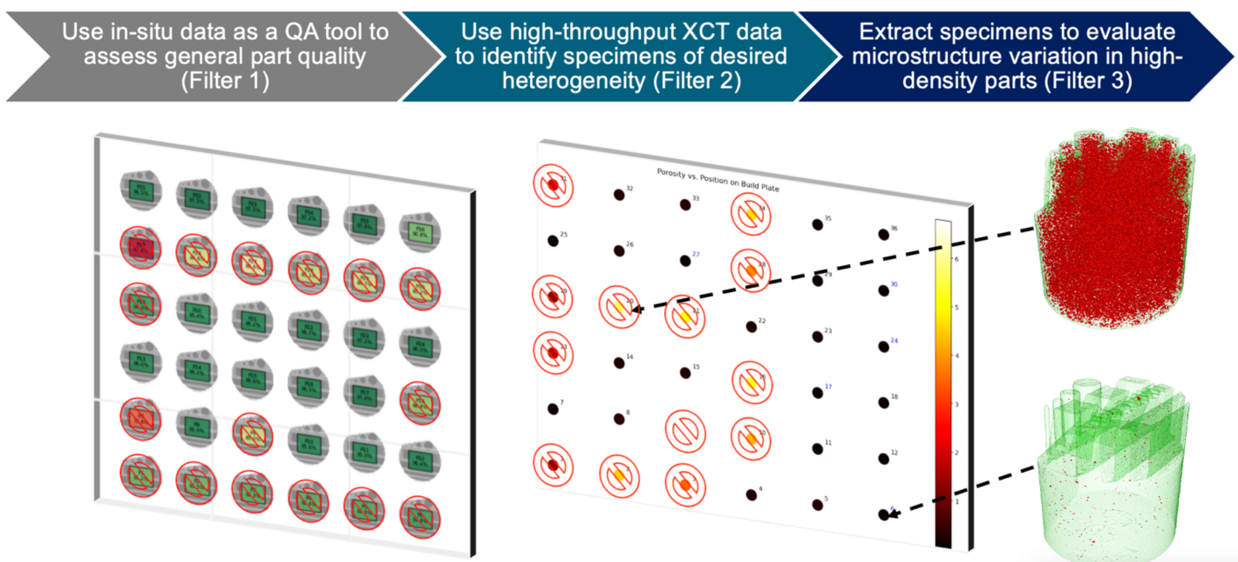

Figure 5. Sequential filtering framework used to optimize processing conditions for 316L/H prints.

2.3.1 In Situ Data Analysis

Peregrine is an ORNL-developed software tool designed to provide a comprehensive suite of data collection, analysis, and visualization capabilities for powder bed AM systems and is responsible for collecting and analyzing layer-wise imaging data for the LPBF printers used under the AMMT Program. In support of various AMMT work packages, a common sensor package for in situ monitoring data was installed on three ORNL LPBF machines: the Concept Laser M2, the Renishaw AM250, and the Renishaw AM400. This common sensor package, which includes a combination of high-resolution visible light images and temporally integrated near infrared (TI-NIR) images, will better allow comparisons of process stability and material quality across different builds, materials, LPBF machines, and printing facilities. The data generated by these sensors have been integrated into the Peregrine software tool to support ex situ characterization efforts.

Each of the above machines was instrumented with two cameras: a 20 MP visible light camera (Basler acA5472-17um) and a 4.2 MP NIR-sensitive camera (Pixelink PL-D734MU-NIR-T). The visible light camera is outfitted with a UV/NIR cutoff filter to protect the camera detector from the laser. Similarly, the NIR-sensitive camera has a narrow bandpass filter centered in the NIR range (808 nm ± 10 nm) as well as neutral density filters (OD ≈ 1.8) to prevent image saturation. The visible light captures a postmelt and a post-recoat image for each layer, while the NIR camera produces a video buffer that is dynamically analyzed at the end of a layer, producing three images engineered to extract relevant process dynamics for the layer. Representative examples of each of these data modalities are shown in Figure 6.

Data collected by each of the sensors described above can be used to train a dynamic multilabel segmentation convolutional neural network (DMSCNN), the deep learning model that forms the backbone of Peregrine’s analysis capabilities. A trained DMSCNN may be used to detect various anomaly classes observable from the multimodal sensor signature of a given layer. Common anomaly classes include successfully printed material, unmelted powder, spatter particles, recoater events, powder short feeding, sensor anomalies, and more, and analysis of the anomaly segmentation results may be used to improve understanding of anomalous behavior with the LPBF process. Additional details regarding Peregrine, the Digital Tool, and the sensor upgrades can be found in the FY23 AMMT report on the multidimensional data correlation (MDDC) framework (M3CR-22OR0403051).

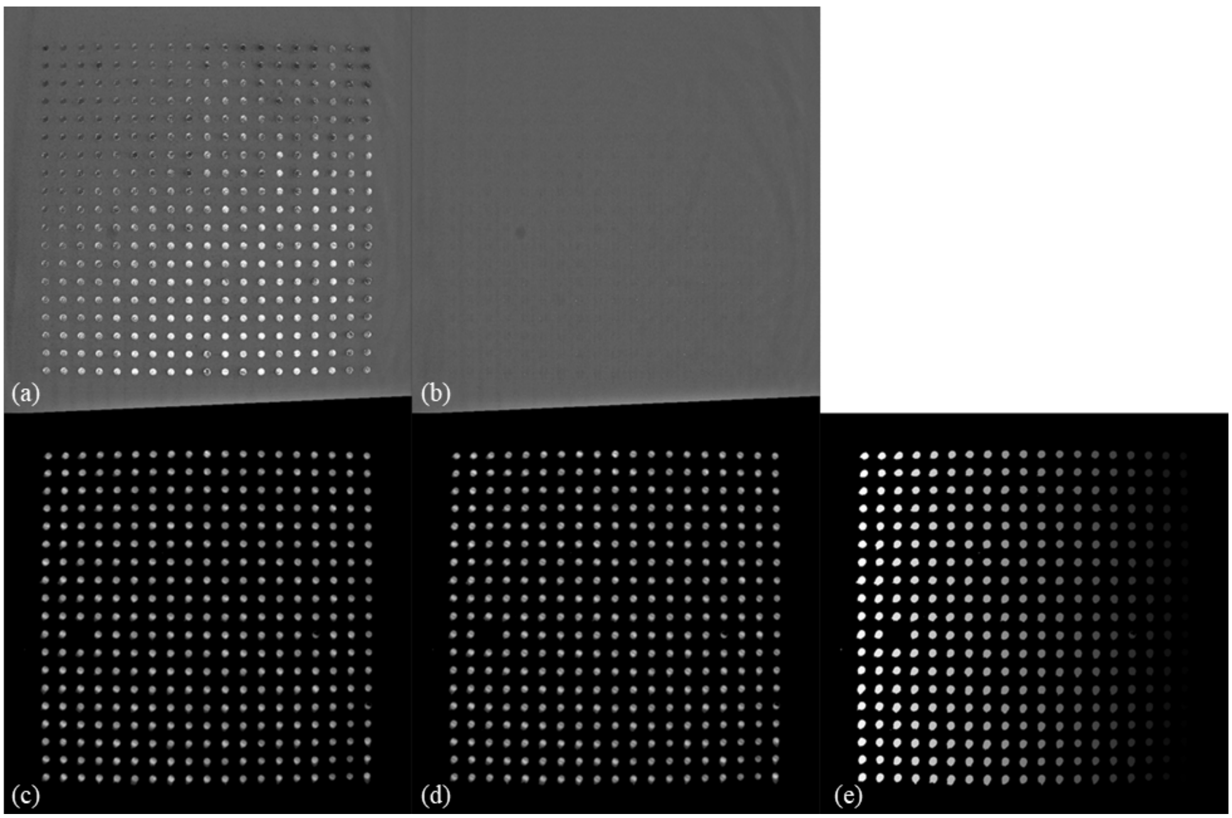

Figure 6. Representative examples of each of the five data modalities captured on a given layer for the Renishaw AM400. The visible camera collects postmelt (a) and post-recoat (b) snapshots, while the NIR camera produced three temporally integrated images that summarize process dynamics: sum (c), max (d), and argmax (e).

2.3.2 X-ray Computed Tomography Data Analysis

After printing the parts with various process parameters on a build plate, they were machined with EDM and scanned in the Zeiss's Metrotom 800 x-ray CT scanner (tube voltage of 225 kV, tube power of 500 W, and voxel size of 17.28 μm) in the characterization lab at the MDF. Figure 7 provides an overview of the automated high-throughput characterization process, which has been developing under *Automated, High-Throughput Materials Characterization Techniques work package* in the AMMT Program (see report M3CR-22OR0406012 for more information). To enable high-throughput characterization, each sample must be scanned, reconstructed, and analyzed (Figure 8) very quickly. To that end, deep learning–based tools are being developed and fine-tuned to accelerate characterization of the dense metal components such 316L and 316H, which traditionally may take several hours to produce a decent image for 15 mm parts.

Specifically, CAD-DLMBIR reconstruction in the Simurgh framework [12, 13], developed at ORNL under the DOE TCF program and a CRADA with Zeiss, and the Kakapo segmentation algorithm (based on a modified U-Net [14] architecture) partially developed under the AMMT Program along with other programs at ORNL were used to perform image reconstruction, artifact reduction, and segmentation on data that are acquired significantly faster than setting used commonly for such dense materials.

For instance, for Zeiss parts made out of 316L and 316H instead of using a 2 h scan per part, each part was scanned for only 20 min. In Figure 9, a comparison between the DL-based reconstruction and standard reconstruction of a 20 min scan highlights the superior quality that can be achieved.

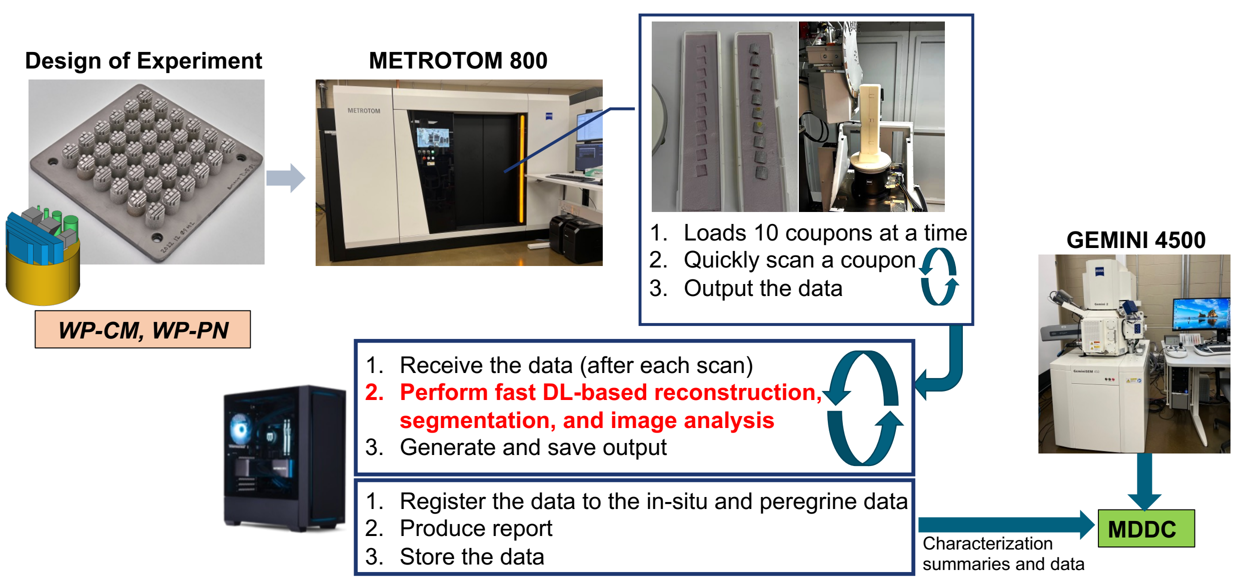

Figure 7. Breakdown of the high-throughput rapid automated characterization process developing under the AMMT Program. Abbreviations are work package Caleb Massey (WP-CM), work package Peeyush Nandwana (WP-PN), deep learning (DL), and multidimensional data correlation (MDDC).

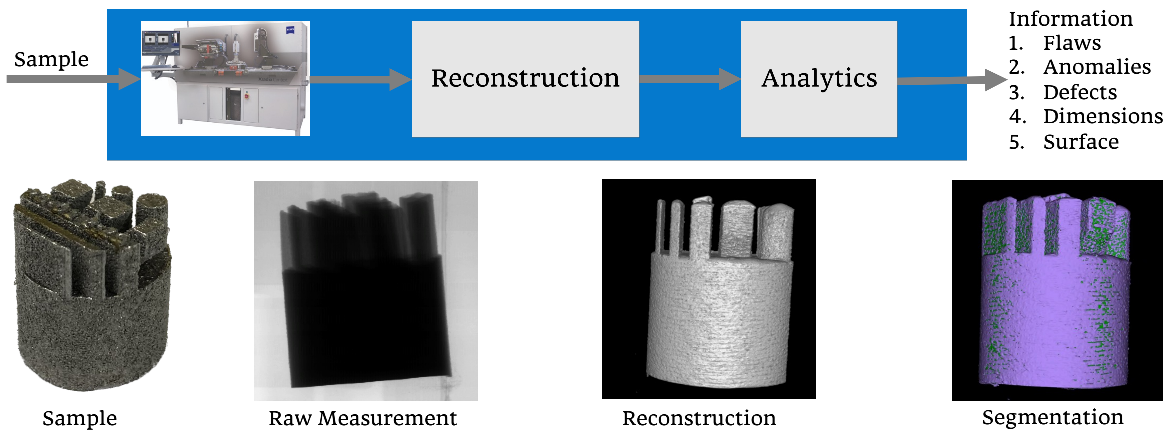

Figure 8. Procedure from scanning to analysis. Each raw data will first get reconstructed into an image, and then it is analyzed using segmentation algorithms to detect flaws and defects, among other analysis.

Even with high-quality reconstruction provided, the standard segmentation algorithm lacks in providing the true statistic of the pores when compared against microscopy data. To mitigate the issue and perform better flaw detection on the high-quality reconstruction, the Kakapo segmentation framework was developed. A comparison between the porosity level detected in 30 parts between the standard algorithm and Kakapo is shown in Figure 10(a). Figure 10(b) further qualitatively demonstrates the improvement in flaw detection using this algorithm. (Note: this work is being prepared for publication, and therefore no reference to the algorithm exists yet.) It should be pointed out that while the standard segmentation algorithm in the vendor software package mostly underestimates the true porosity of the part, the porosity results are provided as region-based for each feature of the parts; therefore, the trends observed for different features based on standard segmentation can be informative in selecting the process parameters. Consequently, those values were also leveraged for completeness in this work package and report.

In summary, the fast and high-quality deep learning–based reconstruction and segmentation algorithms enabled high-throughput characterization of more than 700 coupons designed under this work package and printed with 316L and 316H using the Concept Laser M2 and Renishaw AM400 LPBF 3D-printing systems.

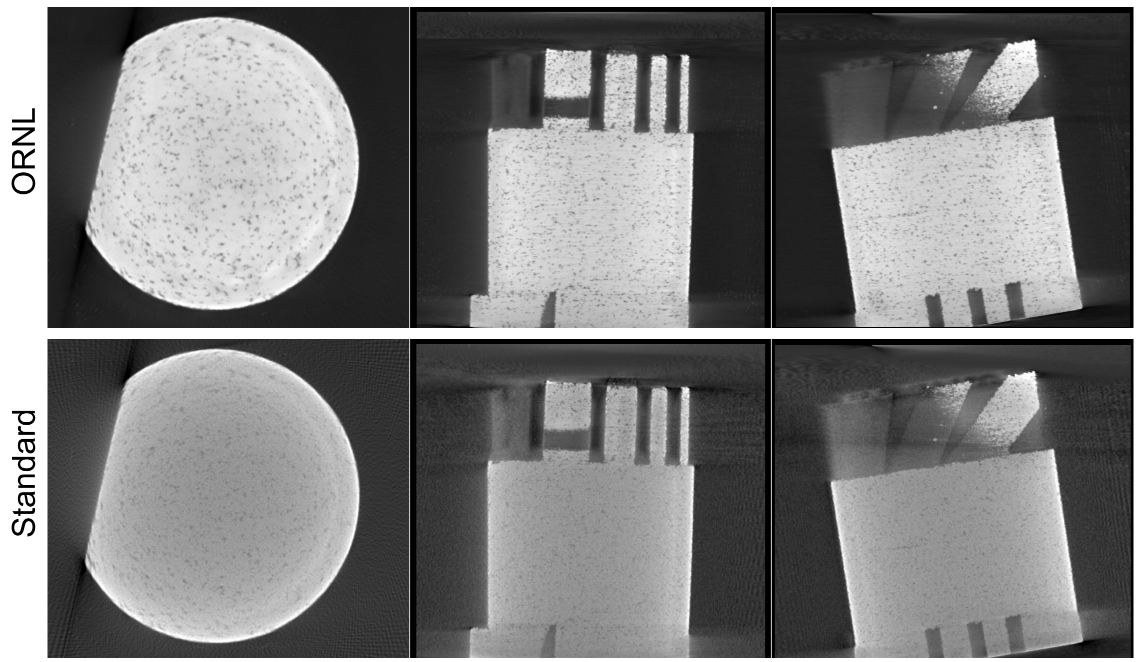

Figure 9. ORNL reconstruction (top) of a 20 min scan of Zeiss metal part made of 316H against standard reconstruction (bottom).

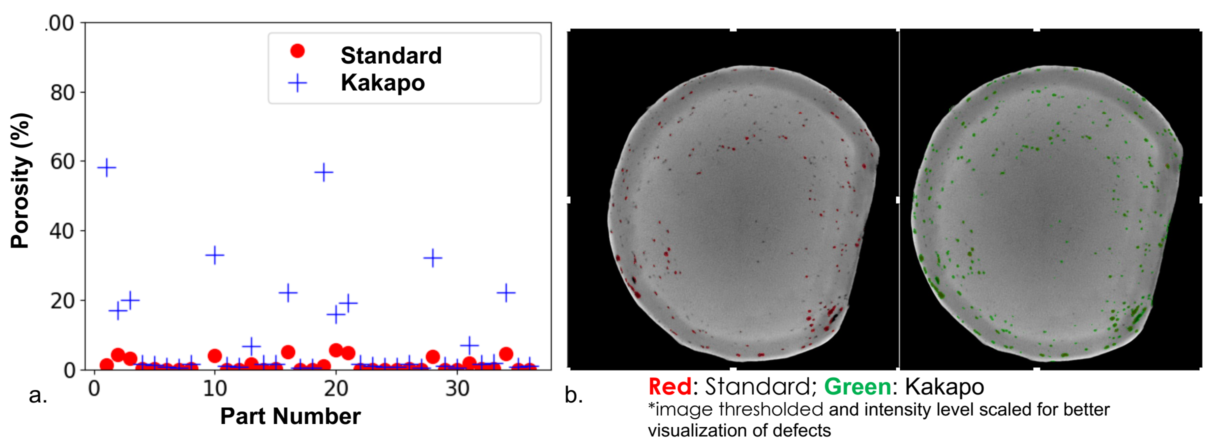

Figure 10. Kakapo segmentation vs. standard segmentation on CAD-DLMBIR reconstruction.

2.3.3 Microscopy and Mechanical Testing

Microstructure characterization was performed on multiple microscopes. The first was a Zeiss high-resolution field emission Crossbeam 550 dual beam FIB/SEM equipped with an Oxford electron backscatter diffraction (EBSD) and energy-dispersive x-ray spectroscopy (EDS) detector. Grain's structure and orientations were characterized with EBSD by collecting data at an accelerating voltage of 25 kV at a step size of 1 µm and postprocessed on the MTEX Matlab toolbox [15]. A chemical variation on the microstructure was measured with the EDS method by applying 15 kV voltage, which approximately yielded 1 µm interaction volume from the surface. The second microscope leveraged was a Tescan MIRA3 GMH field emission SEM also equipped with an Oxford EBSD detector. Maps were collected using an accelerating voltage of 30 kV at step sizes ranging from 0.5 to 2 µm depending on the field of view analyzed. For large field-of-view grain mapping for texture and grain size analysis, a total field of at least 1 mm × 1 mm was surveyed. Large-area optical images were collected before and after etching was collected on a Leica DMi8M equipped with a Leica DMC4500 camera, and images were autostitched onto Leica LAS-X software. Electrolytic etching of samples was done on a solution prepared with 10 g oxalic acid dissolved in 100 mL of distilled water and operated at 2.0 V under direct current. The 316L samples were etched for 90 s to reveal the fish scale structure, while 316H samples were only etched for 20–50 s due to quickly darkened surfaces during a longer etching. Focused ion beam (FIB) liftouts were prepared using a Quanta Dual Beam FIB. Transmission electron microscopy lamella were produced using decreasing beam voltages from 20 kV for initial liftout and 5 kV for final thinning to minimize FIB damage. A FEI Talos transmission electron microscope (TEM) operating at 200 kV was used with coupled EDS to resolve elemental segregation within each sample.

Mechanical properties for select specimens of interest were collected using room temperature microhardness and tensile tests. Hardness was performed on a Leco-LM110AT Vickers hardness tester by applying over 100 indents with a diamond indenter under 500 gf for a 10 s dwell time. For tensile tests, mechanical behavior was evaluated utilizing two different tensile specimen geometries, shown in Figure 11: the SSJ3, a commonly employed geometry in nuclear materials characterization, and the SST, a novel geometry whose extraordinarily small size was designed to accommodate the small, intricate geometries often encountered in AM components, as well as to maximize data extraction from often valuable test materials.

Specimens were tested in the shoulder-loading configuration under ambient conditions on a single-column MTS Criterion Model 42 servomechanical test frame at a nominal strain rate of $10^{-3}s^{-1}$, or displacement rates of 5 and 1.5 µm/s for the SSJ3 and SST, respectively; time, crosshead displacement, load, and gauge cross-section dimensions were recorded. Since strain was not measured directly, a compliance correction method was employed so the approximate plastic strain values could be extracted from the crosshead displacement data:

$$\varepsilon_p = \frac{\delta - P * C_{LL}}{l}, \tag{4}$$

where ε_p is the plastic strain; δ and P are the crosshead displacement and load, respectively; C_{LL} is the load line compliance calculated as the inverse of the elastic slope of the raw load-displacement curve; and l is the gauge length. Once the load-displacement curve is converted to a stress-plastic strain curve, the pertinent tensile values are calculated. The 0.2% offset yield stress (YS) is the stress at 0.2% plastic strain, the ultimate tensile strength (UTS) is the maximum stress, the uniform elongation (UE) is the plastic strain value corresponding to the UTS, and the total elongation (TE) is the plastic elongation at failure.

The SST specimen, due to its small size, is subject to some artifacts that can skew mechanical properties. Some of these artifacts are visualized in Figure 12 for various wrought alloys. In particular, the smaller specimen gauge of the SST specimen, coupled with its different width-to-depth ratio vs. the SSJ3 specimen, results in larger ductility values across the board. Fortunately, for isotropic materials with suitably fine grain size, the strength and uniform elongation values are comparable between the two geometries. Thus, the SST specimen is considered for this work to be an adequate screening tool for site-specific ductility and strength evaluations for specific regions of the miniature Zeiss geometry specimens previously described in this work. It is important to note that in the size effect evaluations conducted in this work package, it was identified that considerable scatter exists in SST tensile specimens with measurable porosity (as in the 316LSS specimens previously printed as part of the transformational challenge reactor). Thus, it can be inferred from mechanical testing data with high scatter and/or poor mechanical strength that considerable porosity may have been present in a particular geometric feature or region.

Wire electrical discharge machining (EDM) was used to extract samples from Zeiss specimens in a way that preserved traceability back to the digital MDDC platform and enabled the extraction of data from thin fins (SST) and the Zeiss specimen body (SSJ3 and SST). The machining schematic and example SST specimens are shown in Figure 13.

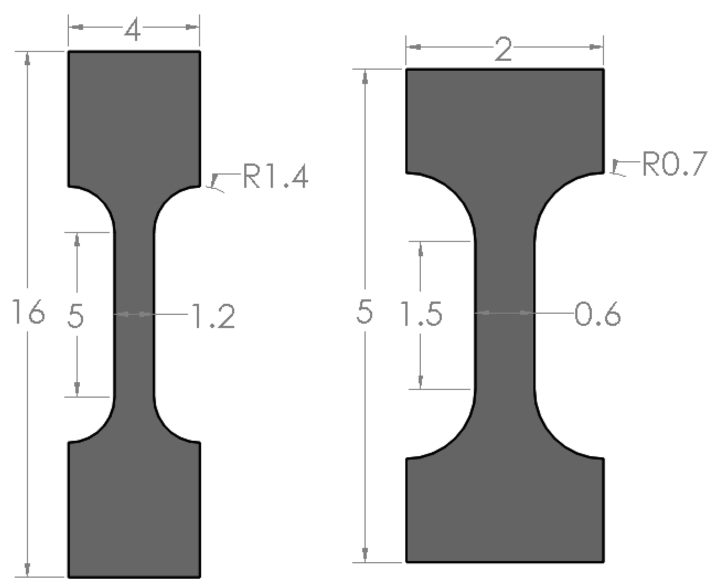

Figure 11. SSJ3 (left) and SST (right) nominal geometries; both are flat dog bone–type specimens. The nominal sample thicknesses are 0.75 mm and 0.6 mm, respectively.

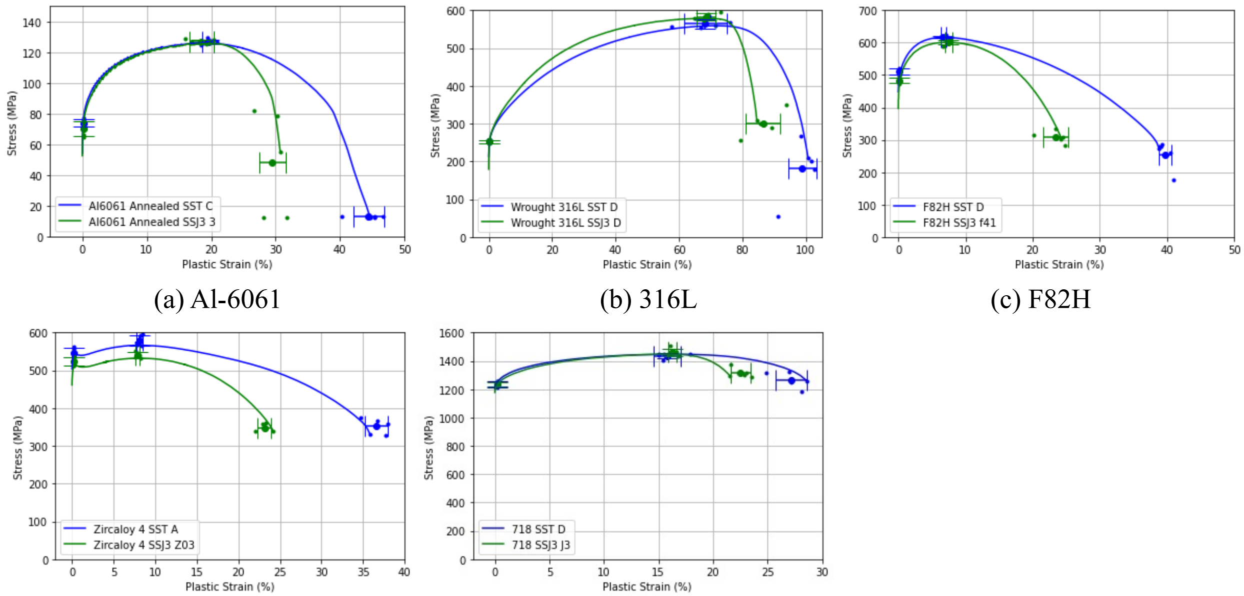

(a) Al-6061 (b) 316L (c) F82H

(d) Zircaloy-4 (e) Inconel 718

Figure 12. Comparison of representative SSJ3 (green) and SST (blue) tensile response for various wrought nuclear-relevant materials included. In each, the error bars indicate the standard deviation in yield strength, ultimate tensile strength, uniform elongation, and total elongation as an average of at least five different measurements.

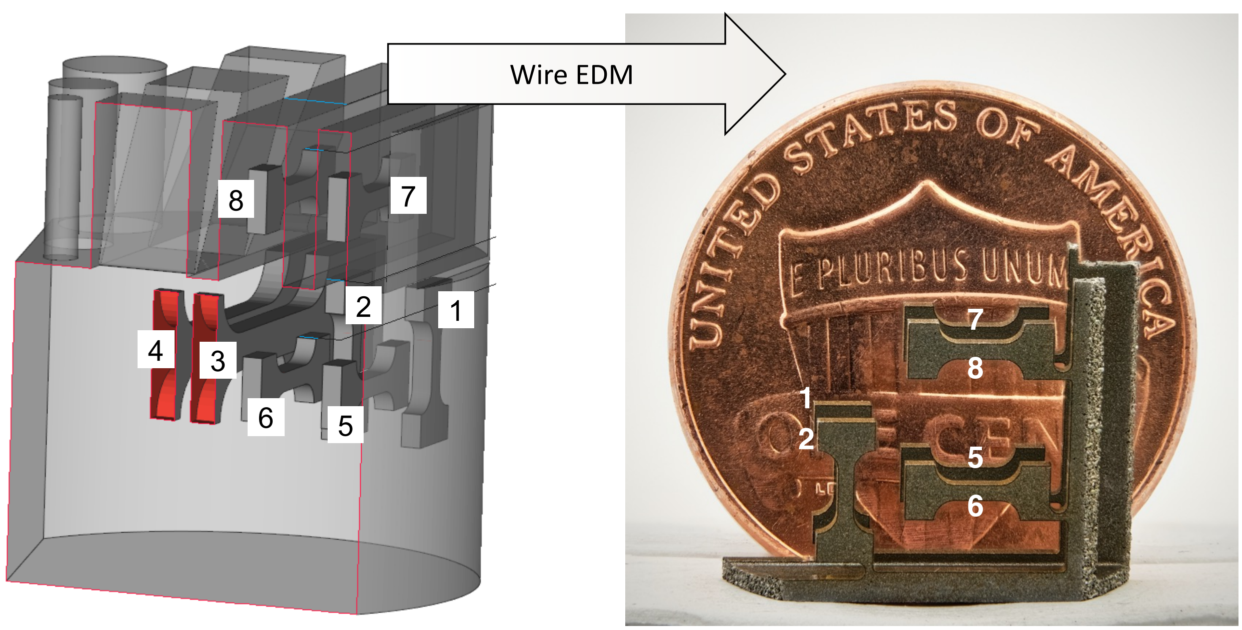

(a) (b)

Figure 13. Tensile specimen harvesting strategy for SSJ3 and SST specimens. In (a), the specific harvest locations are shown that include Body (#1–#6), Fin 2 (#7), and Fin 3 (#8) locations, while (b) shows the scale of the SST specimens in reference to a US penny.

3. RESULTS AND DISCUSSION

3.1 THE USE OF IN SITU DATA AS A QUALITY ASSURANCE TOOL

The FY23 AMMT report on the MDDC framework (M3CR-22OR0403051) proposes four levels at which data can be used to support quality assurance and part qualification efforts. Using the Peregrine software tool, Level II is regularly achieved across a subset of the laser powder bed fusion (LPBF) printers used under the AMMT Program, with support for additional AMMT LPBF printers available by the first quarter of FY24. At Level II, in situ sensors and machine learning (ML) algorithms are sufficient to determine whether a given build was printed under nominal conditions. Level II capabilities can therefore directly assist with qualification in a production setting, as multiple builds with nominally identical geometries and process parameters can be easily compared. Thus, once the in situ sensor signature for a "known-good" instance of a given component has been identified, the sensor signatures for other instances of the same component can be leveraged as one element of the qualification process.

Unlike the Transformational Challenge Reactor (TCR) program, AMMT is focused on process parameter development and on-demand manufacture for one-off components. As a result, Level II capabilities are insufficient for supporting the relevant qualification processes. This is because the current set of deployed Peregrine segmentation models are trained to detect in situ anomalies (Figure 14) as opposed to directly observing flaws or predicting fundamental material properties. In other words, the anomalies detected by Peregrine's segmentation model [16] are not analogous to x-ray computed tomography (XCT) flaw segmentations, and ultimately no geometry-independent quality metrics or thresholds can be determined. Instead, Peregrine analyses of the in situ data can be used to provide the following: (1) significant critical context regarding the process environment, (2) a consistent methodology for comparing parts with identical geometries but varying process parameters, and (3) assurance that no unusual detrimental events (e.g., an under-dosing of powder) occurred during a particular build.
In response to the above limitations, Level III Peregrine capabilities have been under development since FY21 with support provided by TCR, AMMT, and other DOE programs.

For FY23–FY24, these Level III efforts can be broadly associated with two categories. First, the in situ sensor upgrades discussed in Section 2.3.1 and the transition to the DMSCNN (outlined in companion milestone report M3CR-22OR0403051) will enable the direct detection of certain flaws, such as spatter-induced lack-of-fusion porosity. These direct flaw detections can then be treated more analogously to XCT results and could also be ingested by traditional mechanical performance simulations (e.g., crack growth models). Finally, the development of voxelized property prediction models (VPPMs) addresses the geometry-independence problem. Thus, if fundamental material properties can be predicted for sufficiently small subvolumes, the sensor signatures from one subvolume can be readily compared to the signatures for a "known-good" subvolume even if the overall part geometries, process parameters, or build layout are different. Such a technique [17] provides substantial capabilities for on-demand manufacturing but requires extensive materials characterization campaigns and integration between Peregrine and the Myna thermal and microstructural simulation framework.

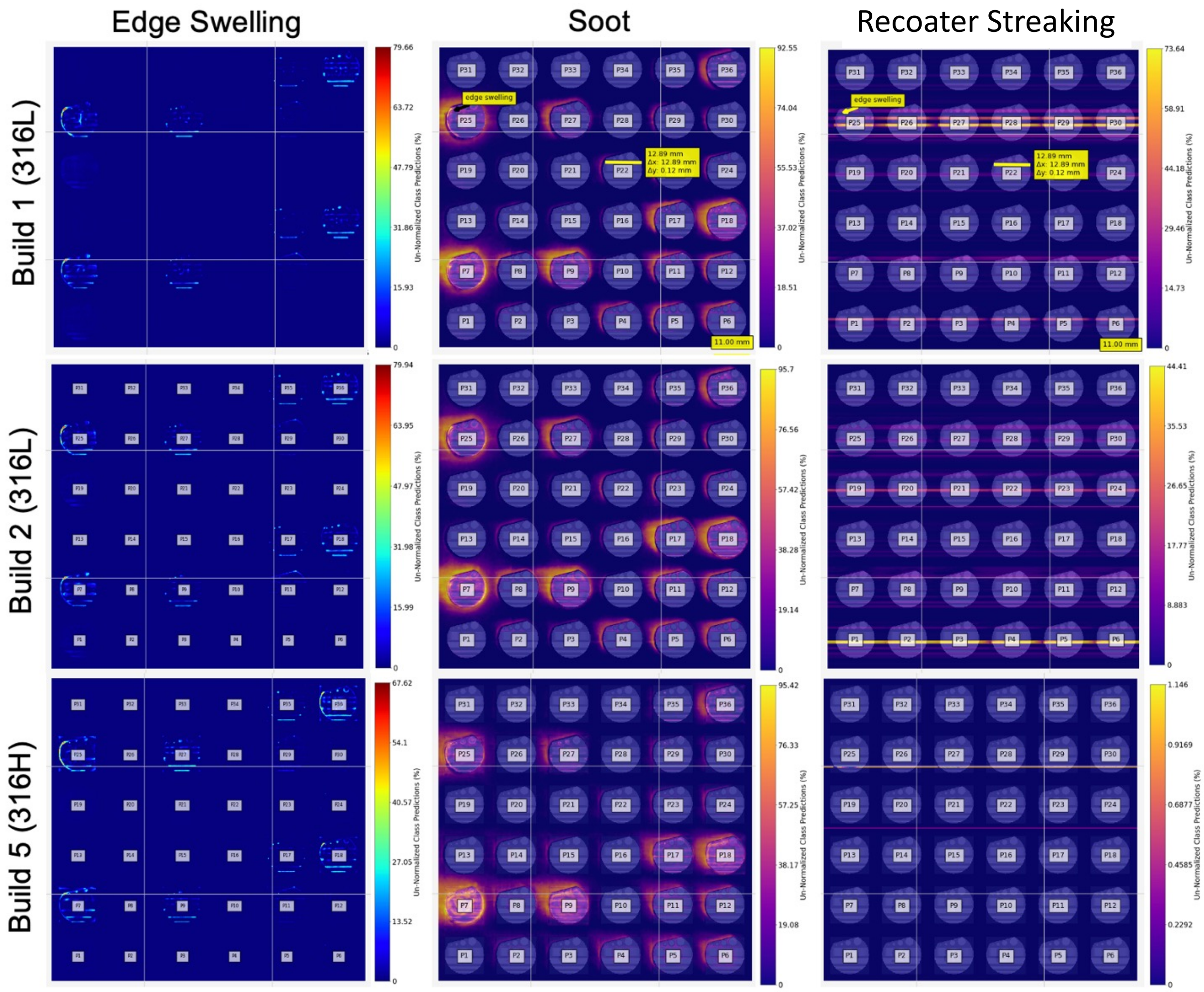

Figure 14. 2D prevalence maps of three classes of characteristic anomalies identified through in situ data collection in three Concept Laser M2 builds (DOE1, DOE2, and DOE5).

3.2 POROSITY ANALYSIS

3.2.1 Concept Laser Builds

A total of 144 316LSS and 108 316HSS Zeiss specimens were printed as part of the concept laser DOE with resulting parameters spanning a volumetric energy density range between 14 and 414 J/mm^3. The summarized XCT data for all builds are plotted as a function of increasing energy density in Figure 15. The porosity levels of both materials reduced from 35% to 0.2% when energy density was increased from 14 to 70 J/mm^3. Then, parts consistently achieved the lowest porosities between 70 and 110 J/mm^3 or roughly between an equivalent linear energy density of 0.25 to 0.5 J/mm. However, their porosity went up to 4.4% when energy density was increased from 110 to 414 J/mm^3. According to the comparison of both materials at identical energy densities, 316H had a slightly higher porosity than 316L under 50 J/mm^3; however, the porosity of 316L became higher than 316H when the energy density was increased beyond 110 J/mm^3. These maps are commonly used to identify the boundaries of process-induced defects such as lack of fusion, keyhole, and balling and to predict the optimum processing conditions to print dense parts [18, 19]. The low power and high scanning velocity combinations caused high porosity, mostly because of the large lack of fusion defect form as a result of poor connection between layers [20, 21]. However, the combination of high power (>300 W) and low velocity (<500 mm/s) resulted in keyhole defects.

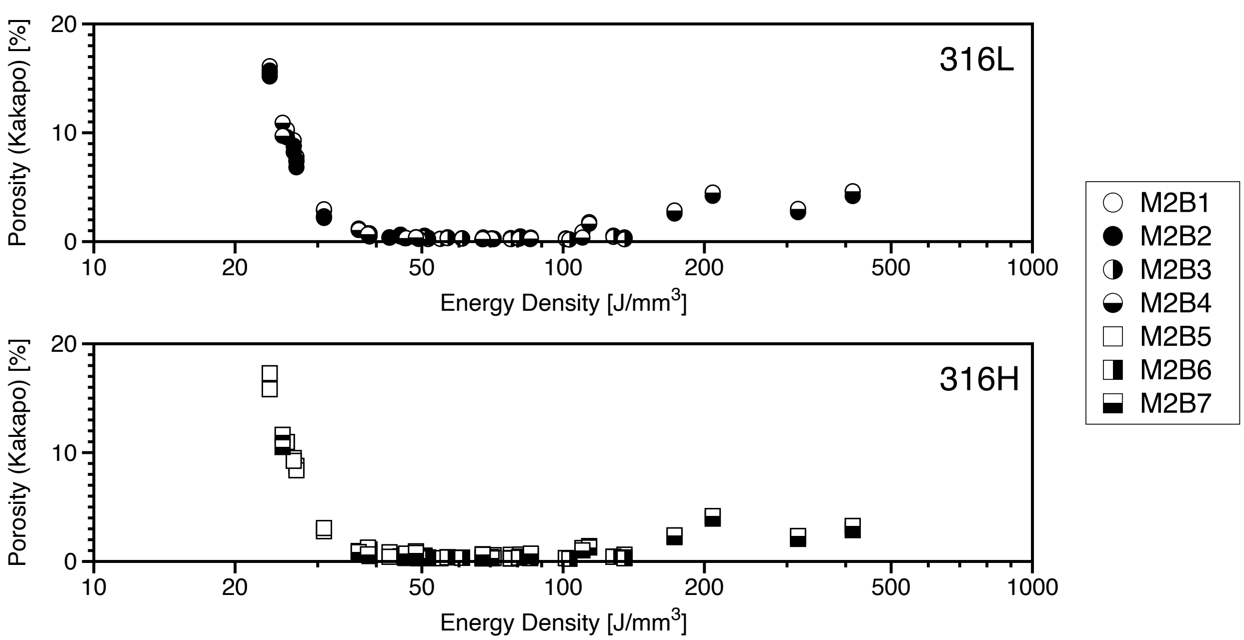

Figure 15. Comparison of all 316L (AM316L-1) and 316H (AM316H-3) specimen porosity using the Kakapo segmentation algorithm for XCT data.

Linking the in situ data with porosity measurements revealed that in situ data alone cannot solely serve as a predictive tool for part porosity. One measure that has been used to summarize the cumulative set of in situ data for each built part is called *aggregated print quality*, which is an imperfect description of summarized in situ data through pixel-by-pixel comparisons of the as-printed part (optical images) with the expected locations of part features from the inputted print geometry. However, it does capture many artifacts, such as edge swelling as well as propagated effects from soot and recoater streaking (if these effects compound and ultimately result in differences in part geometry at subsequent build heights).

Figure 16 shows the relationship between aggregated print quality vs. the bulk porosity measured using the Kakapo XCT segmentation results. In Figure 16(a), each data point is colored with respect to the energy density of the printed part. It is readily apparent that high energy density prints are strongly correlated with both lower print quality and higher porosity. Conversely, high print quality does not necessarily mean low porosity, as illustrated by many lower energy density samples having very high print quality but also concurrently high bulk porosity.

Fortunately, this study's downselection framework also considers the variation of porosity within a part, which is possible through Zeiss's standard XCT segmentation algorithm. In Figure 16(b), the same data are plotted with colors corresponding to the measured spread in XCT data, which is defined as the standard deviation in measured porosity in the different regions of the Zeiss specimen (body, rods, fins, inclines, etc.). This resulting spread is high for both the lower and higher energy density prints and clearly shows an optimized region of processing parameters in red/black near the bottom right corner of the plot. It is from this combined in situ data and XCT analysis that three different samples at increasing energy density (43, 71, and 135 J/mm^3) were chosen for more detailed analysis.

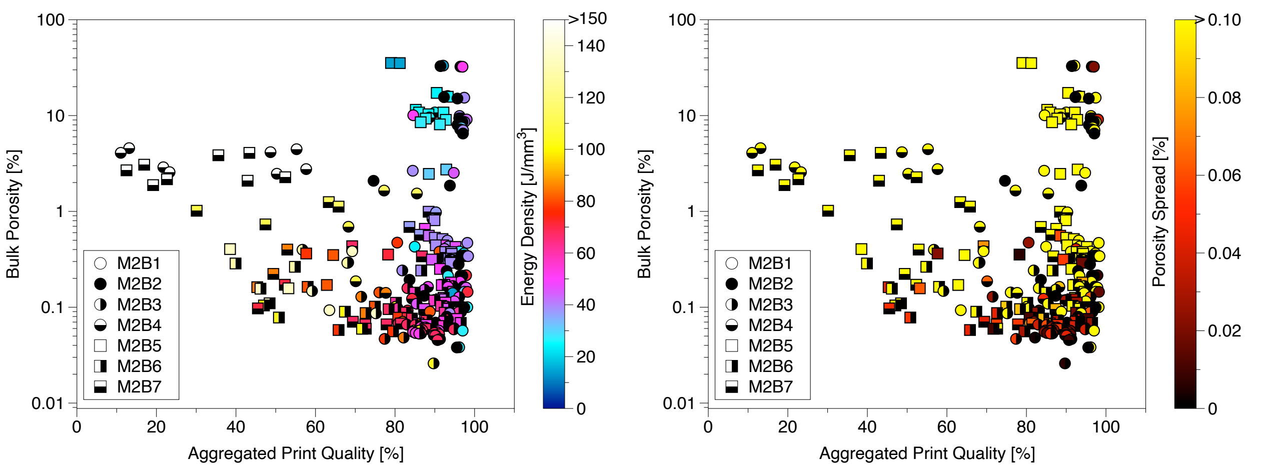

(a) (b)

Figure 16. Comparison of all 316L (AM316L-1) and 316H (AM316H-3) specimen porosity (Kakapo segmentation) with aggregated print quality as measured by in situ data. In (a), the data points are colored with respect to energy density, while in (b), the same data points are colored with respect to measured porosity spread (Zeiss segmentation) within each Zeiss specimen.

The subsequent characterization of the energy density effect on the microstructure was carried out by selecting 43, 71, and 135 J/mm^3 energy densities from both 316L and 316H builds, which possessed <0.2% porosity. The optical images of selected builds were shown in Figure 17(a–d), and according to that, low energy density samples (43 J/mm^3) produced more lack of fusion defects, while most of these defects seemed to be removed at 71 J/mm^3. When high energy, 135 J/mm^3 density was applied, the circular-shaped keyhole porosity began to appear as a result of vaporized constituent elements, such as Mn, and Ni as previously discussed.

The accumulation of additional porosity in the thin-walled rods and fins also can be viewed in their reconstructed XCT scan images in Figure 17(e–f), in which the fin and rods of the build tend to include more pores than the body section. To get a better understanding of pore size changes concerning build height, pore populations in 316L and 316H builds are shown in Figure 18. The effect of different part geometries can be seen in the high number of pores in fins as opposed to the bulk regions, which was consistently observed across all energy densities. Among all energy densities, 71 J/mm^3 has the least pore formation, and the pores were more homogeneously distributed across these samples.

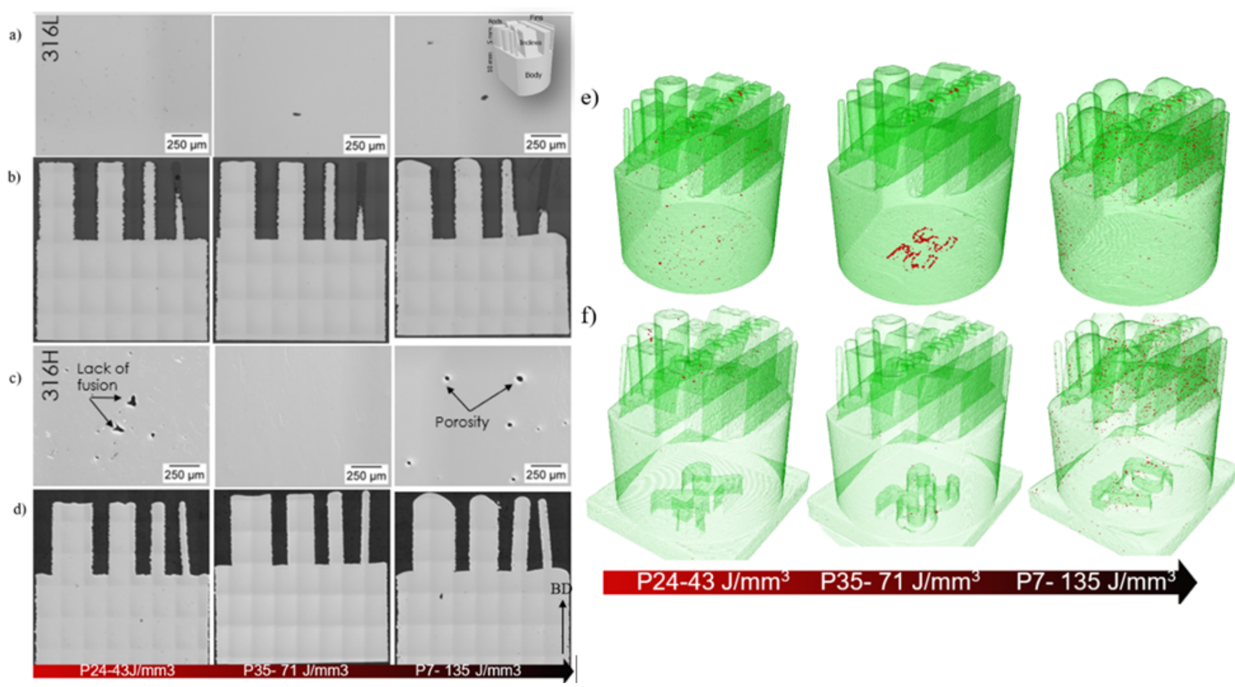

Figure 17. Optical micrographs of (a, b) 316L and (c, d) 316H samples given as (a, d) high magnification and (b, c) entire cross-section images. Reconstructed XCT images of (e) 316L and (f) 316H builds shown with respect to energy densities.

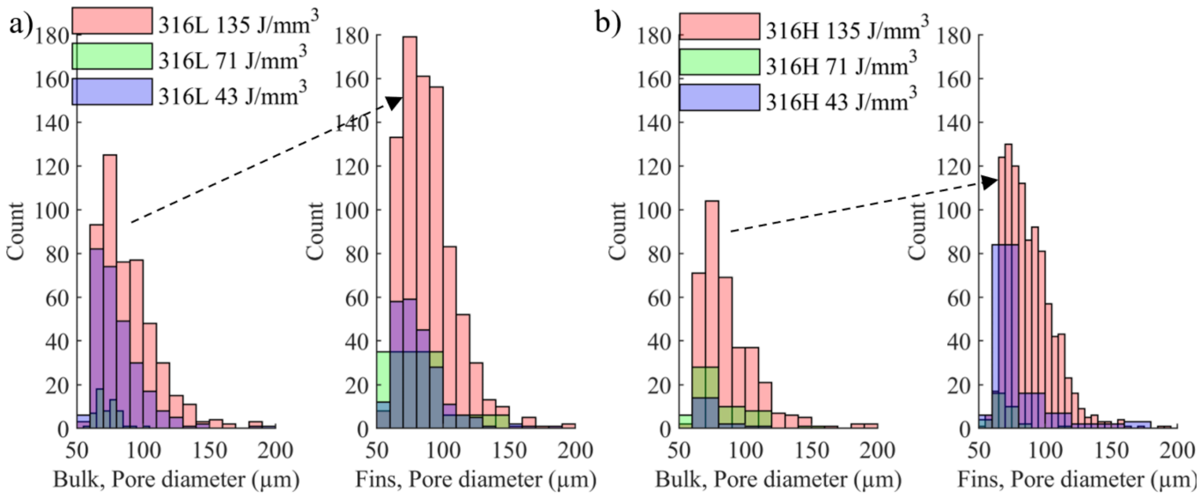

Figure 18. Reconstructed pore size distribution bulk and fins section of (a) 316L and (b) 316H builds produced with 43 J/mm^3, 71 J/mm^3, and 135 J/mm^3 energy densities. Sample names in some of the small histograms were indicated for clarity, and big arrows shows the general trend of the increased pore population from bulk to fin regions. Overlapping regions are shown as regions with mixed color profiles.

3.2.2 Renishaw Builds

A total of 210 samples were printed for SS316L, and 180 samples were printed for SS316H. SS316H appeared to retain more heat during the printing process, making it difficult to complete the PA build without removing multiple samples that were to be printed with extreme parameters. Since variations in hatch spacing were captured in build PB, it was not a concern to have to omit PA from the SS316H processing study. All Renishaw Zeiss samples were analyzed with the same XCT process as performed on the Concept Laser Zeiss samples. As a quick comparison, the mean void space was calculated for each Zeiss specimen and plotted in Figure 19(a, b) against the energy density. Overall, the void space in either SS316L or SS316H is higher at energy densities <50 J/mm^3 and >200 J/mm^3. Compressing the data down using the grand mean, taken as the mean void space for samples with the same energy density, a clearer trend can be observed, as shown in Figure 19(c, d). Under a focused range at more intermediate energy densities in Figure 19(d), there is a shift in the energy density for when the void space is lower in the SS316H than SS316L. However, both materials show that a mean void space is achievable over a wide range of energy densities.

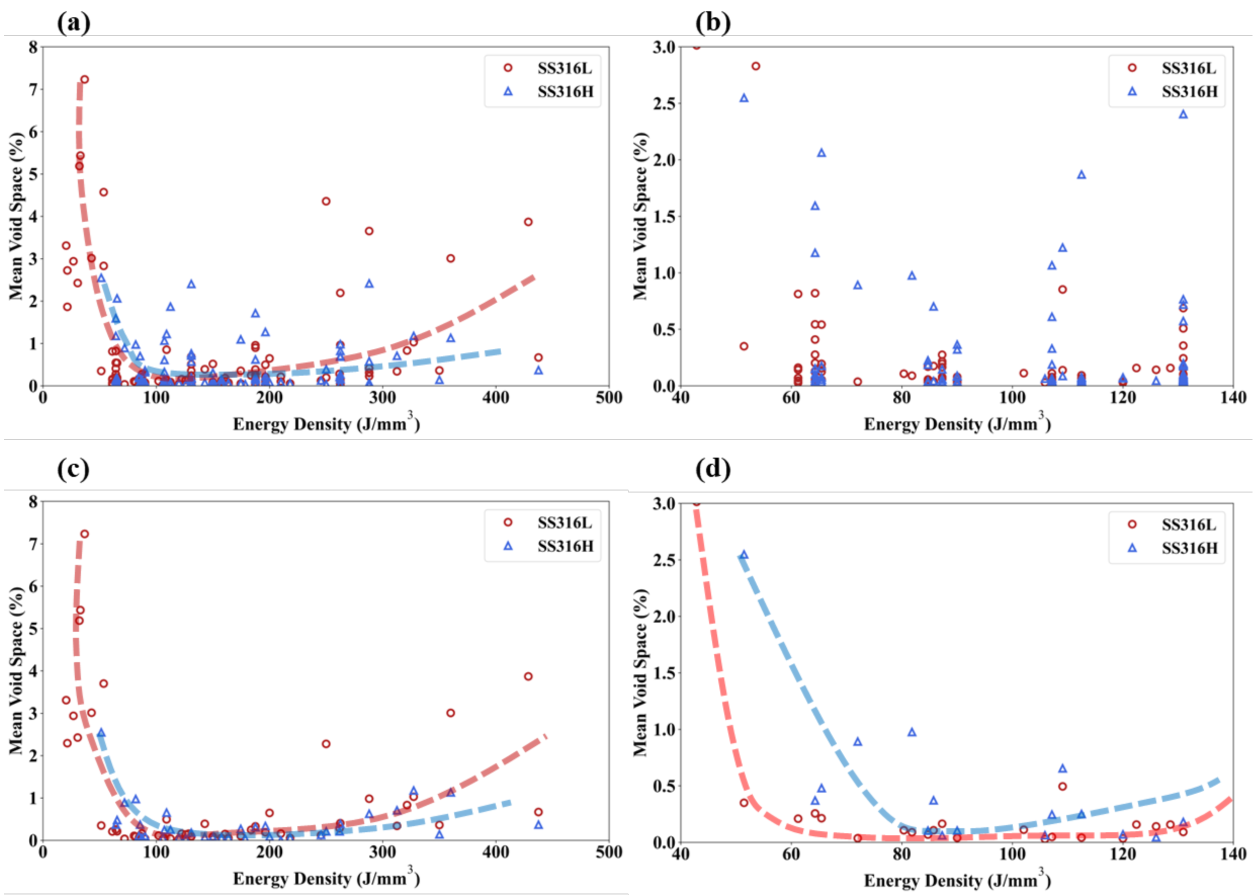

Figure 19. General mean bulk porosity trends for 316L (AM316L-2) and 316H (AM316H-3) builds performed on the Renishaw. General trends are highlighted using arbitrary fit functions. (a, b) Mean void data for all 390 Zeiss samples and (c, d) the grain mean void data averaged over samples with the same energy density. (a, c) Full range of energy densities explored and (b, d) focusing on only intermediate energy densities (40–140 J/mm^3).

Energy density helps normalize the data to suggest general trends, but more analysis is needed to help specify the optimized parameters. Instead of collapsing the data to one normalized value (i.e., energy density), the void space data were segmentized into the individual geometric features. The features were separated into five regions labeled as *all* (the entire sample), the combination of the *rods*, *fins*, and *inclines*, as well as the *body* below the crown of the sample. For simplification, the average of the void space in each rod, fin, and incline was taken as the whole value for each region. All data were imported and analyzed with the Minitab software used specifically for statistical analysis of data. Using the CCD design, Minitab will process and fit the data according to linear + square regression expressed as follows:

Once the fitting is established, the data can be manipulated to predict the appropriate response based on the given inputs for the various factors.

$$Response = C_1 \cdot Factor_1 + C_2 Factor_2 + \cdots C_n Factor_1^2, \tag{5}$$

Overlaid contour plots were generated for the void space found in the five different geometric features for interactions between two parameters, as shown in Figure 20 for PB. The solid and dashed lines represent the boundaries for 0% and 0.1% void space, respectively. The white space represents the parameter region over which <0.1% porosity can be achieved in all five geometric features. The gray represents the space in which porosity is higher than 0.1%. The white space in Figure 20 for build PB has almost no white space, indicating limited parameter combinations for optimizing density across all geometric features. There is also a clear shift in the angel wing pattern observed between similar plots for SS316L and SS316H.

In comparison, the amount of white space found in similar maps for build PG shown in Figure 21 was higher than what was observed in similar maps for build PB. Considering the difference between PB and PG in the assignment of the fourth parameter, hatch spacing vs. hatch offset, one can see the profound effect that energy density parameters have on each vs. other influential parameter such as the hatch offset. Given the stochastic nature of the LPBF, environmental effects such as soot formation or super elevation in certain samples can negatively affect the build quality of the other components on the build plate. More variability in the void space between samples suggests that the parameter in question is more likely to be influential to causing the types of defects seen in LPBF.

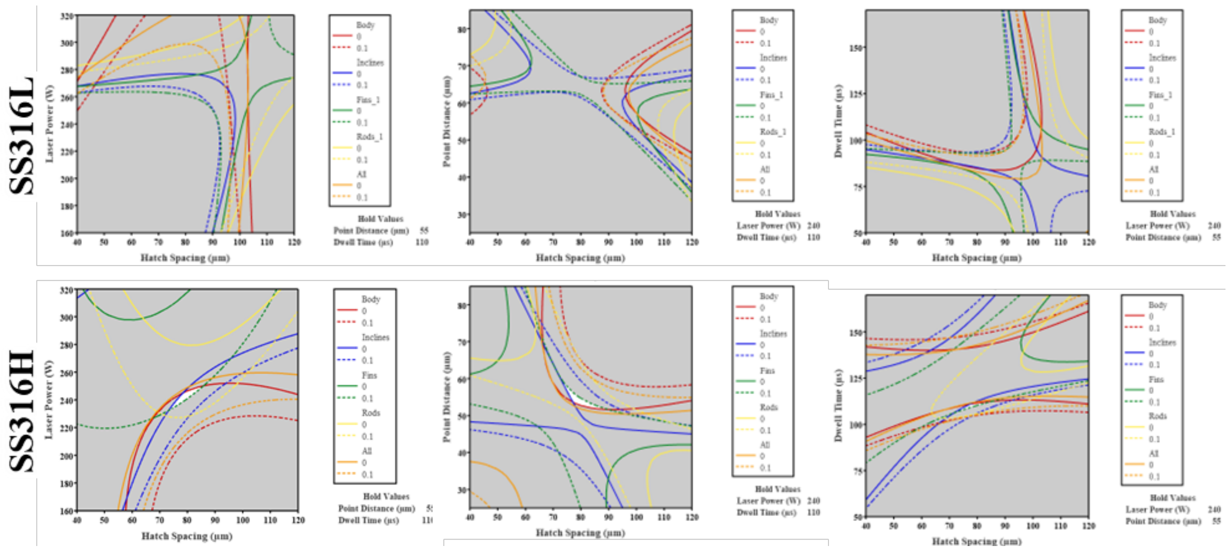

Figure 20. General mean bulk porosity trends for 316L (AM316L-2) and 316H (AM316H-3) build PB performed on the Renishaw. In each plot, the area between solid and dashed lines indicates porosity below 0.1% in the body (red), inclines (blue), fins (green), rods (orange), and the entire Zeiss specimen (yellow). White regions indicate processing space where porosity is minimized for all overlaid curves.

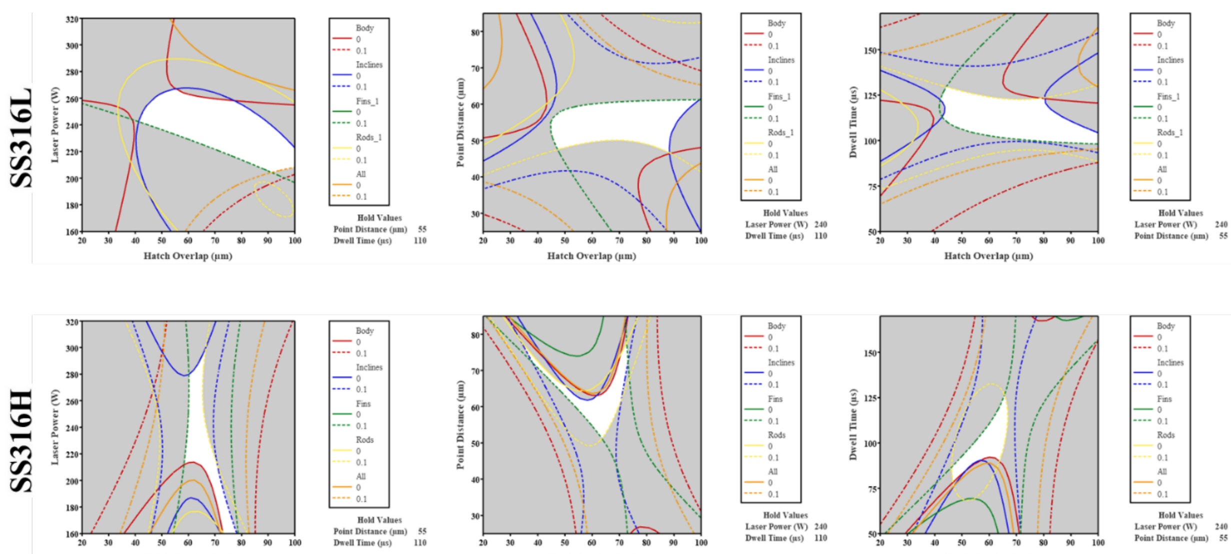

Figure 21. General mean bulk porosity trends for 316L (AM316L-2) and 316H (AM316H-3) build PG performed on the Renishaw. In each plot, the area between solid and dashed lines indicates porosity below 0.1% in the body (red), inclines (blue), fins (green), rods (orange), and the entire Zeiss specimen (yellow). White regions indicate processing space where porosity is minimized for all overlaid curves.

Understanding the significance of various parameters is important for choosing what parameters to study for any given material without having to spend any additional time turning all the possible knobs. Analysis of the true significance of the different parameters can be quantified using statistical tests such as testing for the F-value and subsequently for the p-value. The F-value is expressed as follows:

$$F - value = \frac{variance\ between\ groups}{variance\ between\ all\ samples}, \tag{6}$$

where a group is related to the terms in the regression fitting, whether that is an individual parameter, or squared term. A normal distribution profile can be generated based on the calculated F-values. Setting the confidence level at 95% (0.95), 5% (0.05) of the data are assumed to be significantly different from the center value in the distribution curve. A p-value is calculated as the area under the normal distribution curve over that 5% interval. Therefore, a p-value ≤0.05 will be considered statistically significant.

Analysis of variance calculations was performed on the 13 builds, and the factors with p-values ≤0.05 were plotted in Figure 22. The histogram plots the count for the low p-values found for each parameter. Using the regression fittings, both single-linear terms and square terms were included. Single parameter square terms suggest a stronger influence of the parameter on the void space but a nonlinear response. Multiples of two parameters indicate the influence from the interaction between the two variables. The aliasing was limited to the laser power, point distance, and dwell time. The fourth parameter in each build was simply labeled as *variable* to easily compare the interactions of the linear energy density terms with the varied fourth parameter for SS316L and SS316H. The SS316L appeared to be strongly influenced by all parameters but most strongly by the point distance. Similarly, the SS316H appears to be influenced by the point distance and the dwell time; however, there is no grouping from any of the laser power interactions. This would suggest that SS316H would behave similarly with varying laser power if the other parameters remained constant. SS316H also appears to have some influence from variable–variable interactions, which broadly includes terms such as the hatch spacing and spot size. However, since the p-value count is relatively low considering six different parameters were varied, the influence of other parameters not included in the linear energy density is low.

All 390 samples were evaluated for the porosity content in each of the 5 geometric features to help downselect parameters. Using the regression fitting shown to provide the maps in Figure 20 and Figure 21, a fitted porosity content was predicted for the geometries *all*, *fins*, and *body*. Only these three were selected to reduce sample sizing run times. A threshold of 0.105% was used to grade the porosity content, scored from 0 to 1, with 1 being <0.105%, 0.5 being 0.105%–0.205%, and 0 being anything >0.205%. The rating can help identify what parameters are the most stable for yielding low void space in printed samples. Collected scores from SS316L and SS316H are shown in Figure 23. Only samples from builds PA, PB, and PC are plotted for a correlation between builds with only energy density parameters. As shown in Figure 23(a, c), the SS316L and SS316H do not show stability in the *all* and *body* until <61 J/mm^3 and <85 J/mm^3, respectively. The *fins* appear to require higher energy density to exhibit minimum porosity, as shown in Figure 23(b).

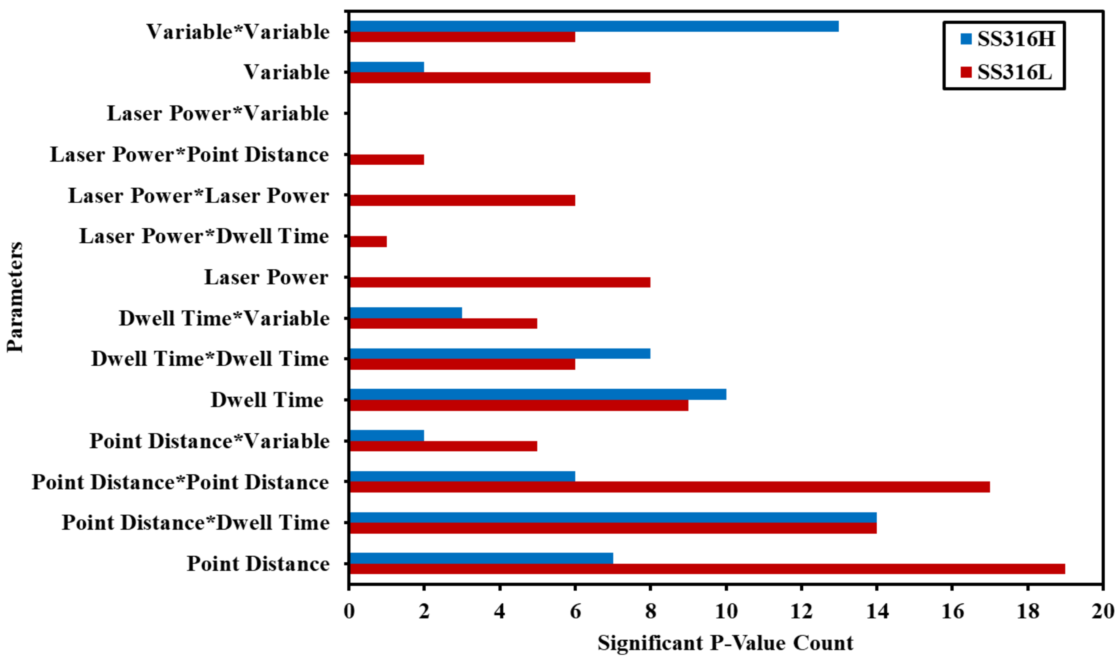

Figure 22. The statistical effect of various input parameters on porosity in Renishaw printed specimens. In addition to laser power, point distance, and dwell time, the additional "variable" indicates all other minor processing conditions changed for each build.

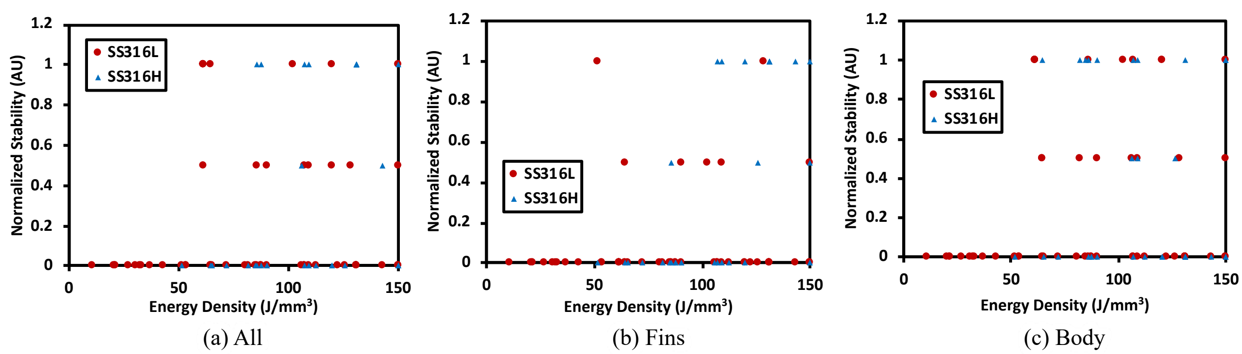

Figure 23. Normalized stability values for all printed 316L (AM316L-2) and 316H (AM316H-3) samples printed using the Renishaw. All data computed using the Zeiss segmentation algorithm across (a) the entire Zeiss part, (b) in the thin fin regions, and (c) in the cylindrical body portion only. The stability value is a set to 1 for samples with less than 0.1% porosity, 0.5 for samples between 0.1% and 0.2%, and 0 for samples with porosity greater than 0.2%.

Varying the non-energy density parameters—spot size, stripe width, scan rotation, and hatch offset—past their median values did not appear to severely affect the void space formation. In general, all these parameters can be held at their median values for any combination of the energy density parameters. Void space formation is certainly sensitive to layer thickness and hatch spacing, but these two parameters were not systematically varied with all the other influential parameters. Build PC for both SS316L and SS316H resulted in many combinations of parameters, yielding dense features at layer thicknesses of 40 and 50 µm. Considering that a 50 µm layer thickness is used for the concept laser and the Renishaw at ANL, the optimized condition will include a layer thickness of 50 µm, understanding that alternates can be used to process material fully dense.

Histograms showing the spread of values found for the laser power, point distance, and dwell time are shown in Figure 23 for printing SS316L or SS316H. Hatch spacing is not represented in the histogram since there were few samples showing high stability from PA or PB in either SS316L or SS316H; however, effects of hatch spacing still need to be narrowed. As shown in Figure 24(a), laser powers between 200 and 250 W appear to the most effective as the general trend leans toward the lower laser powers. Clearly, a point distance of 70 µm is the most effective for producing minimal void space, as shown in Figure 24(b), even though point distance appears to be a highly influential parameter, as indicated in Figure 22. The histogram for the dwell time in Figure 24(c) does not show any identifiable trend, as values 80–140 µs all yield minimal void space.

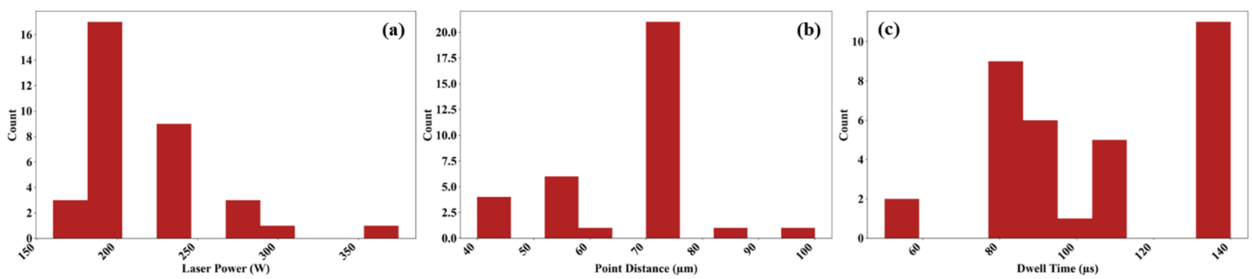

Figure 24. Histograms detailing the values for (a) laser power, (b) point distance, and (c) dwell time found in the Zeiss samples with the most stable parameter combinations for both SS316L and SS316H.

During down selection, it was determined that the four most influential parameters included terms found in the energy density equation—laser power, point distance, dwell time, and hatch spacing. Other influential parameters such as the layer thickness and spot size could be held constant at their nominal values. Minimal porosity can be achieved with this approach if the laser power, point distance, dwell time, and hatch spacing are varied within a reasonable range where the energy density is 60–65 J/mm^3 for SS316L and 80-85 J/mm^3 for SS316H, as identified in Figure 19. To further narrow the parameters, the identifiable ranges for laser power, point distance, dwell time, and hatch spacing are listed in Table 4 for SS316L and SS316H. The ranges for SS316L and SS316H are similar, but the laser power was adjusted to reflect higher energy density parameters.

Table 4. Range of acceptable values for the most influential parameters laser power, point distance, dwell time, and hatch spacing when printing SS316L or SS316H. These values are given supposing that the other influential parameters remain at their nominal values.

	Laser Power		Point Distance		Dwell Time		Hatch Spacing	
Material	Low	High	Low	High	Low	High	Low	High
SS316L	160	240	50	90	50	170	70	110
SS316H	180	260	50	90	50	170	70	110

3.3 FACTORS AFFECTING MICROSTRUCTURE

3.3.1 Effect of Composition

Although the processing ranges are similar between 316L and 316H with respect to porosity minimization, additional complexity is revealed when microstructural differences are considered. The detailed characterization of 316L and 316H structures was performed by etching the structures to reveal their underlying grain boundary and phase features. As shown in Figure 25, the 316L samples showed two distinct contrasts: a lightly etched region appeared at the center of the melt pool while a darkly etched region, so so-called fish scale [8] tended to surround the edge of it. The area of the lightly etched region seems to be affected by energy density, and it was increased from 45% to 52% with increased energy density. Unlike 316L, the 316H structures did not reveal any fish scale formation, and this stark contrast was absent. When compared with the 316L structure, the 316H structure exhibited significantly longer grains that passed through multiple melt pools, whereas 316L grains were typically confined within the melt pool boundaries. The melt pool dimensions in both samples were closely measured, and their melt pool widths and depths were increased proportionally from 100 to 350 µm and 200 to 700 µm, respectively, with energy density.

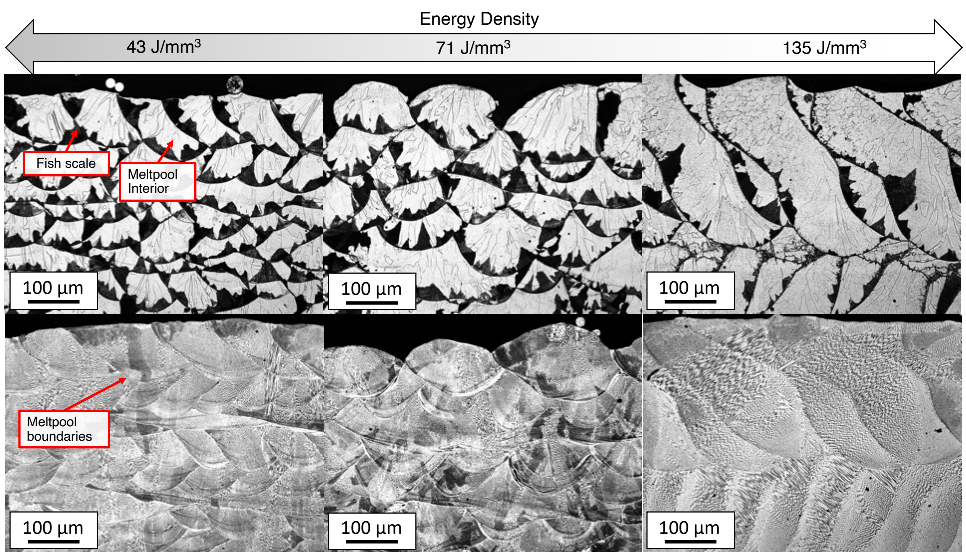

Figure 25. Optical images of grain structures revealed through electrolytic etching of 316L (AM316L-1, top) and 316H (AM316H-3, bottom) specimens printed with different energy densities on the concept laser.

High magnification backscattered images of 316L and 316H samples and their Ni, Cr, and EDS line maps were shown in Figure 26 and Figure 27. When the 316L sample was examined, the dendritic structure of the fish scale region was revealed after the etching process, while the center of the melt pool did not seem to be affected. The line scans of fish scale interdendritic regions showed an increased Cr and a Ni drop, while the melt pool interiors were slightly enriched with Ni. In Figure 27, a similar analysis was carried out on 316H samples, and these micrographs showed clear cellular and dendritic structure and a number of circular voids, which were indicated with white arrows, across the melt pools. The interdendritic regions were rich with Cr and poor with Ni, and this observation was repeated on the circular voids. These circular voids were most likely formed as a result of pulled-out oxides that can leave a circular impression [22, 23].

Austenitic steel 316L and 316H alloys mainly include an austenitic phase, while they can occasionally include small fractions of delta ferrite due to the compositional variation in ASTM [2] specification. The variation in the composition can be captured with Cr_{eq} (Cr+Mo+0.7Nb) and Ni_{eq} (Ni+35C+20N+0.25Cu) numbers on the Schaeffler diagram (WRC-1992), which was used to predict solidification phases under slow cooling rates [24]. In Figure 28, 316L and 316H powder compositions were shown with their ASTM specification [11] of Ni_{eq} and Cr_{eq} boundaries. According to that, 316H and Renishaw builds were found at the intersection of the austenitic-ferritic region, while 316L composition showed up at the ferritic-austenitic (FA) region at 10% of the ferrite line. The Cr_{eq}/Ni_{eq} ratio is also used to predict the solidification mode of composition, and high values (>1.5) indicate ferritic solidification of the structure. The Cr_{eq}/Ni_{eq} ratios of AM316H-3 and AM316L-2 were computed as 1.28 and 1.29 in AF mode, respectively, while AM316L-1 was predicted as 1.55 in FA mode. It should be noted that the Schaeffler method is more accurate when the cooling rate is <50 K/s, so in the next step, the Scheil–Gulliver method was used to include the effect of fast cooling rates. The simulation was based on nominal powder compositions, and none of the phases in the database were restricted. According to results in Figure 28**,** the primary forming phase was predicted as delta ferrite (BCC_A2), and it was followed by austenite (FCC_A1) when the temperature dropped below 1,436°C. The AM316L-1 composition yielded 36% delta ferrite, while AM316H-3 and AM316L-2 powders formed 21% and 9% of delta ferrite until austenite formation. The results of thermodynamic predictions suggest that all compositions were solidified in FA mode while the fraction of the ferrite phases varied due to the difference in the chemical compositions. It can be also noted that the high fraction of delta ferrite in 316L compositions supports the fish scale formation, which was observed on etched optical images. In addition to the main phases, the method also predicted the formation of Cr, Mn-rich oxide (spinel), and Cr-rich MnS (MS_B1) phase, which was considered to be a reason for pitting corrosion in 316L structure [25].

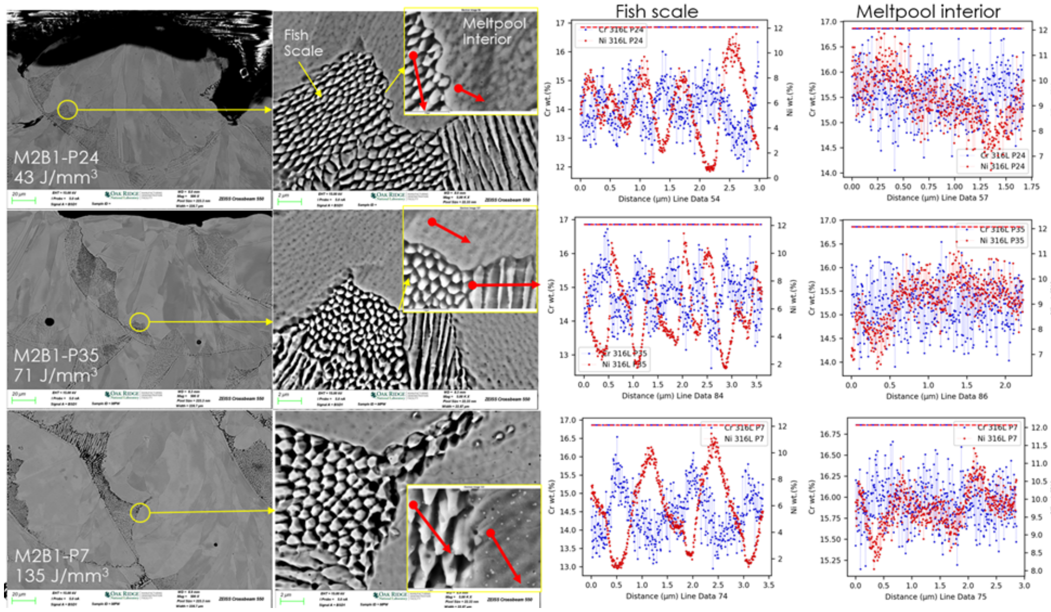

Figure 26. SEM+EDS analysis revealing characteristic elemental segregation in fish scale cellular structure in 316L (AM316L-1) samples printed on the concept laser. The left SEM secondary electron images show the grain structure near the fish scale interface within a weld pool of each of three 316L samples previously shown in Figure 25. Accompanying EDS line scans within the fish scale region and within the melt pool interior show differences in Ni and Cr segregation.

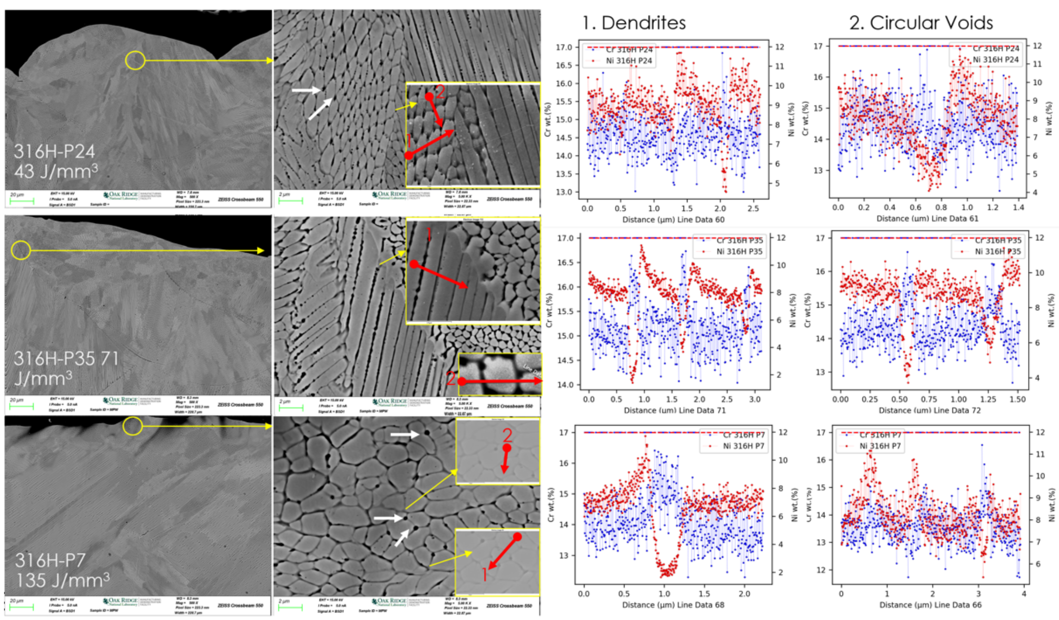

Figure 27. SEM+EDS analysis revealing characteristic elemental segregation in fish scale cellular structure in 316H samples printed on the concept laser. The left SEM secondary electron images show the grain structure near the fish scale interface within a weld pool of each of three 316L samples previously shown in Figure 26. Accompanying EDS line scans within the fish scale region and within the interdendritic region and circular voids show differences in Ni and Cr segregation.

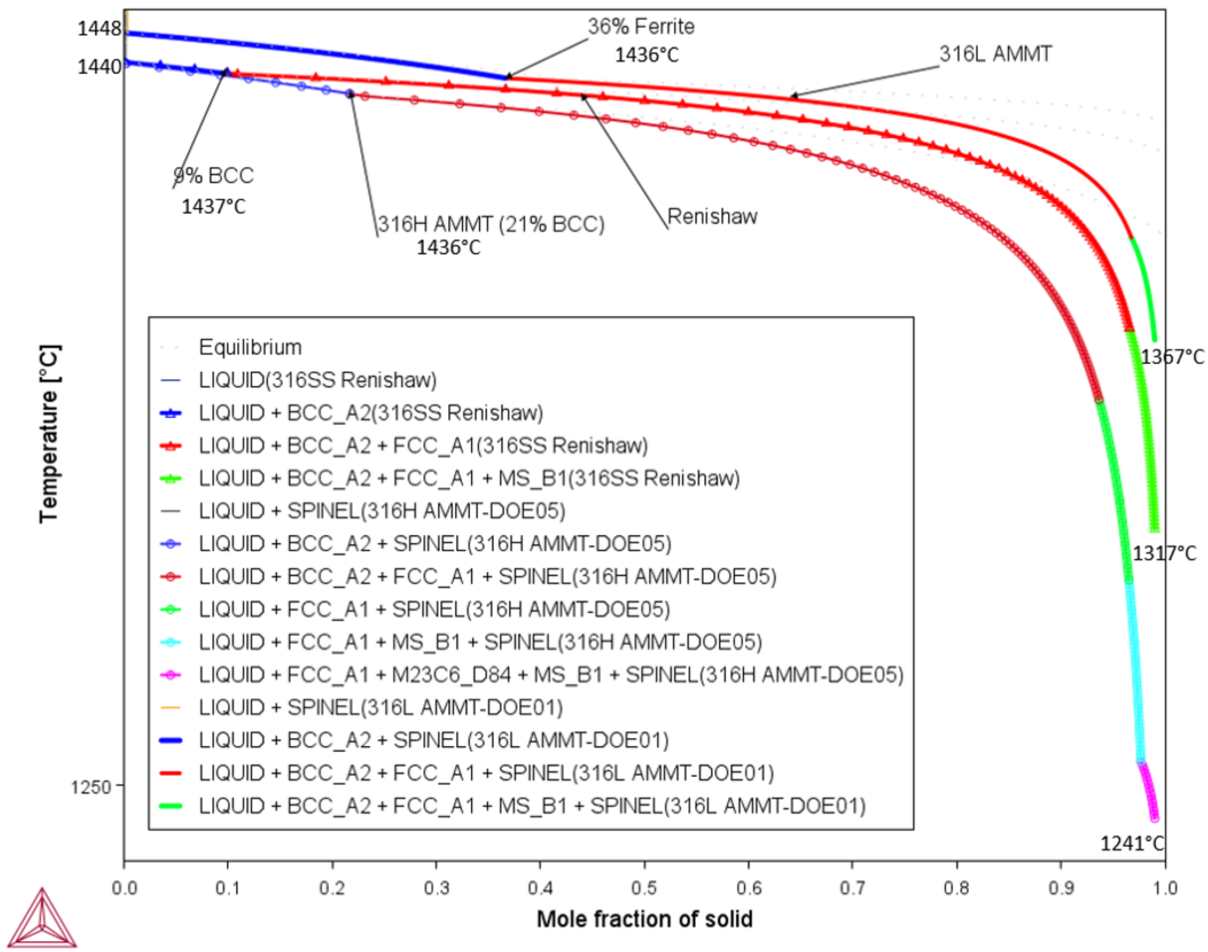

Figure 28. Powder composition of 316L, 316H, and Renishaw prints was overlayed using Scheil–Gulliver methods to predict the fast solidification phases.

3.3.2 Effect of Energy Density

Not only is powder composition important for driving the final microstructure; the energy density has the potential to drastically change the morphology and preferred grain orientation within 316HSS. To investigate the grains' textural and morphological properties, both 316L and 316H samples were scanned along the build direction with the EBSD method. The inverse pole figure (IPF) maps are shown in Figure 29. According to that, 316L was composed of more randomly oriented refined grains with a chevron-like morphology. For these 316L specimens, the grain population did not seem to be affected from increased energy density. Although most of the grains were randomly textured, the pole figure of the maps showed a weak texture along [111] direction. The 316H samples also showed a similar random distribution at low energy density; however, when energy density was increased to 71 and 135 J/mm^3, the texture in the build direction began to be centered around [001] direction. The grain size of the samples of 316L was usually constant over the entire energy density range analyzed, but 316H's grain size increased as the refined chevron grains transformed into elongated columnar grains.

For the Renishaw samples, the same trend of increasing grain size and grain anisotropy can be seen as a function of increasing energy density in Figure 30, albeit with slightly shifted regions of stability. For example, as mentioned in prior sections on porosity, samples with energy densities lower than 80 J/mm3 experienced, on average, higher porosity. Coupling this knowledge with the IPF maps in Figure 30, it follows that there is not a stable set of printing parameters that results in both low porosity and a microstructure with refined chevron grains. Instead, some degree of grain elongation will be expected for optimized Renishaw print conditions.

The observed microstructural variation on both the concept laser and Renishaw builds is also accompanied by changes in the elemental segregation noted within each sample. An example is given in Figure 31 for samples printed using the concept laser with increasing energy density. These are the same samples imaged previously in Figure 29 for reference. As the energy density increases, the characteristic nanoscale cellular structure that forms within each grain evolves with energy density. Even though this data only comprises two different TEM specimens per condition, the trends were the same for all imaged grains. Although the enrichment on cellular walls was consistent between the three variants, averaging 4 wt % excess Cr in comparison to the surrounding matrix, the size of the cells varied as a function of energy density. Although the grain size increased monotonically with energy density, the cellular size is maximized by almost a factor of 2 at the intermediate energy density. Additional work in FY24 will take liftouts as a function of build height to see the statistical variation in cellular structure so that higher fidelity models can be generated to predict these microstructural features during printing.

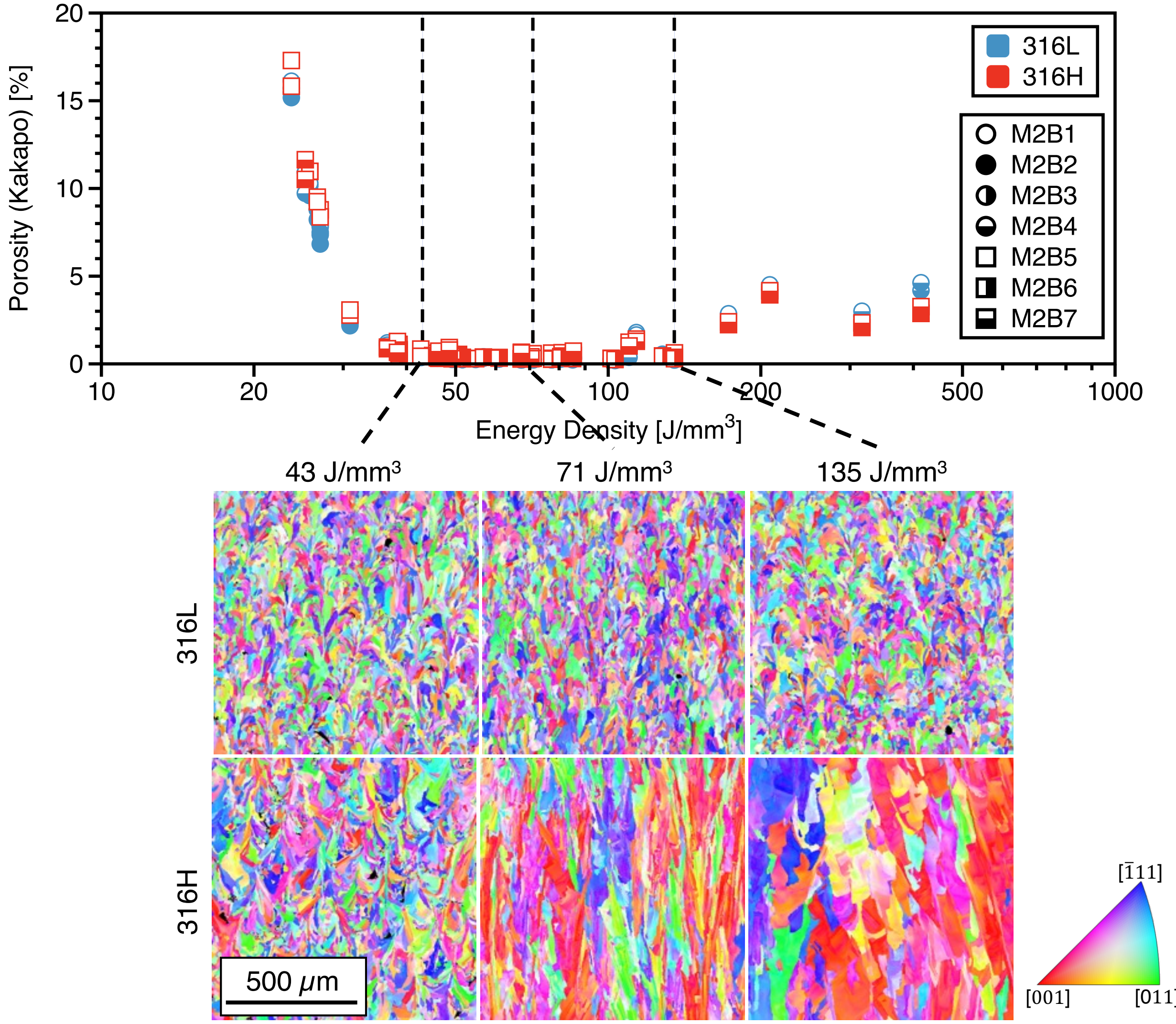

Figure 29. Variation of grain structure and orientation as a function of increasing energy density for 316L and 316H specimens printed on the concept laser within regions of acceptable porosity.

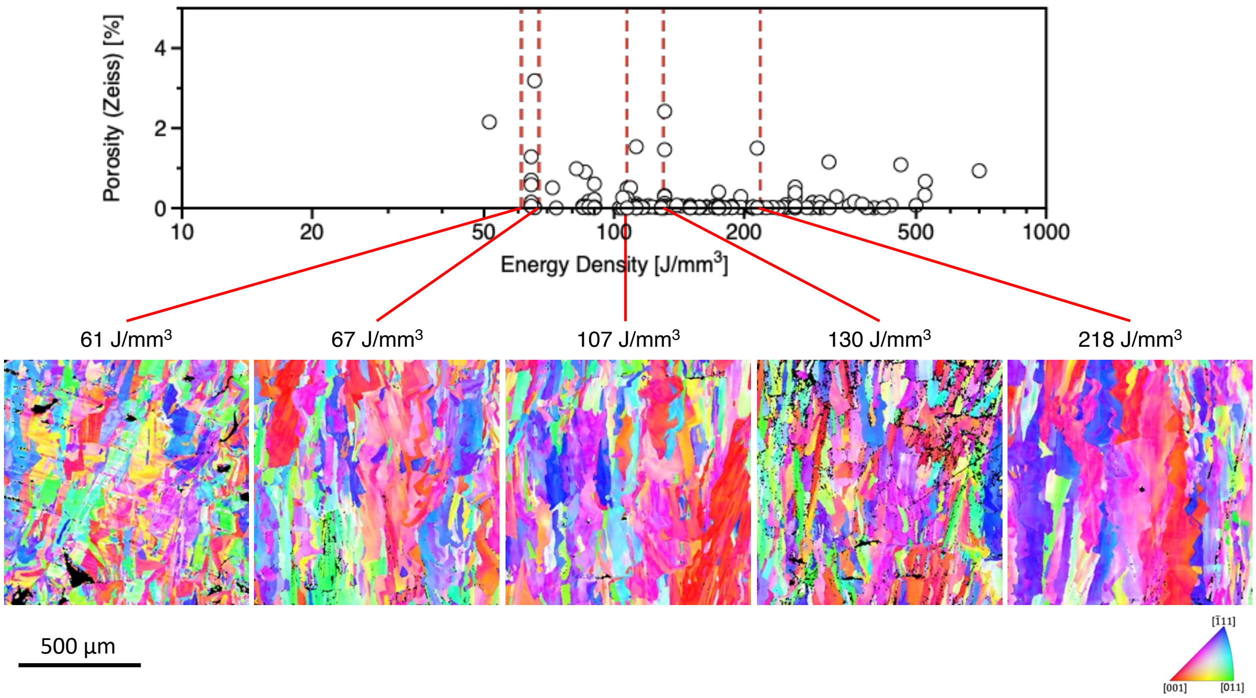

Figure 30. Variation of grain structure and orientation as a function of increasing energy density for 316H (AM316H-3) specimens printed on the Renishaw.

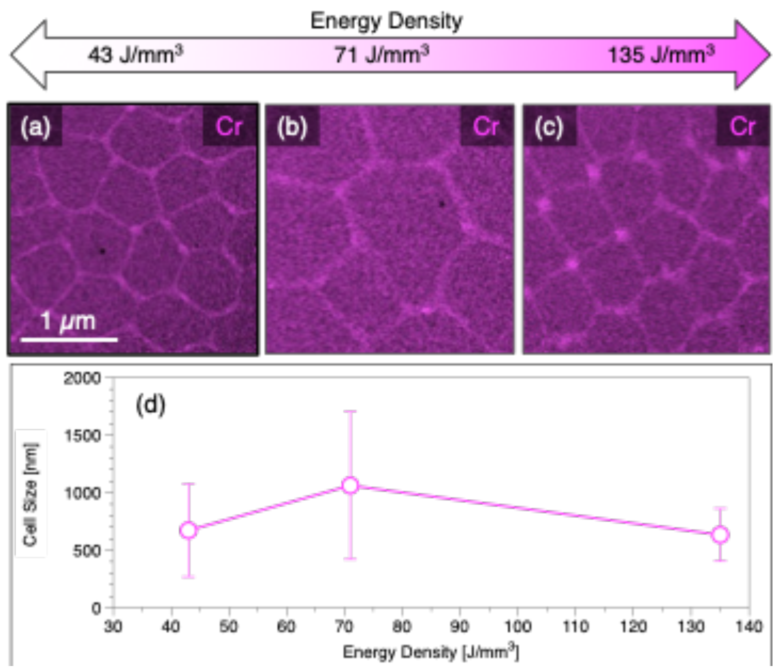

Figure 31. STEM+EDS maps of Cr enrichment along cells in (a) M2B5-P24, (b) M2B5-P35, and (c) M2B5-P7. Also shown in (d) is the relationship between measured cell size and energy density. Scale bar is identical in all STEM+EDS maps.

3.3.3 Effect of Build Geometry

From the above comparison of energy densities, all EBSD maps were extracted from the middle of the Zeiss specimen body. However, one important consideration warranting further investigation is the effect of build geometry on the characteristic microstructures expected during printing. To investigate this effect, EBSD maps were compared between two different "rods" printed atop the Zeiss geometry for a 316H sample with 52 J/mm^3 energy density. As shown in Figure 32, the grains in the 3 mm thick 1st rod were randomly oriented across the scan area, and their morphologies were close to equiaxed shape. However, the grains in 0.5 mm thick 4th rods were visibly elongated when the deposition path moved from bulk to rod section. Kernel average misorientation (KAM), which is a measure of orientation shift in grains due to increased geometrically necessary dislocation density, did not seem to be affected by rod thickness and was homogeneously distributed along the grain boundaries.

The difference in the grain elongation on these rods was most likely caused by an increased energy density per scan area that can change the cooling rates in these regions. During a layer-by-layer deposition, grain growth follows the heat flow, and grains epitaxially grow along the build direction. The pronounced elongation behavior in the thin rod could stem from increased cooling rates when compared with the thick rod. Shahabad et al. tested the wall thickness effect by L-PBF processing the 1–3 mm thick Hastelloy X walls and measured increased temperature gradient with reduced wall thickness [26]. The author also observed slightly reduced grain size and elongated grains in the thinnest walls.

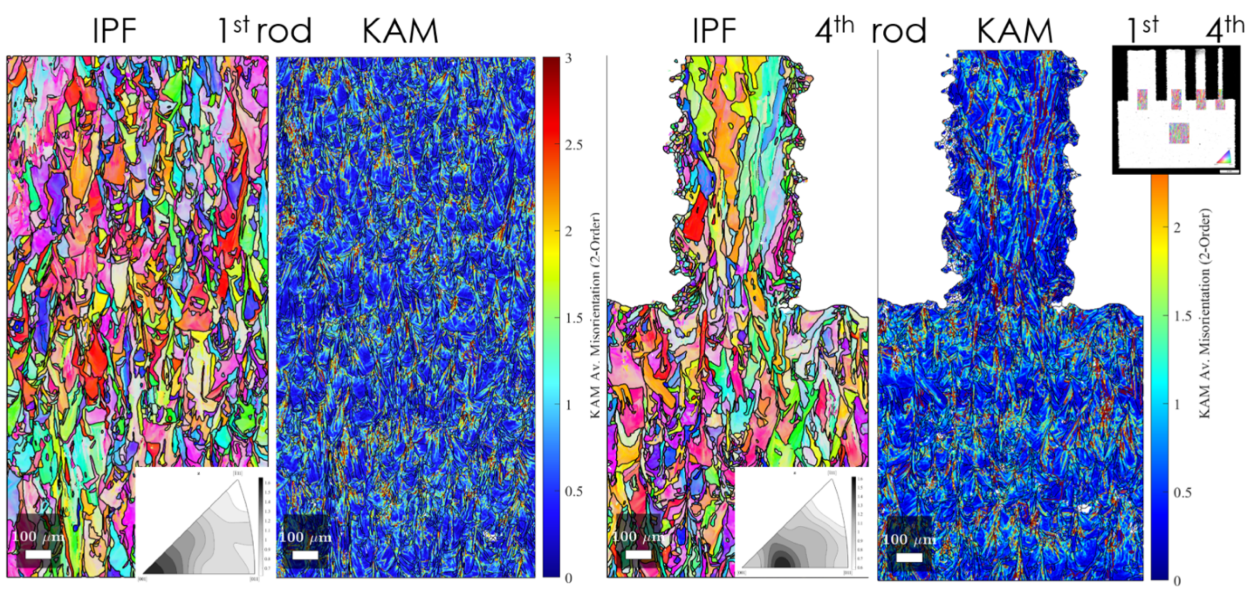

Figure 32. Grain morphology and texture changes within a single 316H (AM316H-3) sample printed on the concept laser (energy density ~52 J/mm3).

3.3.4 Ramifications on Mechanical Properties

Since the microstructure drives the mechanical response, 80 mechanical tests, including 70 316L and 30 316H samples, were conducted on the same specimens from which microstructural information was gathered. The total collection of data is presented in Figure 33. Note that in this figure, all SSJ3 data and all SST data are plotted to show qualitative comparisons of trends, although some SST data include simultaneous plotting of bulk and fin data together, thereby adding more scatter. Nevertheless, clear trends are resolvable using both specimen sizes. First, clearly visible with Renishaw samples and still somewhat resolvable from concept laser prints, the lowest energy density prints are associated with the poorest mechanical performance, which is attributed to the higher porosity from lack-of-fusion defects.

For the 316L and 316H samples printed on the concept laser, the ultimate tensile strength plateaus around 650 MPa when energy density approaches 50 J/mm^3. It is in this realm that both porosity and grain size are minimized, providing the highest grain boundary strengthening. This could invert at higher temperatures where grain boundary sliding may deteriorate creep performance. From mechanical testing results, although samples printed on the Renishaw reach a maximum strength around 50 J/mm^3 (which is the equivalent energy density of Renishaw-recommended 316L printing parameters), this energy density range was unstable for 316H samples printed on the same unit. Instead, combining both strength and ductility plots suggests an optimum range of 80–120 J/mm^3 for consistent performance. At increasing energy densities, the strength begins to slightly decline (less so for 316L samples), as the microstructure begins to shift to larger columnar grains in the 316H samples and as keyhole porosity reduces load bearing capacity in the gauge. This is true for both Renishaw and concept laser prints.

The true benefit from the subsized SST specimens, besides the ability to screen mechanical properties in smaller thin fins of the Zeiss specimen geometry, was the ability to assess the degree of anisotropy in the grains following the energy density–related morphology transformation in the 316HSS samples. For example, using samples #1–#2 (vertically oriented in Figure 13) and #5–#6 (horizontally oriented), SST specimens were tested in the bulk regions of the same 316HSS samples with microstructures illustrated in Figure 29. The comparative analysis, shown below in Figure 34, reveals the degree of anisotropy in each microstructure when loaded at room temperature. Due to the increasing grain size and preferred basal grain orientation in the build direction, the larger epitaxial grains in the 135 J/mm3 sample result in higher yield strength and strain hardening capacity in the transverse direction and less in the build direction. This degree of anisotropy decreases to almost unity in the lower energy density (43 J/mm3) sample. The orientation-dependent mechanical properties must be taken into consideration in both irradiation and mechanical testing work packages for eventual code qualification since anisotropy has been shown in this work to appear both as a function of printing parameters (composition and machine specific) and build geometry (part specific).

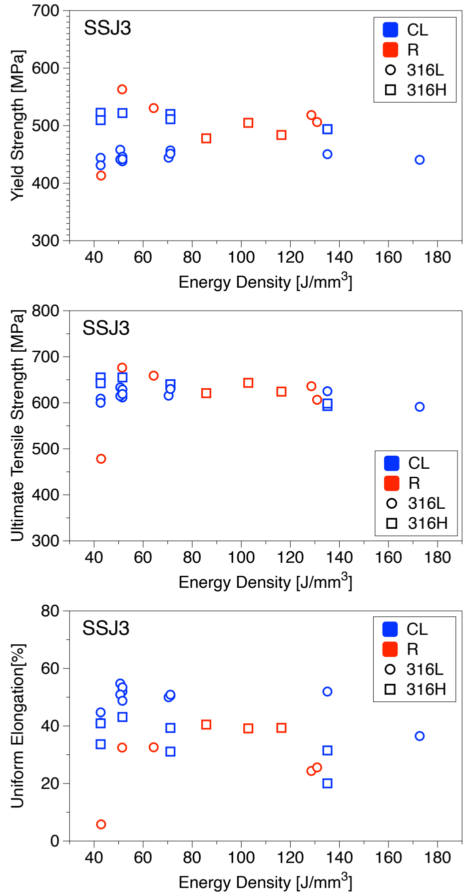

Figure 33. Collection of tensile results of 316L and 316H builds printed on both the concept laser and Renishaw tested using SSJ3 and SST tensile specimen geometries.

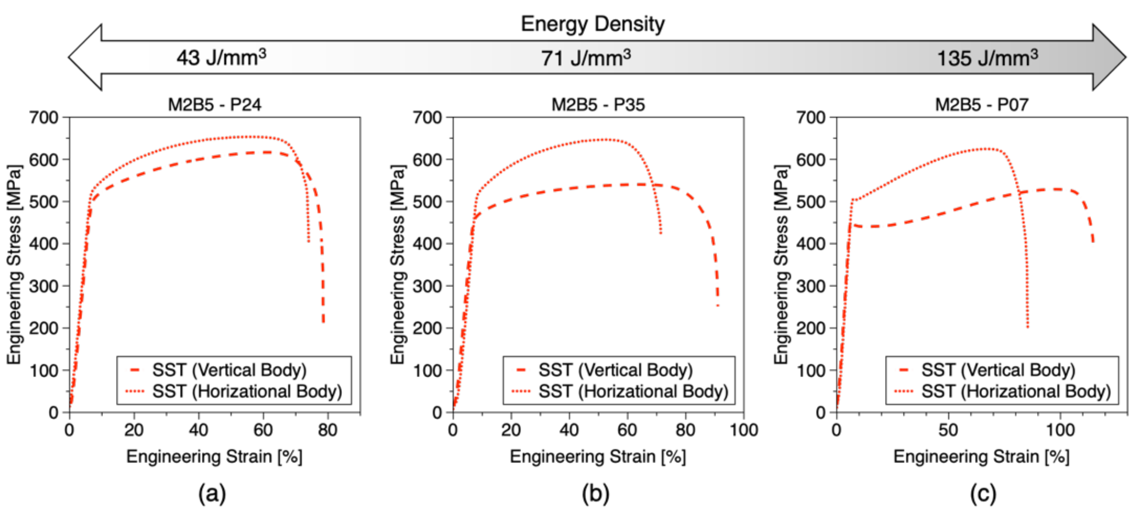

Figure 34. Subsized mechanical property data from SST specimens machined from the body of Zeiss specimens in the vertical (build direction) and horizontal (transverse direction) for samples printed with increasing energy density on the Concept Laser M2 from 316H powder (AM316H-3).

Unfortunately, the metadata comparisons do not capture the build geometry effects highlighted in the previous section. Since these effects may also serve to provide performance bounds for these parts, the Vickers hardness of 316H and 316L was measured to reveal the correlation between microstructural properties, and results are presented in Figure 35. According to that, the bulk sections of the 316H and 316L builds were measured to be on average approximately 220 HV and approximately 200 HV, respectively, and the hardness of both samples was reduced to 190 and 170 HV, respectively, when measurements were taken from rod sections. The slight loss of hardness in the 316L samples most likely originated from an increased pore formation on the rod section, while the 316H samples may show grain structure shift in the thin fins as well, further lowering the strength of the material. The slightly higher hardness measurement on 316H samples was probably caused by high retained strain in the 316H structure, as shown previously in examined KAM maps (Figure 32). In both materials, the samples produced with the lowest energy density showed slightly higher hardness, while the loss of hardness on the rods was more significant at 71 and 135 J/mm^3 energy density samples.

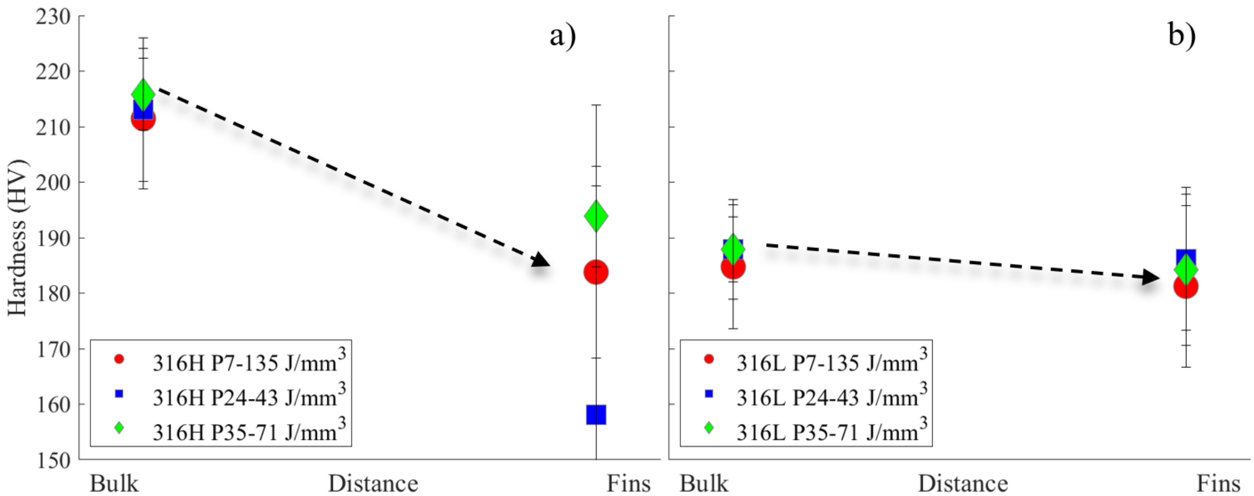

Figure 35. Hardness results for bulk and fin regions were given for (a) 316L and (b) 316L builds. The arrows show the changes in the general hardness trend from bulk to fin regions.

4. FUTURE WORK

4.1 FUTURE OPTIMIZATION AND ROUND-ROBIN TESTING

In the first year of this work package, significant advancement has been made in understanding the effect of composition, the importance of various processing parameters, and the extent to which in situ sensing and high-throughput characterization tools can be used to refine processing windows for LPBF 316HSS. However, significant gaps still exist in the ability to select optimal parameters for nuclear-relevant components. These gaps include (1) the effect of surface roughness, (2) an assessment of epitaxial vs. chevron grain structure performance, (3) the effect of heat treatment on subsequent thermal aging, (4) the extent to which Zeiss geometry "bulk" microstructures emulate larger components, and (5) machine-to-machine variations in part stability.

Work is ongoing to address the above questions, with the primary objective being identical builds performed at different laboratories to resolve the last of these gaps. Machine-to-machine variability is fundamentally the largest piece of uncertainty when evaluating a potential code qualification campaign, and a fundamental premise in its implementation would be that parts produced on any unit using the same parameters should produce the same characteristic microstructure as to enable the testing of a smaller subset of specimens from 2–3 different LPBF units for code case testing.

4.2 LARGER BUILDS FOR CAMPAIGN TESTING

After printing 252 samples on the Concept Laser and 390 on the Renishaw, ORNL has performed select larger builds for irradiations, thermal aging, and campaign testing. To date on the Concept Laser M2, three builds, titled "Tensile Blocks 01," "Tensile Blocks 02," and "Tensile Blocks 03" were printed using identical parameters for M2B5-P35, M2B6-P24, and M2B5-P24, respectively. A complete list of processing parameters used for these builds can be found in the appendix. All three builds utilized the 316H (AM316H-3) powder. The first build used an energy density of 71 J/mm^3, which should provide a columnar microstructure similar to that shown in Figure 29. The latter two builds used lower energy densities (52 J/mm^3 for Tensile Blocks 02 and 43 J/mm^3 for Tensile Blocks 03) and thus should have a refined grain structure with the chevron grain morphology.

Optical images for Tensile Blocks 01 are presented in Figure 36. Each build contained four Zeiss specimens, four small cubes (25.4 mm × 25.4 mm × 25.4 mm), two taller cuboids measured (25.4 mm × 25.4 mm × 101.6 mm), and four larger plates (13 mm × 95 mm × 101.6 mm). One of each of these geometries was subjected to three different heat treatments, as outlined in Table 5, with some specimens being allocated for irradiation testing, creep/creep-fatigue testing, and thermal aging. Specimens have been removed from the baseplate and are awaiting machining for FY24 activities. To date, the only larger 316H (AM316H-3) Renishaw build that has been performed used processing parameters identical to PA-6 (equivalent energy density 61 J/mm^3), which was an optimized printing condition for 316LSS (~0.18% porosity from XCT Kakapo segmentation). For future optimization, large builds are planned for parameters consistent with DOE builds PG-24 and PF-30, which can be referenced in Appendix Table A-2.

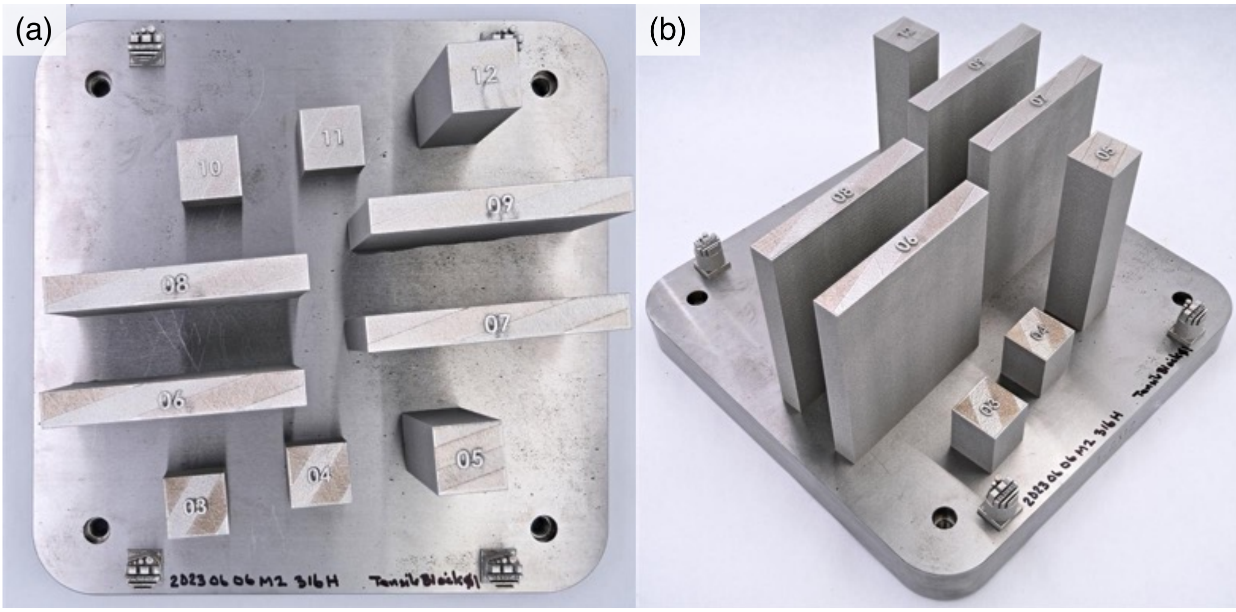

Figure 36. Optical images of build "Tensile Blocks 01" from the (a) top view and (b) isometric view.

Table 5. Material allocations from initial large builds

Build	Part	Dimensions	Geometry	Heat Treatment*	Purpose
Tensile Blocks XX	1	n/a	Zeiss	n/a	Unirradiated Properties
	2	n/a	Zeiss	HT1	Unirradiated Properties
	3	25.4 mm x 25.4 mm x 25.4 mm	Cube	n/a	Unirradiated Properties
	4	25.4 mm x 25.4 mm x 25.4 mm	Cube	HT1	Unirradiated Properties
	5	25.4 mm x 25.4 mm x 101.6 mm	Cuboid	HT1	Heterogeneity WP
	6	13 mm x 95 mm x 101.6 mm	Plate	HT1, HT2, HT3	HFIR Irradiation
	7	13 mm x 95 mm x 101.6 mm	Plate	HT1	Creep/Creep-Fatigue
	8	13 mm x 95 mm x 101.6 mm	Plate	HT2	Creep/Creep-Fatigue
	9	13 mm x 95 mm x 101.6 mm	Plate	HT3	Creep/Creep-Fatigue
	10	25.4 mm x 25.4 mm x 25.4 mm	Cube	HT2	Unirradiated Properties
	11	25.4 mm x 25.4 mm x 25.4 mm	Cube	HT3	Unirradiated Properties
	12	25.4 mm x 25.4 mm x 101.6 mm	Cuboid	HT1	Thermal Aging
	13	n/a	Zeiss	HT2	Unirradiated Properties
	14	n/a	Zeiss	HT3	Unirradiated Properties

* HT1 (Stress Relief, 650°C/24 h, air cooled), HT2 (Solution Anneal, 1,100°C/1 h, water quench), HT3 (HIP, 1150°C/100 MPa/4 h)

5. REFERENCES

[1] J. Clayton, D. Millington-Smith, B. Armstrong, The application of powder rheology in additive manufacturing, Jom 67(3) (2015) 544-548.

[2] Z. Wang, C. Jiang, P. Liu, W. Yang, Y. Zhao, M.F. Horstemeyer, L.-Q. Chen, Z. Hu, L. Chen, Uncertainty quantification and reduction in metal additive manufacturing, Npj Computational Materials 6(1) (2020) 175.

[3] P. Nandwana, A. Plotkowski, R. Kannan, S. Yoder, R. Dehoff, Predicting geometric influences in metal additive manufacturing, Materials Today Communications 25 (2020) 101174.

[4] I.F. Ituarte, E. Coatanea, M. Salmi, J. Tuomi, J. Partanen, Additive manufacturing in production: a study case applying technical requirements, Physics Procedia 78 (2015) 357-366.

[5] P.A. Hooper, Melt pool temperature and cooling rates in laser powder bed fusion, Additive Manufacturing 22 (2018) 548-559.

[6] Y.M. Wang, T. Voisin, J.T. McKeown, J. Ye, N.P. Calta, Z. Li, Z. Zeng, Y. Zhang, W. Chen, T.T. Roehling, Additively manufactured hierarchical stainless steels with high strength and ductility, Nature materials 17(1) (2018) 63-71.

[7] S. Dryepondt, P. Nandwana, P. Fernandez-Zelaia, F. List III, Microstructure and high temperature tensile properties of 316L fabricated by laser powder-bed fusion, Additive Manufacturing 37 (2021) 101723.

[8] A.J. Godfrey, J. Simpson, D. Leonard, K. Sisco, R. Dehoff, S. Babu, Heterogeneity and Solidification Pathways in Additively Manufactured 316L Stainless Steels, Metallurgical and Materials Transactions A 53(9) (2022) 3321-3340.

[9] S. Li, J. Hu, W.-Y. Chen, J. Yu, M. Li, Y. Wang, Evolution of cellular dislocation structures and defects in additively manufactured austenitic stainless steel under ion irradiation, Scripta Materialia 178 (2020) 245-250.

[10] P. Nandwana, R. Kannan, D.N. Leonard, Leveraging solute segregation in laser powder bed fusion to achieve superior strength and ductility via single-step heat treatment in Ti-free grade 300 maraging steel, JOM 72 (2020) 4221-4231.

[11] A. Committee, A. ASTM, 240/A 240M-04a: Standard specification for chromium and chromium-nickel stainless steel plate, sheet, and strip for pressure vessels and for general applications, ASTM International (2004).

[12] A. Ziabari, S. Venkatakrishnan, Z. Snow, A. Lisovich, M. Sprayberry, P. Brackman, C. Frederick, P. Bhattad, S. Graham, P. Bingham, Enabling rapid X-ray CT characterisation for additive manufacturing using CAD models and deep learning-based reconstruction, npj Computational Materials 9(1) (2023) 91.

[13] A. Ziabari, S. Venkatakrishnan, A. Dubey, A. Lisovich, P. Brackman, C. Frederick, P. Bhattad, P. Bingham, A. Plotkowski, R. Dehoff, Simurgh: A Framework for Cad-Driven Deep Learning Based X-Ray CT Reconstruction, 2022 IEEE International Conference on Image Processing (ICIP), IEEE, 2022, pp. 3836-3867.

[14] O. Ronneberger, P. Fischer, T. Brox, U-net: Convolutional networks for biomedical image segmentation, Medical Image Computing and Computer-Assisted Intervention–MICCAI 2015: 18th International Conference, Munich, Germany, October 5-9, 2015, Proceedings, Part III 18, Springer, 2015, pp. 234-241.

[15] R. Hielscher, T. Nyyssönen, F. Niessen, A.A. Gazder, The variant graph approach to improved parent grain reconstruction, Materialia 22 (2022) 101399.

[16] L. Scime, D. Siddel, S. Baird, V. Paquit, Layer-wise anomaly detection and classification for powder bed additive manufacturing processes: A machine-agnostic algorithm for real-time pixel-wise semantic segmentation, Additive Manufacturing 36 (2020) 101453.
[17] L. Scime, A. Singh, V. Paquit, A scalable digital platform for the use of digital twins in additive manufacturing, Manufacturing Letters 31 (2022) 28-32.
[18] R. Seede, D. Shoukr, B. Zhang, A. Whitt, S. Gibbons, P. Flater, A. Elwany, R. Arroyave, I. Karaman, An ultra-high strength martensitic steel fabricated using selective laser melting additive manufacturing: Densification, microstructure, and mechanical properties, Acta Materialia 186 (2020) 199-214.
[19] M. Grasso, B.M. Colosimo, Process defects and in situ monitoring methods in metal powder bed fusion: a review, Measurement Science and Technology 28(4) (2017) 044005.
[20] N. Ahmed, I. Barsoum, G. Haidemenopoulos, R.A. Al-Rub, Process parameter selection and optimization of laser powder bed fusion for 316L stainless steel: A review, Journal of Manufacturing Processes 75 (2022) 415-434.
[21] J.-B. Forien, N.P. Calta, P.J. DePond, G.M. Guss, T.T. Roehling, M.J. Matthews, Detecting keyhole pore defects and monitoring process signatures during laser powder bed fusion: A correlation between in situ pyrometry and ex situ X-ray radiography, Additive Manufacturing 35 (2020) 101336.
[22] Z. Hu, S. Gao, L. Zhang, X. Shen, H.L. Seet, S.M.L. Nai, J. Wei, Micro laser powder bed fusion of stainless steel 316L: Cellular structure, grain characteristics, and mechanical properties, Materials Science and Engineering: A 848 (2022) 143345.
[23] W.M. Tucho, V.H. Lysne, H. Austbø, A. Sjolyst-Kverneland, V. Hansen, Investigation of effects of process parameters on microstructure and hardness of SLM manufactured SS316L, Journal of Alloys and Compounds 740 (2018) 910-925.
[24] D. Kotecki, T. Siewert, WRC-1992 constitution diagram for stainless steel weld metals: a modification of the WRC-1988 diagram, Welding Journal 71(5) (1992) 171-178.
[25] V. Vukkum, J. Christudasjustus, A. Darwish, S. Storck, R. Gupta, Enhanced corrosion resistance of additively manufactured stainless steel by modification of feedstock, npj Materials Degradation 6(1) (2022) 2.
[26] S.I. Shahabad, U. Ali, Z. Zhang, A. Keshavarzkermani, R. Esmaeilizadeh, A. Bonakdar, E. Toyserkani, On the effect of thin-wall thickness on melt pool dimensions in laser powder-bed fusion of Hastelloy X: Numerical modeling and experimental validation, Journal of Manufacturing Processes 75 (2022) 435-449.

APPENDIX A: PRINTING PARAMETERS AND POROSITY MEASUREMENTS

Table A-1: Complete list of concept laser print parameters

Build	Part ID	Power (W)	Hatch Space (mm)	Velocity (mm/s)	Layer Thickness (µm)	Spot Size (µm)	Energy Density (J/mm^3)
M2B1, M2B2, M2B5	1	200	125	2250	50	125	14
M2B1, M2B2, M2B5	2	380	125	2250	50	125	27
M2B1, M2B2, M2B5	3	200	100	1500	50	125	27
M2B1, M2B2, M2B5	4	290	100	1500	50	125	39
M2B1, M2B2, M2B5	5	380	75	2250	50	125	45
M2B1, M2B2, M2B5	6	200	125	750	50	125	43
M2B1, M2B2, M2B5	7	380	75	750	50	125	135
M2B1, M2B2, M2B5	8	290	100	1500	50	125	39
M2B1, M2B2, M2B5	9	290	100	750	50	125	77
M2B1, M2B2, M2B5	10	200	75	2250	50	125	24
M2B1, M2B2, M2B5	11	380	100	1500	50	125	51
M2B1, M2B2, M2B5	12	290	75	1500	50	125	52
M2B1, M2B2, M2B5	13	290	125	1500	50	125	31
M2B1, M2B2, M2B5	14	290	100	1500	50	125	39
M2B1, M2B2, M2B5	15	290	100	1500	50	125	39
M2B1, M2B2, M2B5	16	290	100	2250	50	125	26
M2B1, M2B2, M2B5	17	200	75	750	50	125	71
M2B1, M2B2, M2B5	18	380	125	750	50	125	81
M2B1, M2B2, M2B5	19	200	125	2250	50	125	14
M2B1, M2B2, M2B5	20	380	125	2250	50	125	27
M2B1, M2B2, M2B5	21	200	100	1500	50	125	27
M2B1, M2B2, M2B5	22	290	100	1500	50	125	39
M2B1, M2B2, M2B5	23	380	75	2250	50	125	45
M2B1, M2B2, M2B5	24	200	125	750	50	125	43
M2B1, M2B2, M2B5	25	380	75	750	50	125	135
M2B1, M2B2, M2B5	26	290	100	1500	50	125	39
M2B1, M2B2, M2B5	27	290	100	750	50	125	77
M2B1, M2B2, M2B5	28	200	75	2250	50	125	24
M2B1, M2B2, M2B5	29	380	100	1500	50	125	51
M2B1, M2B2, M2B5	30	290	75	1500	50	125	52
M2B1, M2B2, M2B5	31	290	125	1500	50	125	31
M2B1, M2B2, M2B5	32	290	100	1500	50	125	39
M2B1, M2B2, M2B5	33	290	100	1500	50	125	39
M2B1, M2B2, M2B5	34	290	100	2250	50	125	26
M2B1, M2B2, M2B5	35	200	75	750	50	125	71
M2B1, M2B2, M2B5	36	380	125	750	50	125	81
M2B3, M2B6	1	335	88	1655	50	130	46
M2B3, M2B6	2	380	75	1500	50	130	68
M2B3, M2B6	3	271	88	1125	50	130	55
M2B3, M2B6	4	335	88	1125	50	130	68
M2B3, M2B6	5	335	88	595	50	130	128
M2B3, M2B6	6	290	75	1500	50	130	52
M2B3, M2B6	7	380	100	750	50	130	101
M2B3, M2B6	8	290	75	750	50	130	103
M2B3, M2B6	9	335	105	1125	50	130	57
M2B3, M2B6	10	380	100	1500	50	130	51
M2B3, M2B6	11	370	90	1350	50	130	61
M2B3, M2B6	12	335	88	1125	50	130	68
M2B3, M2B6	13	370	90	1350	50	130	61
M2B3, M2B6	14	290	100	750	50	130	77
M2B3, M2B6	15	290	100	1500	50	130	39
M2B3, M2B6	16	335	70	1125	50	130	85
M2B3, M2B6	17	399	88	1125	50	130	81
M2B3, M2B6	18	380	75	750	50	130	135
M2B3, M2B6	19	335	88	1655	50	130	46
M2B3, M2B6	20	380	75	1500	50	130	68
M2B3, M2B6	21	271	88	1125	50	130	55
M2B3, M2B6	22	335	88	1125	50	130	68
M2B3, M2B6	23	335	88	595	50	130	128
M2B3, M2B6	24	290	75	1500	50	130	52
M2B3, M2B6	25	380	100	750	50	130	101
M2B3, M2B6	26	290	75	750	50	130	103
M2B3, M2B6	27	335	105	1125	50	130	57
M2B3, M2B6	28	380	100	1500	50	130	51
M2B3, M2B6	29	370	90	1350	50	130	61
M2B3, M2B6	30	335	88	1125	50	130	68
M2B3, M2B6	31	370	90	1350	50	130	61
M2B3, M2B6	32	290	100	750	50	130	77
M2B3, M2B6	33	290	100	1500	50	130	39
M2B3, M2B6	34	335	70	1125	50	130	85
M2B3, M2B6	35	399	88	1125	50	130	81
M2B3, M2B6	36	380	75	750	50	130	135
M2B4, M2B7	1	250	110	1800	50	130	25
M2B4, M2B7	2	315	85	2021	50	130	37
M2B4, M2B7	3	380	60	1800	50	130	70
M2B4, M2B7	4	315	85	179	50	130	414

M2B4, M2B7	5	380	60	400	50	130	317
M2B4, M2B7	6	230	85	1100	50	130	49
M2B4, M2B7	7	380	110	400	50	130	173
M2B4, M2B7	8	380	110	1800	50	130	38
M2B4, M2B7	9	315	85	1100	50	130	67
M2B4, M2B7	10	315	85	1100	50	130	67
M2B4, M2B7	11	250	60	400	50	130	208
M2B4, M2B7	12	250	110	400	50	130	114
M2B4, M2B7	13	315	85	1100	50	130	67
M2B4, M2B7	14	315	85	1100	50	130	67
M2B4, M2B7	15	250	60	1800	50	130	46
M2B4, M2B7	16	315	52.1	1100	50	130	110
M2B4, M2B7	17	399	85	1100	50	130	85
M2B4, M2B7	18	315	117.9	1100	50	130	49
M2B4, M2B7	19	250	110	1800	50	130	25
M2B4, M2B7	20	315	85	2021	50	130	37
M2B4, M2B7	21	380	60	1800	50	130	70
M2B4, M2B7	22	315	85	179	50	130	414
M2B4, M2B7	23	380	60	400	50	130	317
M2B4, M2B7	24	230	85	1100	50	130	49
M2B4, M2B7	25	380	110	400	50	130	173
M2B4, M2B7	26	380	110	1800	50	130	38
M2B4, M2B7	27	315	85	1100	50	130	67
M2B4, M2B7	28	315	85	1100	50	130	67
M2B4, M2B7	29	250	60	400	50	130	208
M2B4, M2B7	30	250	110	400	50	130	114
M2B4, M2B7	31	315	85	1100	50	130	67
M2B4, M2B7	32	315	85	1100	50	130	67
M2B4, M2B7	33	250	60	1800	50	130	46
M2B4, M2B7	34	315	52.1	1100	50	130	110
M2B4, M2B7	35	399	85	1100	50	130	85
M2B4, M2B7	36	315	117.9	1100	50	130	49

Table A-2: Complete list of Renishaw print parameters

Build	Part ID	Laser Power (W)	Point Distance (µm)	Dwell Time (µs)	Hatch Spacing (µm)	Scan Speed (mm/s)	Energy Density (J/mm^3)	Layer Thickness (µm)	Scan Rotation	Stripe Width (mm)	Stripe Offset (µm)	Spot Size (µm)
PA	1	225	70	90	175	700	37	50	67	5	60	70
PA	2	225	130	90	105	1300	33	50	67	5	60	70
PA	3	75	70	90	105	700	20	50	67	5	60	70
PA	4	225	70	90	105	700	61	50	67	5	60	70
PA	5	225	10	90	105	100	429	50	67	5	60	70
PA	6	225	70	90	105	700	61	50	67	5	60	70
PA	7	225	70	90	35	700	184	50	67	5	60	70
PA	8	225	70	190	105	350	122	50	67	5	60	70
PA	9	225	70	40	105	1400	31	50	67	5	60	70
PA	10	375	70	90	105	700	102	50	67	5	60	70
PA	11	300	40	40	70	800	107	50	67	5	60	70
PA	12	225	70	90	105	700	61	50	67	5	60	70
PA	13	150	100	40	70	2000	21	50	67	5	60	70
PA	14	150	40	140	70	267	161	50	67	5	60	70
PA	15	150	100	140	140	667	32	50	67	5	60	70
PA	16	300	100	140	70	667	129	50	67	5	60	70
PA	17	225	70	90	105	700	61	50	67	5	60	70
PA	18	150	40	40	140	800	27	50	67	5	60	70
PA	19	300	40	140	140	267	161	50	67	5	60	70
PA	20	300	100	40	140	2000	21	50	67	5	60	70
PA	21	150	100	40	140	2000	11	50	67	5	60	70
PA	22	150	40	40	70	800	54	50	67	5	60	70
PA	23	150	40	140	140	267	80	50	67	5	60	70
PA	24	300	40	40	140	800	54	50	67	5	60	70
PA	25	300	100	40	70	2000	43	50	67	5	60	70
PA	26	300	100	140	140	667	64	50	67	5	60	70
PA	27	225	70	90	105	700	61	50	67	5	60	70
PA	28	150	100	140	70	667	64	50	67	5	60	70
PA	29	300	40	140	70	267	321	50	67	5	60	70
PA	30	225	70	90	105	700	61	50	67	5	60	70
PB	1	240	55	110	80	458	131	50	67	5	60	70
PB	2	200	70	80	100	778	51	50	67	5	60	70
PB	3	200	40	140	100	267	150	50	67	5	60	70
PB	4	240	55	110	80	458	131	50	67	5	60	70
PB	5	280	70	140	100	467	120	50	67	5	60	70
PB	6	280	40	80	100	444	126	50	67	5	60	70
PB	7	200	70	140	60	467	143	50	67	5	60	70
PB	8	200	40	80	60	444	150	50	67	5	60	70
PB	9	280	70	80	60	778	120	50	67	5	60	70
PB	10	280	40	140	60	267	350	50	67	5	60	70
PB	11	200	40	140	60	267	250	50	67	5	60	70
PB	12	280	70	140	60	467	200	50	67	5	60	70
PB	13	200	40	80	100	444	90	50	67	5	60	70
PB	14	280	40	80	60	444	210	50	67	5	60	70
PB	15	280	40	140	100	267	210	50	67	5	60	70
PB	16	240	55	110	80	458	131	50	67	5	60	70
PB	17	200	70	140	100	467	86	50	67	5	60	70
PB	18	280	70	80	100	778	72	50	67	5	60	70
PB	19	200	70	80	60	778	86	50	67	5	60	70
PB	20	240	55	110	80	458	131	50	67	5	60	70
PB	21	240	55	110	80	458	131	50	67	5	60	70
PB	22	320	55	110	80	458	175	50	67	5	60	70
PB	23	240	55	50	80	917	65	50	67	5	60	70
PB	24	240	55	170	80	306	196	50	67	5	60	70
PB	25	160	55	110	80	458	87	50	67	5	60	70
PB	26	240	85	110	80	708	85	50	67	5	60	70
PB	27	240	55	110	120	458	87	50	67	5	60	70
PB	28	240	25	110	80	208	288	50	67	5	60	70
PB	29	240	55	110	40	458	262	50	67	5	60	70
PB	30	240	55	110	80	458	131	50	67	5	60	70
PC	1	280	70	80	80	778	90	50	67	5	60	70
PC	2	200	70	140	80	467	107	50	67	5	60	70
PC	3	280	40	80	80	444	263	30	67	5	60	70
PC	4	240	55	110	80	458	164	40	67	5	60	70
PC	5	200	40	80	80	444	113	50	67	5	60	70
PC	6	200	70	80	80	778	107	30	67	5	60	70
PC	7	280	40	140	80	267	263	50	67	5	60	70
PC	8	280	70	140	80	467	250	30	67	5	60	70
PC	9	240	55	110	80	458	164	40	67	5	60	70
PC	10	200	40	140	80	267	313	30	67	5	60	70
PC	11	240	55	50	80	917	82	40	67	5	60	70
PC	12	320	55	110	80	458	218	40	67	5	60	70
PC	13	240	55	110	80	458	164	40	67	5	60	70
PC	14	240	55	110	80	458	109	60	67	5	60	70
PC	15	240	55	170	80	306	245	40	67	5	60	70
PC	16	240	55	110	80	458	164	40	67	5	60	70
PC	17	160	55	110	80	458	109	40	67	5	60	70
PC	18	240	25	110	80	208	360	40	67	5	60	70
PC	19	240	85	110	80	708	106	40	67	5	60	70

PC	20	240	55	110	80	458	327	20	67	5	60	70
PC	21	280	70	140	80	467	150	50	67	5	60	70
PC	22	200	40	140	80	267	188	50	67	5	60	70
PC	23	280	70	80	80	778	150	30	67	5	60	70
PC	24	200	70	80	80	778	64	50	67	5	60	70
PC	25	240	55	110	80	458	164	40	67	5	60	70
PC	27	280	40	140	80	267	438	30	67	5	60	70
PC	28	240	55	110	80	458	164	40	67	5	60	70
PC	29	280	40	80	80	444	158	50	67	5	60	70
PC	30	200	40	80	80	444	188	30	67	5	60	70
PC	26	200	70	140	80	467	179	30	67	5	60	70
PD	1	240	55	110	80	458	131	50	67	5	60	75
PD	2	240	85	110	80	708	85	50	67	5	60	105
PD	3	240	55	110	80	458	131	50	67	5	60	135
PD	4	160	55	110	80	458	87	50	67	5	60	105
PD	5	320	55	110	80	458	175	50	67	5	60	105
PD	6	240	55	170	80	306	196	50	67	5	60	105
PD	7	240	55	110	80	458	131	50	67	5	60	105
PD	8	240	55	50	80	917	65	50	67	5	60	105
PD	9	240	55	110	80	458	131	50	67	5	60	105
PD	10	240	25	110	80	208	288	50	67	5	60	105
PD	11	200	40	140	80	267	188	50	67	5	60	90
PD	12	200	70	140	80	467	107	50	67	5	60	120
PD	13	280	70	80	80	778	90	50	67	5	60	120
PD	14	200	40	80	80	444	113	50	67	5	60	120
PD	15	240	55	110	80	458	131	50	67	5	60	105
PD	16	280	70	140	80	467	150	50	67	5	60	90
PD	17	200	70	80	80	778	64	50	67	5	60	90
PD	18	280	40	140	80	267	263	50	67	5	60	120
PD	19	240	55	110	80	458	131	50	67	5	60	105
PD	20	280	40	80	80	444	158	50	67	5	60	90
PD	21	280	40	140	80	267	263	50	67	5	60	90
PD	22	280	70	140	80	467	150	50	67	5	60	120
PD	23	280	70	80	80	778	90	50	67	5	60	90
PD	24	200	70	80	80	778	64	50	67	5	60	120
PD	25	200	40	140	80	267	188	50	67	5	60	120
PD	26	280	40	80	80	444	158	50	67	5	60	120
PD	27	200	70	140	80	467	107	50	67	5	60	90
PD	28	240	55	110	80	458	131	50	67	5	60	105
PD	29	240	55	110	80	458	131	50	67	5	60	105
PD	30	200	40	80	80	444	113	50	67	5	60	90
PE	1	240	55	50	80	917	65	50	67	5	60	70
PE	2	240	25	110	80	208	288	50	67	5	60	70
PE	3	240	55	110	80	458	131	50	67	9	60	70
PE	4	320	55	110	80	458	175	50	67	5	60	70
PE	5	240	55	110	80	458	131	50	67	5	60	70
PE	6	160	55	110	80	458	87	50	67	5	60	70
PE	7	240	85	110	80	708	85	50	67	5	60	70
PE	8	240	55	110	80	458	131	50	67	1	60	70
PE	9	240	55	110	80	458	131	50	67	5	60	70
PE	10	240	55	170	80	306	196	50	67	5	60	70
PE	11	240	55	110	80	458	131	50	67	5	60	70
PE	12	200	70	140	80	467	107	50	67	7	60	70
PE	13	280	40	140	80	267	263	50	67	7	60	70
PE	14	200	70	80	80	778	64	50	67	3	60	70
PE	15	200	40	80	80	444	113	50	67	7	60	70
PE	16	280	40	80	80	444	158	50	67	3	60	70
PE	17	240	55	110	80	458	131	50	67	5	60	70
PE	18	280	70	80	80	778	90	50	67	7	60	70
PE	19	200	40	140	80	267	188	50	67	3	60	70
PE	20	280	70	140	80	467	150	50	67	3	60	70
PE	21	240	55	110	80	458	131	50	67	5	60	70
PE	22	240	55	110	80	458	131	50	67	5	60	70
PE	23	280	70	80	80	778	90	50	67	3	60	70
PE	24	200	70	80	80	778	64	50	67	7	60	70
PE	25	200	40	140	80	267	188	50	67	7	60	70
PE	26	280	70	140	80	467	150	50	67	7	60	70
PE	27	280	40	140	80	267	263	50	67	3	60	70
PE	28	200	40	80	80	444	113	50	67	3	60	70
PE	29	200	70	140	80	467	107	50	67	3	60	70
PE	30	280	40	80	80	444	158	50	67	7	60	70
PF	1	280	70	80	80	778	103	50	70	5	60	70
PF	2	200	40	140	80	267	500	50	30	5	60	70
PF	3	200	70	80	80	778	171	50	30	5	60	70
PF	4	280	70	140	80	467	400	50	30	5	60	70
PF	5	280	40	80	80	444	420	50	30	5	60	70
PF	6	200	70	140	80	467	122	50	70	5	60	70
PF	7	200	40	80	80	444	129	50	70	5	60	70
PF	8	240	55	110	80	458	209	50	50	5	60	70
PF	9	240	55	110	80	458	209	50	50	5	60	70
PF	10	280	40	140	80	267	300	50	70	5	60	70
PF	11	280	40	140	80	267	700	50	30	5	60	70
PF	12	280	40	80	80	444	180	50	70	5	60	70
PF	13	200	40	80	80	444	300	50	30	5	60	70

PF	14	240	55	110	80	458	209	50	50	5	60	70
PF	15	200	70	80	80	778	73	50	70	5	60	70
PF	16	200	40	140	80	267	214	50	70	5	60	70
PF	17	280	70	80	80	778	240	50	30	5	60	70
PF	18	280	70	140	80	467	171	50	70	5	60	70
PF	19	240	55	110	80	458	209	50	50	5	60	70
PF	20	200	70	140	80	467	286	50	30	5	60	70
PF	21	240	55	170	80	306	314	50	50	5	60	70
PF	22	320	55	110	80	458	279	50	50	5	60	70
PF	23	240	25	110	80	208	461	50	50	5	60	70
PF	24	240	55	110	80	458	209	50	50	5	60	70
PF	25	240	55	50	80	917	105	50	50	5	60	70
PF	26	240	85	110	80	708	136	50	50	5	60	70
PF	27	240	55	110	80	458	116	50	90	5	60	70
PF	28	240	55	110	80	458	209	50	50	5	60	70
PF	29	240	55	110	80	458	1047	50	10	5	60	70
PF	30	160	55	110	80	458	140	50	50	5	60	70
PG	1	240	55	110	80	458	175	50	67	5	60	70
PG	2	240	85	110	80	708	113	50	67	5	60	70
PG	3	320	55	110	80	458	233	50	67	5	60	70
PG	4	160	55	110	80	458	116	50	67	5	60	70
PG	5	240	55	110	80	458	175	50	67	5	60	70
PG	6	240	55	50	80	917	87	50	67	5	60	70
PG	7	240	25	110	80	208	384	50	67	5	60	70
PG	8	240	55	170	80	306	262	50	67	5	60	70
PG	9	240	55	110	80	458	524	50	67	5	20	70
PG	10	240	55	110	80	458	105	50	67	5	100	70
PG	11	280	40	80	80	444	158	50	67	5	80	70
PG	12	200	40	80	80	444	225	50	67	5	40	70
PG	13	200	70	140	80	467	214	50	67	5	40	70
PG	14	200	40	140	80	267	188	50	67	5	80	70
PG	15	240	55	110	80	458	175	50	67	5	60	70
PG	16	280	40	140	80	267	525	50	67	5	40	70
PG	17	280	70	80	80	778	180	50	67	5	40	70
PG	18	200	70	80	80	778	64	50	67	5	80	70
PG	19	240	55	110	80	458	175	50	67	5	60	70
PG	20	280	70	140	80	467	150	50	67	5	80	70
PG	21	280	70	140	80	467	300	50	67	5	40	70
PG	22	200	40	80	80	444	113	50	67	5	80	70
PG	23	200	70	140	80	467	107	50	67	5	80	70
PG	24	280	70	80	80	778	90	50	67	5	80	70
PG	25	280	40	140	80	267	263	50	67	5	80	70
PG	26	200	40	140	80	267	375	50	67	5	40	70
PG	27	200	70	80	80	778	129	50	67	5	40	70
PG	28	240	55	110	80	458	175	50	67	5	60	70
PG	29	280	40	80	80	444	315	50	67	5	40	70
PG	30	240	55	110	80	458	175	50	67	5	60	70

Table A-3: XCT porosity analysis summary (Concept Laser M2)

Build	Zeiss Segmentation						Kakapo Segmentation						
								52 Micron Surface Avoided			104 Micron Surface Avoided		
	Part ID	All	Rods	Fins	Inclines	Body	Full	Full Porosity	True Porosity	Surface Porosity	Full Porosity	True Porosity	Surface Porosity
M2B1	1	1.30	2.94	2.22	1.29	1.24	32.89	31.91	33.20	0.98	31.12	33.58	1.77
M2B1	2	4.48	12.12	11.33	20.10	4.20	16.12	15.39	16.00	0.72	14.93	16.10	1.19
M2B1	3	3.42	8.69	8.66	14.23	3.23	0.50	0.20	0.21	0.29	0.10	0.11	0.40
M2B1	4	0.25	0.44	0.75	0.87	0.24	0.34	0.08	0.09	0.25	0.04	0.04	0.30
M2B1	5	0.26	0.45	0.48	0.79	0.27	2.85	2.43	2.53	0.41	2.19	2.36	0.65
M2B1	6	0.01	0.03	0.12	0.05	0.01	0.70	0.39	0.41	0.31	0.28	0.30	0.42
M2B1	7	0.03	0.46	0.41	0.24	0.01	0.70	0.37	0.38	0.33	0.26	0.28	0.45
M2B1	8	0.31	0.58	0.74	1.18	0.30	10.16	9.54	9.91	0.62	9.14	9.84	1.02
M2B1	9												
M2B1	10	4.20	5.63	4.22	3.83	4.58	0.27	0.04	0.04	0.23	0.01	0.01	0.26
M2B1	11	0.02	0.10	0.31	0.11	0.01	0.40	0.18	0.18	0.22	0.07	0.08	0.33
M2B1	12	0.02	0.03	0.07	0.04	0.02	32.06	31.08	32.33	0.98	30.31	32.71	1.74
M2B1	13	1.73	6.05	4.45	8.58	1.53	7.81	7.24	7.52	0.57	6.88	7.42	0.93
M2B1	14	0.18	0.45	0.62	0.79	0.17	7.36	6.78	7.04	0.58	6.43	6.93	0.92
M2B1	15	0.25	0.84	0.83	1.10	0.23	8.80	8.27	8.59	0.53	7.97	8.57	0.83
M2B1	16	5.30	8.80	8.04	11.75	5.67	0.66	0.35	0.36	0.31	0.26	0.28	0.41
M2B1	17	0.00	0.00	0.02	0.01	0.00	0.49	0.21	0.22	0.28	0.15	0.16	0.34
M2B1	18	0.05	0.60	0.94	0.23	0.03	0.36	0.09	0.09	0.28	0.02	0.03	0.34
M2B1	19	1.27	3.78	2.08	1.42	1.21	0.35	0.14	0.14	0.21	0.10	0.11	0.25
M2B1	20	5.63	13.32	12.35	21.59	5.44	0.69	0.37	0.38	0.32	0.27	0.29	0.42
M2B1	21	5.06	10.21	10.13	15.68	5.11	0.28	0.06	0.06	0.22	0.02	0.02	0.26
M2B1	22	0.14	0.38	0.51	0.63	0.13	15.48	14.79	15.37	0.69	14.33	15.45	1.14
M2B1	23	0.14	0.25	0.41	0.43	0.14	0.46	0.15	0.16	0.31	0.06	0.07	0.40
M2B1	24	0.01	0.01	0.11	0.04	0.01	9.31	8.77	9.10	0.54	8.44	9.08	0.87
M2B1	25	0.02	0.27	0.10	0.14	0.02	0.34	0.09	0.09	0.25	0.04	0.04	0.31
M2B1	26	0.24	0.72	0.68	0.94	0.22	2.97	2.56	2.66	0.41	2.33	2.51	0.64
M2B1	27	0.00	0.03	0.07	0.02	0.00	0.75	0.46	0.47	0.29	0.35	0.38	0.40
M2B1	28	3.82	5.12	4.18	4.01	4.27	0.72	0.41	0.43	0.31	0.32	0.34	0.41
M2B1	29	0.03	0.18	0.35	0.11	0.02	10.30	9.70	10.08	0.60	9.33	10.05	0.97
M2B1	30	0.01	0.01	0.03	0.03	0.01	0.28	0.05	0.05	0.23	0.03	0.03	0.25
M2B1	31	1.95	7.95	5.04	10.07	1.69	0.41	0.14	0.15	0.27	0.05	0.05	0.36
M2B1	32	0.26	0.70	0.75	0.92	0.24	0.75	0.45	0.47	0.30	0.34	0.37	0.41
M2B1	33	0.29	0.80	0.72	1.15	0.27	0.63	0.33	0.34	0.30	0.26	0.28	0.37
M2B1	34	4.63	8.67	8.43	10.18	4.87	0.38	0.10	0.10	0.29	0.03	0.03	0.35
M2B1	35	0.03	0.00	0.03	0.00	0.03	0.29	0.14	0.14	0.15	0.10	0.11	0.19
M2B1	36	0.04	0.44	0.71	0.17	0.02	0.68	0.37	0.38	0.32	0.26	0.28	0.42
M2B2	1	1.33	3.16	1.91	1.45	1.27	32.52	31.52	32.81	1.00	30.71	33.17	1.81
M2B2	2	4.64	12.41	11.26	20.91	4.34	15.71	15.00	15.58	0.71	14.50	15.61	1.22
M2B2	3	4.91	10.29	9.13	16.90	4.96	0.54	0.23	0.24	0.31	0.12	0.13	0.42
M2B2	4	0.16	0.50	0.73	0.77	0.13	0.33	0.08	0.08	0.25	0.03	0.03	0.30
M2B2	5	0.27	0.33	0.70	0.85	0.27	2.18	1.79	1.86	0.38	1.60	1.72	0.58
M2B2	6	0.00	0.01	0.05	0.02	0.00	0.59	0.29	0.30	0.30	0.18	0.20	0.40
M2B2	7	0.02	0.49	0.27	0.17	0.01	0.61	0.28	0.29	0.32	0.18	0.20	0.42
M2B2	8	0.19	0.44	0.67	0.83	0.17	9.60	9.02	9.36	0.58	8.66	9.32	0.94
M2B2	9	0.01	0.06	0.10	0.04	0.00	0.48	0.19	0.19	0.29	0.07	0.08	0.40
M2B2	10	4.17	4.82	3.80	3.58	4.56	32.20	31.19	32.46	1.01	30.40	32.81	1.80
M2B2	11	0.08	0.41	0.92	0.42	0.06	7.49	6.91	7.18	0.58	6.52	7.01	0.98
M2B2	12	0.01	0.02	0.05	0.02	0.01	6.83	6.26	6.50	0.58	5.90	6.36	0.93
M2B2	13	1.56	6.24	4.24	7.86	1.37	8.22	7.69	7.99	0.53	7.37	7.95	0.85
M2B2	14	0.16	0.66	0.69	0.76	0.15	0.58	0.27	0.28	0.31	0.17	0.18	0.41
M2B2	15	0.20	0.50	0.74	0.81	0.18	0.47	0.21	0.21	0.27	0.14	0.15	0.33
M2B2	16	4.98	8.74	9.37	13.52	5.18	0.40	0.09	0.09	0.31	0.02	0.03	0.37
M2B2	17												
M2B2	18	0.02	0.24	0.52	0.17	0.01	0.35	0.13	0.13	0.23	0.09	0.09	0.26
M2B2	19	1.66	2.95	2.25	1.57	1.64	0.60	0.30	0.32	0.30	0.19	0.21	0.41
M2B2	20	4.36	13.89	12.48	19.53	3.90	0.30	0.06	0.06	0.24	0.02	0.02	0.28
M2B2	21	4.56	11.52	10.14	17.79	4.44	15.18	14.50	15.06	0.68	14.05	15.13	1.13
M2B2	22	0.03	0.11	0.19	0.17	0.02	0.50	0.19	0.19	0.31	0.08	0.09	0.42
M2B2	23	0.15	0.38	0.48	0.48	0.14	8.79	8.25	8.57	0.54	7.89	8.49	0.90
M2B2	24	0.01	0.03	0.11	0.02	0.01	0.32	0.10	0.10	0.22	0.04	0.05	0.28
M2B2	25	0.02	0.35	0.28	0.19	0.01	2.33	2.01	2.09	0.31	1.82	1.95	0.51
M2B2	26	0.05	0.16	0.30	0.23	0.04	0.63	0.31	0.32	0.31	0.21	0.23	0.42
M2B2	27	0.00	0.00	0.03	0.01	0.00	0.62	0.31	0.32	0.31	0.21	0.23	0.41
M2B2	28	4.04	4.83	4.18	3.55	4.42	9.60	9.03	9.38	0.57	8.66	9.33	0.94
M2B2	29	0.05	0.29	0.70	0.26	0.03	0.23	0.04	0.04	0.19	0.01	0.01	0.21
M2B2	30	0.01	0.04	0.04	0.02	0.02	0.45	0.18	0.19	0.27	0.07	0.07	0.39
M2B2	31	1.42	5.80	3.99	6.77	1.26	0.64	0.33	0.35	0.31	0.22	0.24	0.42
M2B2	32	0.03	0.11	0.15	0.14	0.02	0.63	0.33	0.34	0.30	0.25	0.27	0.38
M2B2	33	0.20	0.52	0.66	0.83	0.18	0.38	0.10	0.10	0.28	0.03	0.03	0.35
M2B2	34	4.69	8.44	10.06	11.69	4.84	0.38	0.16	0.16	0.22	0.11	0.12	0.27
M2B2	35	0.00	0.00	0.02	0.01	0.00	0.63	0.33	0.35	0.30	0.22	0.24	0.41
M2B2	36	0.05	0.46	0.96	0.23	0.02	0.33	0.07	0.07	0.26	0.02	0.02	0.31
M2B3	1	0.07	0.29	0.54	0.28	0.03	0.34	0.15	0.15	0.19	0.09	0.10	0.25
M2B3	2	0.12	0.51	0.31	0.50	0.13	0.38	0.15	0.16	0.23	0.10	0.11	0.28
M2B3	3	0.00		0.06	0.03	0.00	0.27	0.06	0.06	0.21	0.02	0.02	0.25
M2B3	4	0.01	0.07	0.15	0.04	0.00	0.26	0.06	0.07	0.20	0.02	0.02	0.24
M2B3	5	0.16	2.14	1.55	1.08	0.09	0.55	0.39	0.40	0.16	0.34	0.36	0.21

M2B3	6	0.01	0.04	0.06	0.01	0.00	0.24	0.06	0.06	0.18	0.02	0.02	0.22
M2B3	7	0.03	0.22	0.42	0.17	0.01	0.30	0.10	0.10	0.20	0.05	0.05	0.25
M2B3	8	0.04	0.11	0.10	0.10	0.03	0.21	0.06	0.06	0.15	0.03	0.03	0.18
M2B3	9	0.02	0.07	0.34	0.08	0.00	0.40	0.16	0.17	0.24	0.07	0.07	0.33
M2B3	10	0.10	0.31	1.10	0.35	0.04	0.45	0.21	0.21	0.24	0.11	0.12	0.34
M2B3	11	0.01	0.12	0.15	0.06	0.00	0.30	0.09	0.09	0.21	0.03	0.04	0.26
M2B3	12	0.01	0.07	0.10	0.04	0.00	0.26	0.06	0.06	0.20	0.02	0.02	0.24
M2B3	13	0.03	0.24	0.45	0.22	0.02	0.31	0.09	0.10	0.22	0.04	0.04	0.28
M2B3	14	0.01	0.10	0.13	0.03	0.00	0.23	0.05	0.05	0.19	0.02	0.02	0.22
M2B3	15	0.04	0.23	0.38	0.36	0.03	0.47	0.23	0.24	0.24	0.16	0.17	0.31
M2B3	16	0.05	0.02	0.02	0.08	0.07	0.30	0.12	0.13	0.18	0.09	0.09	0.22
M2B3	17	0.07	1.14	0.59	0.22	0.05	0.35	0.14	0.14	0.21	0.06	0.07	0.29
M2B3	18	0.08	0.56	0.82	0.68	0.04	0.31	0.14	0.15	0.17	0.11	0.11	0.20
M2B3	19	0.04	0.49	0.38	0.22	0.03	0.31	0.11	0.11	0.21	0.05	0.05	0.27
M2B3	20	0.03	0.01	0.22	0.08	0.03	0.24	0.07	0.07	0.17	0.03	0.03	0.21
M2B3	21	0.01	0.03	0.06	0.02	0.00	0.25	0.05	0.06	0.20	0.02	0.02	0.23
M2B3	22	0.02	0.07	0.09	0.03	0.00	0.26	0.06	0.07	0.20	0.02	0.03	0.24
M2B3	23	0.07	0.79	0.54	0.82	0.04	0.44	0.28	0.29	0.16	0.24	0.26	0.20
M2B3	24	0.01	0.01	0.13	0.05	0.01	0.24	0.05	0.05	0.19	0.02	0.02	0.23
M2B3	25	0.00	0.05	0.06	0.03	0.00	0.23	0.06	0.06	0.18	0.02	0.02	0.21
M2B3	26	0.00	0.01	0.01	0.01	0.00	0.19	0.03	0.03	0.17	0.01	0.01	0.18
M2B3	27	0.02	0.11	0.41	0.10	0.01	0.32	0.10	0.10	0.22	0.03	0.03	0.29
M2B3	28	0.01	0.04	0.17	0.05	0.00	0.36	0.12	0.13	0.23	0.05	0.05	0.31
M2B3	29	0.01	0.02	0.10	0.03	0.00	0.28	0.07	0.08	0.21	0.02	0.02	0.26
M2B3	30	0.05	0.04	0.13	0.03	0.00	0.27	0.07	0.07	0.20	0.04	0.04	0.23
M2B3	31	0.04	0.09	0.11	0.04	0.00	0.28	0.07	0.07	0.21	0.03	0.03	0.25
M2B3	32	0.02	0.17	0.19	0.03	0.00	0.23	0.05	0.05	0.19	0.01	0.02	0.22
M2B3	33	0.08	0.29	0.44	0.63	0.05	0.55	0.30	0.31	0.25	0.22	0.24	0.32
M2B3	34	0.01	0.00	0.01	0.00	0.01	0.23	0.05	0.05	0.18	0.02	0.02	0.21
M2B3	35	0.01	0.23	0.13	0.04	0.00	0.27	0.06	0.07	0.21	0.02	0.02	0.25
M2B3	36	0.04	1.16	0.35	0.40	0.02	0.22	0.08	0.09	0.14	0.06	0.06	0.16
M2B4	1	6.31	22.33	10.63	11.78	6.80	10.92	10.43	10.79	0.49	10.12	10.80	0.80
M2B4	2	0.41	1.94	1.30	2.55	0.36	1.20	0.95	0.98	0.25	0.86	0.92	0.34
M2B4	3	0.09	0.18	0.09	0.19	0.10	0.30	0.12	0.12	0.18	0.08	0.09	0.22
M2B4	4	2.49	27.37	15.36	28.28	1.13	4.19	3.96	4.08	0.23	3.88	4.12	0.31
M2B4	5	1.63	20.45	8.89	17.28	0.77	2.71	2.49	2.57	0.22	2.41	2.57	0.30
M2B4	6	0.00	0.01	0.05	0.02	0.00	0.26	0.06	0.06	0.21	0.02	0.02	0.25
M2B4	7	1.09	10.72	6.55	8.11	0.76	2.58	2.40	2.47	0.19	2.32	2.47	0.26
M2B4	8	0.16	0.80	0.80	0.79	0.13	0.77	0.48	0.50	0.29	0.37	0.39	0.40
M2B4	9	0.00	0.00	0.04	0.01	0.00	0.25	0.05	0.05	0.20	0.01	0.01	0.24
M2B4	10	0.01	0.07	0.12	0.04	0.01	0.25	0.05	0.05	0.20	0.01	0.02	0.24
M2B4	11	2.47	17.37	15.55	19.31	1.64	4.21	4.02	4.15	0.19	3.95	4.21	0.26
M2B4	12	0.57	8.46	3.85	5.95	0.29	1.79	1.60	1.65	0.19	1.53	1.62	0.26
M2B4	13	0.00		0.05	0.02	0.00	0.22	0.06	0.06	0.17	0.02	0.02	0.21
M2B4	14	0.00	0.00	0.05	0.01	0.00	0.25	0.05	0.05	0.20	0.01	0.01	0.24
M2B4	15	0.01		0.07	0.07	0.01	0.32	0.12	0.12	0.20	0.08	0.08	0.24
M2B4	16	0.51	0.06	0.04	0.21	0.65	0.89	0.67	0.69	0.22	0.62	0.67	0.26
M2B4	17	0.09	1.56	0.47	0.18	0.08	0.37	0.14	0.14	0.24	0.07	0.08	0.30
M2B4	18	0.01	0.07	0.23	0.08	0.01	0.41	0.16	0.16	0.25	0.06	0.06	0.35
M2B4	19	6.33	12.95	12.22	14.94	6.78	9.72	9.24	9.55	0.49	8.92	9.51	0.81
M2B4	20	0.73	2.49	2.02	3.91	0.68	1.07	0.81	0.84	0.26	0.73	0.78	0.34
M2B4	21	0.03		0.05	0.04	0.03	0.25	0.09	0.09	0.16	0.06	0.06	0.19
M2B4	22	2.67	32.98	20.00	30.58	1.16	4.63	4.43	4.57	0.19	4.35	4.62	0.28
M2B4	23	1.94	13.99	10.41	19.77	0.99	3.00	2.80	2.89	0.20	2.73	2.91	0.27
M2B4	24	0.01	0.01	0.07	0.02	0.00	0.26	0.05	0.05	0.21	0.01	0.01	0.24
M2B4	25	0.69	5.02	3.96	5.65	0.47	2.86	2.68	2.76	0.18	2.60	2.76	0.26
M2B4	26	0.06	0.27	0.40	0.31	0.05	0.68	0.42	0.43	0.27	0.31	0.33	0.37
M2B4	27	0.00	0.01	0.06	0.01	0.00	0.24	0.05	0.05	0.19	0.01	0.01	0.23
M2B4	28	0.01	0.00	0.04	0.02	0.01	0.23	0.05	0.05	0.18	0.01	0.02	0.22
M2B4	29	2.72	16.92	18.82	18.43	1.95	4.51	4.32	4.46	0.19	4.24	4.52	0.26
M2B4	30	0.53	5.07	3.45	5.22	0.28	1.65	1.49	1.54	0.16	1.42	1.51	0.23
M2B4	31	0.00	0.00	0.02	0.00	0.00	0.24	0.04	0.05	0.19	0.01	0.01	0.23
M2B4	32	0.01	0.00	0.12	0.01	0.00	0.25	0.05	0.05	0.19	0.02	0.02	0.23
M2B4	33	0.07	0.23	0.25	0.31	0.05	0.33	0.11	0.12	0.22	0.08	0.08	0.25
M2B4	34	0.12	0.01	0.03	0.08	0.15	0.38	0.18	0.19	0.19	0.15	0.16	0.22
M2B4	35	0.01	0.05	0.12	0.03	0.00	0.28	0.07	0.07	0.21	0.03	0.03	0.26
M2B4	36	0.04		0.49	0.25	0.03	0.39	0.16	0.16	0.23	0.06	0.07	0.33
M2B5	1	1.24	1.78	2.39	1.30	1.24	35.10	33.83	35.40	1.27	32.85	35.80	2.24
M2B5	2	4.74	15.67	11.90	20.58	4.33	8.78	8.18	8.52	0.60	7.77	8.42	1.01
M2B5	3	5.22	16.33	11.85	18.17	5.02	9.50	8.93	9.31	0.58	8.58	9.30	0.93
M2B5	4	0.03	0.09	0.28	0.26	0.02	0.75	0.43	0.44	0.33	0.31	0.33	0.45
M2B5	5	0.02	0.13	0.08	0.12	0.01	0.60	0.30	0.31	0.30	0.22	0.24	0.38
M2B5	6	0.01	0.04	0.16	0.05	0.00	0.84	0.54	0.56	0.31	0.43	0.46	0.42
M2B5	7	0.03	0.76	0.47	0.22	0.01	0.63	0.39	0.40	0.24	0.32	0.35	0.30
M2B5	8	0.04	0.15	0.32	0.27	0.03	1.11	0.78	0.81	0.33	0.64	0.69	0.47
M2B5	9	0.00	0.02	0.06	0.02	0.00	0.61	0.35	0.36	0.26	0.29	0.31	0.33
M2B5	10	4.94	5.36	3.97	4.18	5.81	17.29	16.54	17.24	0.75	16.03	17.36	1.27
M2B5	11	0.08	0.69	1.14	0.51	0.04	0.54	0.24	0.25	0.30	0.13	0.14	0.41
M2B5	12	0.01	0.01	0.07	0.03	0.00	0.37	0.11	0.11	0.27	0.05	0.05	0.33
M2B5	13	0.36	2.58	1.48	2.89	0.24	2.78	2.37	2.46	0.41	2.15	2.32	0.63
M2B5	14	0.07	0.33	0.43	0.51	0.05	0.82	0.50	0.51	0.32	0.37	0.40	0.45
M2B5	15	0.06	0.33	0.43	0.39	0.03	0.80	0.51	0.53	0.29	0.38	0.41	0.43
M2B5	16	5.14	12.77	10.69	16.73	5.09	10.97	10.36	10.76	0.61	9.94	10.71	1.03
M2B5	17	0.00	0.00	0.02	0.01	0.00	0.58	0.34	0.35	0.24	0.30	0.32	0.28

M2B5	18	0.03	0.21	0.43	0.17	0.01	0.64	0.34	0.35	0.30	0.22	0.24	0.42
M2B5	19	1.12	2.26	1.82	1.42	1.10	34.97	33.79	35.27	1.17	32.91	35.69	2.06
M2B5	20	4.61	15.28	12.27	20.25	4.08	8.38	7.77	8.10	0.60	7.39	7.99	0.99
M2B5	21	3.98	13.50	10.87	17.12	3.90	9.25	8.68	9.02	0.57	8.35	9.02	0.90
M2B5	22	0.00	0.02	0.02	0.05	0.00	0.60	0.28	0.29	0.32	0.18	0.20	0.42
M2B5	23	0.01	0.04	0.08	0.06	0.01	0.47	0.17	0.17	0.31	0.09	0.10	0.39
M2B5	24	0.00	0.09	0.02	0.01	0.00	0.43	0.12	0.12	0.32	0.04	0.04	0.39
M2B5	25	0.01	0.15	0.11	0.10	0.01	0.37	0.15	0.16	0.22	0.10	0.11	0.27
M2B5	26	0.05	0.25	0.34	0.34	0.03	0.63	0.31	0.32	0.32	0.21	0.23	0.42
M2B5	27	0.00	0.01	0.03	0.01	0.00	0.32	0.07	0.08	0.24	0.02	0.03	0.29
M2B5	28	4.32	7.24	6.77	7.27	4.89	15.83	15.09	15.72	0.74	14.58	15.80	1.24
M2B5	29	0.01	0.07	0.22	0.08	0.00	0.48	0.17	0.18	0.30	0.07	0.08	0.41
M2B5	30	0.00	0.00	0.02	0.02	0.00	0.36	0.07	0.08	0.28	0.02	0.03	0.33
M2B5	31	0.46	2.11	2.09	3.36	0.36	3.07	2.63	2.74	0.44	2.43	2.61	0.64
M2B5	32	0.06	0.30	0.35	0.59	0.04	0.69	0.35	0.36	0.34	0.24	0.26	0.45
M2B5	33	0.02	0.11	0.19	0.24	0.01	0.70	0.36	0.38	0.34	0.25	0.27	0.44
M2B5	34	2.14	9.13	7.99	11.68	1.87	10.98	10.34	10.76	0.63	9.96	10.76	1.02
M2B5	35	0.00	0.00	0.00	0.00	0.00	0.32	0.07	0.08	0.24	0.03	0.03	0.29
M2B5	36	0.02	0.21	0.45	0.11	0.01	0.45	0.16	0.17	0.28	0.06	0.07	0.39
M2B6	1	0.03	0.13	0.29	0.22	0.02	0.38	0.12	0.13	0.26	0.05	0.06	0.32
M2B6	2	0.05	0.36	0.18	0.20	0.05							
M2B6	3	0.00	0.00	0.00	0.00	0.00	0.31	0.07	0.07	0.23	0.02	0.02	0.28
M2B6	4	0.01	0.08	0.24	0.07	0.01	0.32	0.09	0.10	0.23	0.03	0.04	0.28
M2B6	5	0.15	2.35	2.00	1.51	0.08	0.45	0.28	0.29	0.18	0.22	0.24	0.23
M2B6	6	0.01	0.03	0.12	0.04	0.01	0.31	0.07	0.07	0.24	0.02	0.02	0.28
M2B6	7	0.03	0.29	0.51	0.17	0.01	0.32	0.10	0.10	0.22	0.05	0.05	0.27
M2B6	8	0.01	0.11	0.13	0.09	0.00	0.27	0.08	0.08	0.20	0.04	0.04	0.23
M2B6	9	0.03	0.14	0.51	0.18	0.01	0.39	0.14	0.14	0.25	0.05	0.05	0.34
M2B6	10	0.01	0.09	0.33	0.15	0.01	0.44	0.16	0.17	0.28	0.07	0.08	0.37
M2B6	11	0.02	0.11	0.40	0.11	0.01	0.36	0.10	0.10	0.26	0.03	0.04	0.32
M2B6	12	0.01	0.13	0.22	0.05	0.00	0.31	0.07	0.08	0.23	0.02	0.02	0.29
M2B6	13	0.02	0.28	0.33	0.13	0.01	0.36	0.11	0.11	0.25	0.04	0.04	0.32
M2B6	14	0.01	0.03	0.13	0.03	0.00	0.27	0.06	0.06	0.21	0.02	0.02	0.25
M2B6	15	0.11	0.75	0.63	0.81	0.09	0.50	0.23	0.24	0.26	0.14	0.15	0.36
M2B6	16	0.09	0.10	0.02	0.07	0.13	0.39	0.16	0.16	0.24	0.11	0.12	0.28
M2B6	17	0.06	0.70	0.46	0.22	0.06	0.41	0.16	0.16	0.25	0.08	0.09	0.33
M2B6	18	0.06	1.59	1.04	0.52	0.03	0.33	0.15	0.16	0.18	0.10	0.11	0.23
M2B6	19	0.03	0.14	0.28	0.14	0.02	0.35	0.09	0.10	0.25	0.04	0.04	0.31
M2B6	20	0.01	0.03	0.08	0.04	0.01	0.32	0.08	0.09	0.24	0.04	0.04	0.28
M2B6	21	0.01	0.04	0.11	0.02	0.00	0.30	0.06	0.06	0.24	0.02	0.02	0.29
M2B6	22	0.00	0.03	0.08	0.02	0.00	0.31	0.07	0.08	0.24	0.02	0.03	0.29
M2B6	23	0.11	1.68	1.49	1.05	0.06	0.43	0.26	0.26	0.17	0.20	0.21	0.23
M2B6	24	0.01	0.00	0.07	0.02	0.00	0.30	0.07	0.07	0.23	0.02	0.02	0.28
M2B6	25	0.02	0.23	0.35	0.10	0.01	0.30	0.09	0.09	0.22	0.04	0.04	0.27
M2B6	26	0.00	0.01	0.02	0.02	0.00	0.25	0.06	0.06	0.19	0.03	0.03	0.22
M2B6	27	0.00	0.00	0.00	0.00	0.00	0.37	0.11	0.12	0.26	0.04	0.04	0.33
M2B6	28	0.03	0.23	0.55	0.21	0.02	0.41	0.14	0.15	0.27	0.06	0.06	0.36
M2B6	29	0.01	0.04	0.31	0.08	0.01	0.33	0.09	0.10	0.24	0.03	0.03	0.30
M2B6	30	0.00	0.04	0.08	0.02	0.00	0.31	0.07	0.07	0.24	0.02	0.02	0.29
M2B6	31	0.00	0.01	0.05	0.02	0.00	0.33	0.08	0.09	0.25	0.03	0.03	0.31
M2B6	32	0.01	0.04	0.08	0.02	0.00	0.28	0.05	0.06	0.22	0.02	0.02	0.26
M2B6	33	0.18	0.79	0.94	1.42	0.15	0.59	0.31	0.32	0.29	0.21	0.23	0.38
M2B6	34	0.03	0.01	0.13	0.02	0.03	0.31	0.08	0.09	0.22	0.04	0.05	0.26
M2B6	35	0.02	0.07	0.25	0.08	0.01	0.35	0.10	0.10	0.25	0.04	0.04	0.31
M2B6	36	0.03	0.43	0.36	0.34	0.01	0.30	0.11	0.11	0.19	0.07	0.07	0.23
M2B7	1	6.32	10.49	7.94	12.15	7.16	11.64	11.07	11.49	0.57	10.70	11.50	0.94
M2B7	2	0.24	1.23	0.88	1.85	0.21	0.96	0.66	0.69	0.29	0.57	0.61	0.38
M2B7	3	0.08	0.22	0.10	0.36	0.07	0.40	0.17	0.17	0.24	0.12	0.13	0.28
M2B7	4	1.82	14.62	20.90	14.97	0.79	2.88	2.60	2.68	0.28	2.50	2.66	0.38
M2B7	5	1.33	17.58	5.71	12.46	0.80	2.07	1.82	1.88	0.25	1.73	1.84	0.35
M2B7	6	0.01	0.11	0.11	0.03	0.01	0.30	0.07	0.07	0.24	0.02	0.02	0.28
M2B7	7	1.21	10.88	7.84	8.77	0.90	2.24	2.02	2.09	0.22	1.93	2.07	0.30
M2B7	8	0.22	1.16	1.52	1.45	0.18	1.28	0.96	0.99	0.32	0.82	0.88	0.45
M2B7	9	0.01	0.02	0.12	0.03	0.00	0.30	0.07	0.07	0.23	0.02	0.02	0.28
M2B7	10	0.01	0.07	0.20	0.04	0.01	0.66	0.42	0.43	0.24	0.37	0.39	0.30
M2B7	11	2.45	16.61	16.40	18.77	1.77	3.94	3.73	3.85	0.21	3.65	3.90	0.29
M2B7	12	0.65	7.24	6.07	6.73	0.30	1.41	1.21	1.25	0.21	1.13	1.21	0.28
M2B7	13	0.01	0.02	0.15	0.03	0.01	0.29	0.06	0.07	0.23	0.02	0.02	0.27
M2B7	14	0.01	0.01	0.41	0.02	0.00	0.29	0.06	0.06	0.23	0.02	0.02	0.27
M2B7	15	0.03	0.05	0.21	0.17	0.02	0.32	0.09	0.10	0.22	0.05	0.05	0.27
M2B7	16	0.75	0.06	0.01	0.09	1.06	1.24	0.98	1.02	0.25	0.93	1.00	0.31
M2B7	17	0.14	0.77	0.48	0.84	0.15	0.48	0.22	0.22	0.27	0.14	0.15	0.34
M2B7	18	0.03	0.15	0.61	0.20	0.01	0.93	0.64	0.66	0.30	0.52	0.56	0.41
M2B7	19	6.30	16.42	9.62	16.01	7.11	10.52	9.95	10.32	0.56	9.59	10.30	0.93
M2B7	20	0.46	1.16	1.84	3.20	0.41	0.87	0.55	0.57	0.32	0.46	0.49	0.41
M2B7	21	0.03	0.16	0.09	0.05	0.04	0.30	0.09	0.10	0.20	0.05	0.06	0.24
M2B7	22	2.11	17.90	15.25	19.65	0.98	3.26	2.97	3.07	0.29	2.86	3.05	0.41
M2B7	23	1.56	19.38	7.09	14.19	0.96	2.34	2.10	2.17	0.24	2.00	2.14	0.34
M2B7	24	0.01	0.02	0.14	0.04	0.00	0.30	0.06	0.07	0.23	0.02	0.02	0.28
M2B7	25	1.34	10.82	8.40	9.67	1.03	2.40	2.20	2.27	0.20	2.11	2.26	0.29
M2B7	26	0.21	0.83	1.33	1.33	0.18	0.66	0.36	0.38	0.29	0.25	0.27	0.40
M2B7	27	0.01	0.01	0.16	0.03	0.00	0.30	0.07	0.07	0.23	0.02	0.02	0.27
M2B7	28	0.01	0.06	0.15	0.03	0.01	0.29	0.06	0.07	0.23	0.02	0.02	0.27
M2B7	29	2.63	13.95	17.62	19.93	2.04	4.17	3.94	4.08	0.23	3.85	4.12	0.32

M2B7	30	0.52	5.02	4.98	5.94	0.22	1.29	1.08	1.12	0.20	1.00	1.08	0.28
M2B7	31	0.00	0.04	0.15	0.01	0.00	0.28	0.06	0.06	0.22	0.02	0.02	0.26
M2B7	32	0.06	0.35	0.37	0.14	0.04	0.62	0.33	0.34	0.30	0.23	0.25	0.39
M2B7	33	0.06	0.40	0.50	0.23	0.04	0.72	0.41	0.43	0.31	0.30	0.32	0.43
M2B7	34	0.47	0.31	0.41	0.45	0.60	1.02	0.71	0.73	0.32	0.60	0.65	0.42
M2B7	35	0.19	0.57	0.78	0.45	0.18	0.73	0.39	0.40	0.34	0.26	0.28	0.47
M2B7	36	0.05	0.27	0.48	0.25	0.03	0.79	0.43	0.44	0.36	0.27	0.29	0.52

Table A-4: XCT porosity analysis summary (Renishaw)

Build	Material	Zeiss Segmentation						Kakapo Segmentation						
									52 Micron Surface Avoided			104 Micron Surface Avoided		
		Part ID	All	Rods	Fins	Inclines	Stdev (Spread)	All	Full Porosity	True Porosity	Surface Porosity	Full Porosity	True Porosity	Surface Porosity
PA	316L	1	4.10	7.07	6.77	14.12	3.37	7.86	7.28	7.57	0.58	6.98	7.53	0.88
PA	316L	2	4.08	6.57	3.82	8.23	1.81	9.10	8.56	8.90	0.54	8.26	8.90	0.84
PA	316L	3	3.12	3.86	3.59	2.60	0.47	17.41	16.68	17.34	0.73	16.14	17.41	1.27
PA	316L	4	0.19	1.24	1.18	1.33	0.46	0.72	0.34	0.36	0.38	0.21	0.23	0.51
PA	316L	5	1.13	5.60	2.90	8.77	2.77	2.33	1.90	1.98	0.42	1.77	1.90	0.56
PA	316L	6	0.02	0.02	0.12	0.06	0.05	0.55	0.17	0.18	0.38	0.06	0.07	0.48
PA	316L	7	0.04	0.66	0.25	0.28	0.25	0.51	0.18	0.18	0.33	0.08	0.09	0.43
PA	316L	8	0.02	0.47	0.15	0.14	0.19	0.43	0.12	0.12	0.31	0.06	0.06	0.37
PA	316L	9	3.71	2.03	1.01	1.17	1.23	16.69	15.91	16.57	0.78	15.39	16.66	1.29
PA	316L	10	0.02	0.15	0.31	0.08	0.12	0.86	0.33	0.35	0.53	0.11	0.12	0.75
PA	316L	11	0.02	0.06	0.21	0.09	0.09	0.47	0.12	0.13	0.35	0.04	0.04	0.43
PA	316L	12	0.01	0.03	0.08	0.02	0.03	0.49	0.12	0.13	0.36	0.03	0.03	0.46
PA	316L	13	3.59	2.14	1.95	2.00	0.78	23.70	22.85	23.77	0.85	22.20	23.98	1.50
PA	316L	14	0.02	0.65	0.15	0.09	0.29	0.50	0.15	0.15	0.35	0.07	0.08	0.43
PA	316L	15	3.37	5.10	5.84	8.11	1.50	7.42	6.85	7.13	0.56	6.54	7.07	0.87
PA	316L	16	0.02	0.49	0.16	0.11	0.20	0.48	0.13	0.13	0.35	0.05	0.05	0.44
PA	316L	17	0.01	0.13	0.14	0.05	0.06	0.48	0.12	0.12	0.37	0.03	0.03	0.45
PA	316L	18	3.52	2.71	2.09	2.48	0.66	16.10	15.32	15.94	0.78	14.79	15.99	1.31
PA	316L	19	0.02	0.29	0.19	0.09	0.11	0.76	0.26	0.27	0.49	0.09	0.09	0.67
PA	316L	20	2.05	2.57	1.04	1.53	0.71	29.38	28.19	29.53	1.19	27.35	29.92	2.03
PA	316L	21												
PA	316L	22	1.12	3.53	2.95	5.58	1.48	2.56	2.25	2.34	0.30	2.16	2.33	0.39
PA	316L	23	0.02	0.39	0.04	0.07	0.18	0.46	0.16	0.16	0.30	0.10	0.11	0.35
PA	316L	24	3.34	2.78	3.10	10.11	2.89	6.11	5.54	5.76	0.58	5.25	5.67	0.87
PA	316L	25	2.60	2.59	2.69	4.27	0.65	6.96	6.42	6.67	0.54	6.12	6.61	0.84
PA	316L	26	0.02	0.24	0.25	0.12	0.10	0.61	0.19	0.20	0.42	0.06	0.06	0.55
PA	316L	27	0.02	0.28	0.32	0.07	0.13	0.41	0.10	0.10	0.31	0.03	0.03	0.38
PA	316L	28	0.43	0.69	0.82	1.74	0.45	0.71	0.42	0.44	0.29	0.37	0.39	0.34
PA	316L	29	0.46	0.49	1.82	0.98	0.67	1.75	1.23	1.28	0.52	1.05	1.13	0.70
PA	316L	30	0.03	0.24	0.28	0.24	0.10	0.58	0.18	0.19	0.40	0.06	0.06	0.52
PB	316L	1	0.48	0.41	0.14	0.18	0.22	1.09	0.82	0.85	0.27	0.75	0.81	0.34
PB	316L	2	0.17	0.51	0.51	0.54	0.31	0.52	0.24	0.24	0.29	0.17	0.18	0.36
PB	316L	3	0.71	0.63	0.15	0.22	0.38	2.85	2.61	2.70	0.24	2.53	2.72	0.32
PB	316L	4	0.02	0.34	0.11	0.04	0.26	0.46	0.14	0.14	0.32	0.06	0.06	0.40
PB	316L	5	0.01	0.09	0.08	0.03	0.06							
PB	316L	6	0.21	0.11	0.08	0.06	0.07	1.18	0.91	0.95	0.27	0.84	0.90	0.34
PB	316L	7	0.53	0.56	0.15	0.13	0.29	1.34	1.07	1.11	0.26	1.00	1.07	0.34
PB	316L	8	0.04	0.23	0.07	0.06	0.14	0.51	0.21	0.21	0.30	0.13	0.14	0.38
PB	316L	9	0.01	0.03	0.07	0.02	0.03	0.59	0.20	0.20	0.39	0.07	0.08	0.51
PB	316L	10	0.31	0.58	0.17	0.50	0.21	1.15	0.76	0.79	0.39	0.65	0.69	0.50
PB	316L	11	3.29	5.30	5.16	5.41	1.49	6.01	5.79	6.00	0.22	5.70	6.12	0.32
PB	316L	12	1.04	0.40	0.23	0.29	0.32	2.34	2.04	2.12	0.30	1.94	2.09	0.40
PB	316L	13	0.01	0.06	0.09	0.02	0.05	0.31	0.09	0.09	0.23	0.03	0.03	0.28
PB	316L	14	0.06	0.24	0.09	0.09	0.16	0.65	0.29	0.30	0.36	0.18	0.20	0.47
PB	316L	15	0.14	0.54	0.08	0.17	0.26	0.73	0.41	0.43	0.32	0.32	0.34	0.42
PB	316L	16	0.67	0.95	0.60	0.59	0.46	1.42	1.17	1.21	0.25	1.10	1.18	0.32
PB	316L	17	0.18	0.28	0.10	0.12	0.20	0.61	0.34	0.36	0.26	0.29	0.31	0.32
PB	316L	18	0.01	0.02	0.12	0.03	0.06	0.45	0.13	0.13	0.32	0.03	0.03	0.42
PB	316L	19	0.02	0.03	0.12	0.03	0.05							
PB	316L	20	0.02	0.16	0.06	0.04	0.11	0.44	0.16	0.16	0.29	0.08	0.09	0.36
PB	316L	21	0.41	0.75	0.37	0.71	0.21	1.46	1.24	1.29	0.22	1.17	1.25	0.30
PB	316L	22	0.58	0.30	0.08	0.13	0.20	1.98	1.66	1.72	0.32	1.56	1.68	0.42
PB	316L	23	0.09	0.03	0.11	0.03	0.05	0.42	0.11	0.12	0.31	0.04	0.04	0.38
PB	316L	24	0.52	0.98	0.14	0.37	0.45	1.07	0.76	0.79	0.32	0.67	0.72	0.40
PB	316L	25	0.30	0.13	0.08	0.09	0.11	0.74	0.51	0.53	0.23	0.45	0.49	0.29
PB	316L	26	0.08	0.49	0.13	0.10	0.43	0.42	0.18	0.18	0.24	0.12	0.13	0.30
PB	316L	27	0.16	0.24	0.18	0.07	0.20	0.56	0.32	0.33	0.24	0.25	0.27	0.30
PB	316L	28	3.97	2.47	3.06	4.62	1.43	6.08	5.84	6.04	0.24	5.75	6.16	0.33
PB	316L	29	0.19	0.62	0.19	0.36	0.26	0.78	0.42	0.44	0.36	0.30	0.33	0.48
PB	316L	30	0.12	0.34	0.11	0.07	0.21	0.50	0.25	0.26	0.24	0.19	0.20	0.31
PC	316L	1	0.02	0.01	0.06	0.03	0.03	0.17	0.07	0.07	0.10	0.03	0.04	0.14
PC	316L	2	0.13	0.10	0.10	0.09	0.05	0.26	0.19	0.19	0.07	0.16	0.17	0.10
PC	316L	3	0.02	0.08	0.09	0.07	0.05	0.22	0.09	0.10	0.13	0.04	0.05	0.18
PC	316L	4	0.03	0.05	0.08	0.06	0.03	0.16	0.07	0.07	0.09	0.03	0.04	0.12
PC	316L	5	0.07	0.08	0.07	0.05	0.05	0.23	0.17	0.17	0.06	0.14	0.15	0.09
PC	316L	6	0.01	0.02	0.04	0.04	0.03	0.11	0.05	0.05	0.06	0.03	0.03	0.09
PC	316L	7	1.66	1.92	2.94	3.25	1.19	2.37	2.30	2.38	0.07	2.26	2.42	0.11
PC	316L	8	0.18	0.17	0.29	0.25	0.16	0.33	0.24	0.25	0.09	0.20	0.22	0.12
PC	316L	9	0.04	0.05	0.09	0.05	0.04	0.17	0.08	0.08	0.09	0.04	0.04	0.13
PC	316L	10	0.15	0.57	0.28	0.66	0.31	0.25	0.17	0.18	0.07	0.14	0.15	0.11
PC	316L	11	0.08	0.05	0.16	0.13	0.09	0.23	0.13	0.14	0.10	0.09	0.09	0.14
PC	316L	12	0.03	0.10	0.09	0.05	0.04							
PC	316L	13	0.02	0.04	0.07	0.04	0.03	0.15	0.06	0.06	0.08	0.03	0.03	0.12
PC	316L	14	0.49	1.07	1.29	1.16	0.40	1.10	1.01	1.05	0.09	0.94	1.02	0.15
PC	316L	15	0.06	0.30	0.09	0.15	0.14	0.21	0.10	0.11	0.11	0.06	0.06	0.15
PC	316L	16	0.04	0.07	0.07	0.06	0.03	0.17	0.07	0.07	0.10	0.03	0.04	0.14
PC	316L	17	0.25	0.05	0.06	0.07	0.07	0.39	0.34	0.35	0.05	0.32	0.34	0.08

PC	316L	18	2.13	2.47	4.46	4.52	1.60	2.62	2.53	2.61	0.09	2.48	2.66	0.14
PC	316L	19	0.04	0.02	0.07	0.03	0.03							
PC	316L	20	0.52	1.31	1.68	1.42	0.46	0.69	0.64	0.66	0.05	0.59	0.63	0.10
PC	316L	21	0.04	0.09	0.06	0.05	0.05	0.18	0.09	0.10	0.09	0.06	0.06	0.12
PC	316L	22	0.63	1.38	0.66	1.30	0.51	0.58	0.52	0.54	0.06	0.49	0.53	0.09
PC	316L	23	0.04	0.02	0.06	0.04	0.03	0.15	0.06	0.06	0.09	0.03	0.03	0.12
PC	316L	24	0.07	0.02	0.10	0.04	0.05	0.16	0.08	0.09	0.08	0.05	0.06	0.11
PC	316L	25	0.03	0.18	0.09	0.07	0.09	0.15	0.06	0.07	0.08	0.03	0.03	0.12
PC	316L													
PC	316L	27	0.36	0.61	0.90	1.34	0.48	0.64	0.51	0.53	0.13	0.45	0.48	0.18
PC	316L	28	0.03	0.12	0.05	0.08	0.05	0.16	0.07	0.08	0.09	0.04	0.04	0.12
PC	316L	29	0.06	0.17	0.07	0.13	0.08	0.18	0.09	0.09	0.09	0.06	0.06	0.12
PC	316L	30	0.03	0.12	0.03	0.08	0.05	0.10	0.05	0.05	0.05	0.03	0.03	0.07
PD	316L	1	0.26	0.20	0.36	0.15	0.22	0.75	0.48	0.49	0.27	0.41	0.44	0.34
PD	316L	2	0.04	0.01	0.07	0.02	0.03	0.58	0.29	0.30	0.29	0.17	0.18	0.41
PD	316L	3	0.02	0.01	0.10	0.02	0.05	0.73	0.29	0.31	0.43	0.14	0.15	0.59
PD	316L	4	0.11	0.01	0.06	0.09	0.05	0.60	0.30	0.32	0.30	0.24	0.25	0.37
PD	316L	5	0.02	0.01	0.07	0.02	0.03	0.63	0.26	0.27	0.36	0.14	0.15	0.49
PD	316L	6	0.02	0.02	0.08	0.03	0.03	0.50	0.19	0.20	0.31	0.09	0.10	0.41
PD	316L	7	0.01	0.02	0.05	0.01	0.03	0.45	0.13	0.14	0.32	0.05	0.06	0.40
PD	316L	8	0.21	0.07	0.15	0.14	0.08	0.67	0.35	0.37	0.32	0.23	0.24	0.44
PD	316L	9	0.05	0.02	0.08	0.03	0.03	0.55	0.23	0.23	0.32	0.13	0.14	0.42
PD	316L	10	0.66	0.26	0.12	0.25	0.22	1.57	1.29	1.33	0.29	1.19	1.27	0.38
PD	316L	11	1.24	0.38	1.16	0.78	0.60	2.69	2.46	2.55	0.23	2.36	2.53	0.33
PD	316L	12	0.10	0.02	0.08	0.05	0.04	0.65	0.29	0.30	0.36	0.16	0.17	0.49
PD	316L	13	0.03	0.01	0.07	0.04	0.03	0.61	0.22	0.23	0.39	0.09	0.10	0.52
PD	316L	14	0.02	0.01	0.06	0.03	0.03	0.51	0.18	0.19	0.34	0.09	0.10	0.42
PD	316L	15	0.03	0.02	0.09	0.02	0.04	0.50	0.22	0.23	0.28	0.12	0.13	0.38
PD	316L	16	0.09	0.03	0.14	0.04	0.09	0.69	0.40	0.41	0.29	0.30	0.32	0.40
PD	316L	17	0.01	0.00	0.03	0.01	0.02	0.46	0.17	0.18	0.29	0.10	0.10	0.36
PD	316L	18	0.03	0.02	0.06	0.04	0.02	0.63	0.27	0.28	0.36	0.14	0.15	0.49
PD	316L	19	0.05	0.02	0.07	0.06	0.03	0.46	0.20	0.21	0.26	0.11	0.11	0.36
PD	316L	20	0.03	0.06	0.07	0.07	0.02	0.33	0.15	0.15	0.18	0.10	0.10	0.23
PD	316L	21	0.67	0.78	1.31	1.67	0.77	1.60	1.32	1.37	0.28	1.24	1.33	0.36
PD	316L	22	0.04	0.02	0.06	0.04	0.03	0.72	0.32	0.33	0.40	0.17	0.19	0.55
PD	316L	23	0.04	0.01	0.04	0.02	0.02	0.49	0.19	0.20	0.29	0.11	0.12	0.38
PD	316L	24	0.16	0.09	0.13	0.12	0.06	0.75	0.39	0.41	0.36	0.28	0.30	0.47
PD	316L	25	0.04	0.01	0.06	0.05	0.03	0.57	0.25	0.26	0.32	0.13	0.14	0.44
PD	316L	26	0.05	0.01	0.07	0.03	0.03	0.68	0.32	0.33	0.36	0.19	0.20	0.50
PD	316L	27	0.02	0.01	0.03	0.02	0.02	0.57	0.30	0.31	0.27	0.24	0.25	0.33
PD	316L	28	0.04	0.01	0.05	0.02	0.02	0.53	0.24	0.25	0.29	0.15	0.16	0.38
PD	316L	29	0.02	0.01	0.04	0.02	0.02	0.47	0.20	0.21	0.27	0.12	0.13	0.34
PD	316L	30	0.11	0.06	0.12	0.12	0.06	0.54	0.34	0.35	0.20	0.28	0.30	0.26
PE	316L	1	0.16	0.13	0.16	0.38	0.16	0.83	0.49	0.50	0.35	0.34	0.36	0.49
PE	316L	2	0.18	0.40	0.20	0.24	0.11	0.95	0.61	0.63	0.35	0.47	0.51	0.48
PE	316L	3	0.03	0.04	0.08	0.06	0.03	0.61	0.29	0.30	0.31	0.17	0.18	0.44
PE	316L	4	0.04	0.05	0.10	0.05	0.04	0.82	0.37	0.38	0.44	0.18	0.19	0.63
PE	316L	5	0.07	0.09	0.10	0.08	0.06	0.64	0.29	0.31	0.35	0.16	0.18	0.48
PE	316L	6	0.53	0.06	0.09	0.07	0.16	1.20	0.97	1.01	0.23	0.87	0.94	0.33
PE	316L	7	0.06	0.04	0.10	0.04	0.03	0.64	0.30	0.31	0.34	0.18	0.19	0.47
PE	316L	8	0.02	0.04	0.08	0.02	0.04	0.64	0.29	0.30	0.35	0.17	0.18	0.47
PE	316L	9	0.03	0.10	0.06	0.04	0.07	0.63	0.31	0.32	0.32	0.20	0.22	0.43
PE	316L	10	0.04	0.20	0.08	0.06	0.12	0.69	0.35	0.36	0.34	0.21	0.23	0.47
PE	316L	11	0.08	0.05	0.07	0.04	0.03	0.75	0.45	0.46	0.31	0.35	0.37	0.41
PE	316L	12	0.02	0.03	0.06	0.02	0.03	0.58	0.27	0.28	0.31	0.15	0.16	0.43
PE	316L	13	0.05	0.25	0.09	0.11	0.13	0.80	0.37	0.39	0.43	0.18	0.19	0.62
PE	316L	14	0.12	0.12	0.14	0.17	0.09	0.78	0.43	0.45	0.35	0.30	0.32	0.48
PE	316L	15	0.02	0.03	0.06	0.03	0.02	0.48	0.22	0.23	0.26	0.12	0.13	0.35
PE	316L	16	0.10	0.13	0.10	0.07	0.08	0.67	0.40	0.41	0.27	0.29	0.32	0.38
PE	316L	17	0.02	0.03	0.08	0.02	0.03	0.61	0.27	0.28	0.34	0.14	0.15	0.47
PE	316L	18	0.04	0.01	0.09	0.03	0.04	0.70	0.33	0.34	0.37	0.19	0.20	0.51
PE	316L	19	0.10	0.42	0.14	0.25	0.22	0.65	0.37	0.39	0.28	0.28	0.30	0.37
PE	316L	20	0.04	0.04	0.08	0.05	0.03	0.65	0.32	0.33	0.34	0.19	0.20	0.47
PE	316L	21	0.03	0.04	0.05	0.03	0.03	0.66	0.40	0.42	0.26	0.31	0.33	0.35
PE	316L	22	0.03	0.11	0.11	0.06	0.08	0.51	0.19	0.20	0.32	0.08	0.09	0.43
PE	316L	23	0.02	0.01	0.07	0.03	0.03	0.55	0.22	0.23	0.33	0.09	0.10	0.46
PE	316L	24	0.10	0.10	0.17	0.20	0.09	0.57	0.26	0.26	0.31	0.14	0.15	0.42
PE	316L	25	0.15	0.71	0.14	0.22	0.38	0.58	0.34	0.35	0.24	0.26	0.28	0.32
PE	316L	26	0.08	0.18	0.10	0.07	0.11	0.55	0.26	0.27	0.29	0.14	0.15	0.41
PE	316L	27	0.09	0.40	0.13	0.19	0.22	0.87	0.46	0.47	0.42	0.30	0.32	0.58
PE	316L	28	0.01	0.07	0.05	0.02	0.05	0.53	0.25	0.26	0.28	0.16	0.17	0.37
PE	316L	29	0.01	0.05	0.06	0.02	0.04	0.47	0.22	0.23	0.25	0.13	0.14	0.34
PE	316L	30	0.02	0.05	0.08	0.03	0.04	0.48	0.22	0.23	0.25	0.11	0.12	0.36
PF	316L	1	0.08	0.00	0.00	0.00	0.00	0.79	0.37	0.39	0.41	0.19	0.20	0.60
PF	316L	2	0.16	0.00	0.00	0.00	0.00	0.60	0.26	0.27	0.34	0.16	0.17	0.45
PF	316L	3	0.28	0.48	0.27	0.83	0.35	1.09	0.73	0.75	0.36	0.57	0.62	0.52
PF	316L	4	0.03	0.06	0.10	0.04	0.05	0.72	0.31	0.32	0.42	0.13	0.14	0.59
PF	316L	5	0.04	0.04	0.13	0.04	0.06	0.73	0.37	0.38	0.36	0.20	0.22	0.53
PF	316L	6	0.05	0.02	0.12	0.03	0.06	0.60	0.27	0.27	0.33	0.14	0.15	0.46
PF	316L	7	0.02	0.03	0.06	0.04	0.03	0.58	0.27	0.28	0.31	0.15	0.16	0.42
PF	316L	8	0.04	0.07	0.09	0.04	0.05	0.70	0.33	0.34	0.37	0.16	0.17	0.53
PF	316L	9	0.04	0.10	0.08	0.04	0.06	0.66	0.30	0.31	0.35	0.18	0.20	0.47
PF	316L	10	0.05	0.18	0.10	0.11	0.07	0.82	0.41	0.43	0.41	0.23	0.25	0.59
PF	316L	11	0.18	0.15	0.22	0.16	0.10	1.06	0.64	0.66	0.42	0.45	0.48	0.61

PF	316L	12	0.02	0.09	0.05	0.05	0.05	0.57	0.19	0.20	0.38	0.07	0.08	0.50
PF	316L	13	0.03	0.01	0.08	0.05	0.04	0.55	0.23	0.24	0.31	0.12	0.13	0.43
PF	316L	14	0.02	0.06	0.07	0.05	0.03	0.52	0.19	0.20	0.32	0.08	0.09	0.43
PF	316L	15	0.30	0.16	0.25	0.41	0.16	0.92	0.60	0.63	0.32	0.45	0.48	0.47
PF	316L	16	0.46	0.33	0.50	0.24	0.31	1.41	1.11	1.15	0.30	0.97	1.04	0.44
PF	316L	17	0.03	0.01	0.10	0.05	0.05	0.66	0.32	0.34	0.33	0.16	0.17	0.50
PF	316L	18	0.03	0.03	0.08	0.04	0.03	0.77	0.35	0.36	0.42	0.14	0.15	0.63
PF	316L	19	0.03	0.07	0.07	0.05	0.04	0.58	0.26	0.27	0.32	0.12	0.12	0.46
PF	316L	20	0.03	0.07	0.08	0.03	0.05	0.57	0.27	0.28	0.30	0.13	0.13	0.44
PF	316L	21	0.16	0.12	0.14	0.17	0.05	0.91	0.57	0.59	0.34	0.46	0.49	0.45
PF	316L	22	0.03	0.04	0.08	0.04	0.03	0.76	0.35	0.36	0.41	0.17	0.18	0.59
PF	316L	23	0.15	0.50	0.22	0.59	0.24	0.93	0.55	0.57	0.38	0.41	0.44	0.52
PF	316L	24	0.03	0.16	0.08	0.06	0.08	0.52	0.18	0.19	0.33	0.08	0.09	0.43
PF	316L	25	0.09	0.13	0.19	0.19	0.11	0.73	0.39	0.41	0.34	0.23	0.25	0.50
PF	316L	26	0.04	0.01	0.08	0.04	0.03	0.59	0.26	0.27	0.33	0.16	0.17	0.43
PF	316L	27	0.04	0.12	0.06	0.08	0.06	0.53	0.25	0.26	0.29	0.14	0.15	0.40
PF	316L	28	0.04	0.06	0.09	0.07	0.04	0.55	0.26	0.27	0.29	0.12	0.13	0.43
PF	316L	29	0.03	0.06	0.08	0.04	0.03	0.58	0.26	0.27	0.32	0.15	0.16	0.43
PF	316L	30	0.36	0.05	0.09	0.13	0.13	0.98	0.71	0.74	0.27	0.63	0.68	0.34
PG	316L	1	0.02	0.03	0.11	0.03	0.05	0.59	0.20	0.21	0.38	0.08	0.09	0.50
PG	316L	2	0.04	0.01	0.13	0.08	0.06	0.72	0.34	0.35	0.38	0.19	0.21	0.52
PG	316L	3	0.04	0.06	0.11	0.04	0.04	0.95	0.45	0.46	0.50	0.22	0.23	0.74
PG	316L	4	0.07	0.04	0.07	0.07	0.03	0.60	0.28	0.29	0.32	0.20	0.21	0.40
PG	316L	5	0.06	0.06	0.10	0.04	0.04	0.75	0.35	0.36	0.40	0.19	0.21	0.55
PG	316L	6	0.33	0.76	0.21	1.24	0.68	1.31	0.91	0.94	0.40	0.74	0.80	0.57
PG	316L	7	0.18	0.57	0.16	0.56	0.28	1.02	0.61	0.63	0.41	0.44	0.48	0.57
PG	316L	8	0.09	0.54	0.13	0.27	0.32	0.80	0.40	0.42	0.40	0.26	0.28	0.54
PG	316L	9	0.05	0.05	0.08	0.04	0.03	0.69	0.35	0.36	0.35	0.23	0.24	0.47
PG	316L	10	0.04	0.08	0.08	0.05	0.05	0.72	0.32	0.33	0.40	0.15	0.16	0.56
PG	316L	11	0.03	0.02	0.08	0.03	0.03	0.75	0.34	0.35	0.41	0.18	0.19	0.57
PG	316L	12	0.05	0.02	0.08	0.06	0.03	0.58	0.26	0.27	0.32	0.13	0.14	0.45
PG	316L	13	0.04	0.02	0.08	0.03	0.03	0.61	0.27	0.28	0.34	0.15	0.16	0.46
PG	316L	14	0.03	0.45	0.07	0.13	0.29	0.52	0.18	0.19	0.33	0.10	0.10	0.42
PG	316L	15	0.06	0.11	0.11	0.07	0.06	0.68	0.29	0.31	0.38	0.15	0.17	0.52
PG	316L	16	0.12	0.27	0.16	0.13	0.14	0.94	0.53	0.55	0.42	0.36	0.39	0.58
PG	316L	17	0.07	0.02	0.12	0.05	0.05	0.84	0.42	0.44	0.42	0.22	0.23	0.63
PG	316L	18	0.56	0.49	0.50	0.74	0.33	1.42	1.04	1.08	0.38	0.88	0.94	0.54
PG	316L	19	0.02	0.03	0.06	0.02	0.03	0.60	0.26	0.27	0.33	0.14	0.15	0.45
PG	316L	20	0.03	0.07	0.07	0.04	0.04	0.71	0.33	0.34	0.39	0.16	0.17	0.56
PG	316L	21	0.02	0.01	0.06	0.02	0.02	0.72	0.29	0.30	0.43	0.12	0.13	0.60
PG	316L	22	0.02	0.02	0.05	0.02	0.02	0.53	0.21	0.22	0.32	0.11	0.12	0.41
PG	316L	23	0.03	0.02	0.07	0.04	0.03	0.58	0.24	0.25	0.34	0.13	0.14	0.44
PG	316L	24	0.02	0.02	0.08	0.04	0.04	0.60	0.23	0.24	0.38	0.10	0.11	0.50
PG	316L	25	0.06	0.35	0.07	0.13	0.19	0.85	0.40	0.41	0.45	0.21	0.23	0.64
PG	316L	26	0.12	0.37	0.27	0.23	0.21	0.80	0.48	0.49	0.33	0.38	0.41	0.42
PG	316L	27	0.20	0.09	0.42	0.21	0.28	0.88	0.54	0.56	0.34	0.41	0.44	0.47
PG	316L	28	0.05	0.11	0.08	0.05	0.07	0.59	0.25	0.26	0.34	0.14	0.15	0.45
PG	316L	29	0.04	0.10	0.08	0.07	0.06	0.66	0.28	0.29	0.39	0.12	0.13	0.54
PG	316L	30	0.05	0.06	0.09	0.04	0.04	0.65	0.32	0.33	0.33	0.19	0.20	0.47
PB	316H	1	0.04	0.04	0.15	0.05	0.09	0.46	0.20	0.21	0.25	0.08	0.08	0.38
PB	316H	2	2.43	1.85	1.72	4.60	1.79	2.89	2.69	2.79	0.20	2.58	2.77	0.31
PB	316H	3	0.03	0.31	0.12	0.05	0.24	0.36	0.15	0.16	0.21	0.06	0.06	0.30
PB	316H	4	0.03	0.04	0.14	0.02	0.07	0.50	0.23	0.24	0.27	0.09	0.10	0.40
PB	316H	5	0.04	0.09	0.15	0.04	0.08	0.59	0.27	0.28	0.32	0.11	0.12	0.48
PB	316H	6	0.02	0.04	0.12	0.03	0.06	0.40	0.17	0.18	0.23	0.06	0.06	0.34
PB	316H	7	0.06	0.09	0.15	0.04	0.09	0.48	0.22	0.23	0.26	0.10	0.10	0.39
PB	316H	8	0.07	0.08	0.15	0.06	0.06	0.48	0.23	0.24	0.24	0.11	0.12	0.37
PB	316H	9	0.07	0.02	0.14	0.08	0.07	0.68	0.36	0.37	0.32	0.17	0.19	0.50
PB	316H	10	0.09	0.30	0.07	0.19	0.14	1.45	0.94	0.98	0.51	0.55	0.60	0.90
PB	316H	11	0.17	0.99	0.43	0.29	0.53	0.73	0.41	0.43	0.32	0.24	0.26	0.49
PB	316H	12	0.04	0.19	0.12	0.06	0.11	1.00	0.55	0.57	0.45	0.25	0.27	0.75
PB	316H	13	0.07	0.06	0.10	0.13	0.06	0.23	0.11	0.12	0.12	0.06	0.06	0.17
PB	316H	14	0.04	0.15	0.14	0.06	0.08	0.94	0.50	0.52	0.43	0.22	0.24	0.71
PB	316H	15	0.03	0.20	0.08	0.05	0.15	0.75	0.37	0.38	0.38	0.16	0.17	0.59
PB	316H	16	0.02	0.06	0.09	0.03	0.05	0.30	0.13	0.13	0.18	0.04	0.05	0.26
PB	316H	17	0.04	0.03	0.08	0.04	0.04	0.20	0.08	0.08	0.12	0.03	0.03	0.17
PB	316H	18	0.72	0.83	0.79	1.62	0.83	1.13	0.88	0.91	0.25	0.75	0.81	0.38
PB	316H	19	0.88	0.30	0.50	0.93	0.39	0.85	0.67	0.70	0.18	0.57	0.62	0.28
PB	316H	20	0.04	0.10	0.07	0.04	0.08	0.45	0.20	0.21	0.24	0.08	0.09	0.36
PB	316H	21	0.02	0.06	0.08	0.04	0.05	0.27	0.11	0.11	0.16	0.04	0.04	0.23
PB	316H	22	0.03	0.13	0.10	0.05	0.08	0.59	0.27	0.28	0.31	0.10	0.11	0.48
PB	316H	23	2.92	1.31	0.96	1.95	1.19	3.73	3.53	3.66	0.20	3.41	3.66	0.32
PB	316H	24	0.04	0.33	0.17	0.07	0.22	0.65	0.32	0.33	0.33	0.13	0.14	0.52
PB	316H	25	0.17	0.06	0.12	0.21	0.08	0.24	0.15	0.16	0.09	0.11	0.12	0.13
PB	316H	26	0.02	0.01	0.08	0.03	0.04	0.16	0.07	0.07	0.09	0.03	0.03	0.13
PB	316H	27	0.01	0.05	0.08	0.02	0.06	0.17	0.06	0.07	0.10	0.02	0.02	0.15
PB	316H	28	0.28	0.82	0.37	1.31	0.49	0.86	0.52	0.54	0.34	0.33	0.35	0.54
PB	316H	29	0.08	0.57	0.22	0.16	0.38	1.12	0.68	0.71	0.44	0.36	0.39	0.76
PB	316H	30	0.02	0.18	0.08	0.04	0.15	0.40	0.17	0.17	0.23	0.06	0.07	0.33
PC	316H	1	0.53	0.08	0.28	0.12	0.20	0.78	0.54	0.56	0.23	0.42	0.45	0.35
PC	316H	2	0.07	0.06	0.09	0.04	0.04	0.32	0.16	0.17	0.16	0.09	0.09	0.23
PC	316H	3	0.09	0.20	0.31	0.17	0.18	0.45	0.23	0.24	0.22	0.13	0.14	0.32
PC	316H	4	0.04	0.06	0.13	0.04	0.07	0.42	0.19	0.20	0.23	0.08	0.08	0.34
PC	316H	5	0.09	0.06	0.07	0.06	0.05	0.29	0.15	0.16	0.14	0.09	0.10	0.19

PC	316H	6	0.60	0.60	0.69	0.67	0.56	0.58	0.44	0.46	0.13	0.38	0.41	0.20
PC	316H	7	0.55	0.43	1.57	0.63	1.03	1.25	0.84	0.88	0.40	0.62	0.67	0.63
PC	316H	8	0.02	0.06	0.06	0.03	0.03	0.64	0.29	0.30	0.35	0.11	0.12	0.53
PC	316H	9	0.05	0.12	0.10	0.04	0.11	0.45	0.20	0.21	0.25	0.09	0.09	0.36
PC	316H	10	0.30	0.73	1.16	1.32	0.60	0.53	0.36	0.37	0.17	0.28	0.30	0.25
PC	316H	11	1.04	0.60	0.77	1.50	0.69	1.09	0.94	0.97	0.15	0.86	0.92	0.23
PC	316H	12	0.04	0.09	0.10	0.06	0.05	0.79	0.40	0.42	0.39	0.17	0.18	0.62
PC	316H	13	0.05	0.06	0.19	0.04	0.09	0.32	0.16	0.16	0.17	0.08	0.08	0.25
PC	316H	14	0.77	1.50	1.87	1.48	0.40	0.90	0.82	0.85	0.08	0.76	0.81	0.14
PC	316H	15	0.05	0.38	0.11	0.08	0.24	0.80	0.41	0.42	0.40	0.17	0.18	0.63
PC	316H	16	0.03	0.06	0.12	0.03	0.07	0.43	0.19	0.19	0.24	0.07	0.08	0.36
PC	316H	17	0.10	0.04	0.10	0.09	0.04	0.19	0.12	0.13	0.07	0.09	0.09	0.10
PC	316H	18	0.55	1.19	1.47	2.30	0.91	1.19	0.81	0.84	0.38	0.60	0.65	0.59
PC	316H	19	0.06	0.03	0.13	0.06	0.05	0.30	0.15	0.15	0.15	0.07	0.08	0.23
PC	316H	20	0.57	1.56	1.91	1.57	0.45	0.65	0.60	0.62	0.05	0.56	0.60	0.09
PC	316H	21	0.03	0.09	0.10	0.05	0.07	0.60	0.28	0.29	0.32	0.12	0.13	0.48
PC	316H	22	0.06	0.48	0.12	0.20	0.27	0.49	0.23	0.24	0.26	0.11	0.12	0.38
PC	316H	23	0.08	0.05	0.28	0.21	0.17	0.45	0.22	0.23	0.23	0.10	0.11	0.35
PC	316H	24	0.99	0.81	1.39	2.00	1.15	0.98	0.82	0.85	0.16	0.74	0.80	0.24
PC	316H	25	0.03	0.11	0.10	0.04	0.08	0.41	0.18	0.19	0.23	0.07	0.08	0.33
PC	316H	26	0.02	0.03	0.09	0.04	0.05	0.22	0.09	0.09	0.13	0.03	0.03	0.19
PC	316H	27	0.17	0.45	0.15	1.03	0.44	1.19	0.70	0.73	0.48	0.40	0.43	0.79
PC	316H	28	0.03	0.13	0.10	0.06	0.08	0.39	0.17	0.18	0.21	0.07	0.08	0.31
PC	316H	29	0.03	0.05	0.09	0.02	0.04	0.46	0.23	0.23	0.24	0.10	0.11	0.36
PC	316H	30	0.02	0.05	0.08	0.04	0.05	0.20	0.08	0.08	0.12	0.03	0.03	0.17
PD	316H	1	2.53	1.57	1.41	4.09	1.67	2.76	2.53	2.63	0.23	2.41	2.60	0.36
PD	316H	2	0.07	0.57	0.11	0.12	0.44	1.19	0.68	0.71	0.52	0.33	0.36	0.86
PD	316H	3	0.12	0.04	0.16	0.07	0.08	0.59	0.30	0.31	0.29	0.16	0.17	0.43
PD	316H	4	0.04	0.08	0.09	0.04	0.05	1.05	0.56	0.58	0.50	0.25	0.27	0.80
PD	316H	5	0.06	0.06	0.13	0.03	0.07	0.62	0.30	0.31	0.32	0.14	0.15	0.48
PD	316H	6	0.28	0.14	0.13	0.30	0.11	0.34	0.23	0.24	0.11	0.18	0.19	0.16
PD	316H	7	0.52	0.98	0.59	1.43	0.85	0.87	0.64	0.66	0.23	0.52	0.56	0.35
PD	316H	8	0.02	0.07	0.12	0.04	0.06	0.65	0.29	0.30	0.35	0.11	0.12	0.54
PD	316H	9	0.04	0.05	0.07	0.04	0.04	0.54	0.24	0.25	0.30	0.11	0.11	0.43
PD	316H	10	0.03	0.18	0.09	0.05	0.11	0.82	0.39	0.41	0.43	0.16	0.17	0.66
PD	316H	11	0.04	0.06	0.13	0.04	0.07	0.40	0.17	0.18	0.22	0.07	0.07	0.33
PD	316H	12	0.23	0.13	0.16	0.18	0.09	0.50	0.28	0.29	0.22	0.18	0.19	0.32
PD	316H	13	0.05	0.24	0.07	0.06	0.15	1.24	0.70	0.73	0.54	0.34	0.37	0.90
PD	316H	14	1.75	1.42	1.23	3.41	1.42	2.10	1.88	1.95	0.22	1.76	1.90	0.33
PD	316H	15	0.26	0.03	0.15	0.26	0.11	0.47	0.28	0.29	0.18	0.20	0.21	0.27
PD	316H	16	0.03	0.05	0.10	0.04	0.05	0.61	0.27	0.28	0.34	0.10	0.11	0.51
PD	316H	17	0.05	0.05	0.12	0.06	0.06	0.52	0.24	0.25	0.28	0.10	0.11	0.42
PD	316H	18	0.70	0.44	0.74	1.72	0.77	1.25	0.94	0.98	0.30	0.78	0.85	0.46
PD	316H	19	0.05	0.57	0.12	0.14	0.37	0.60	0.27	0.28	0.33	0.10	0.11	0.50
PD	316H	20	0.03	0.05	0.09	0.03	0.04	0.84	0.41	0.43	0.43	0.16	0.18	0.67
PD	316H	21	0.03	0.10	0.07	0.03	0.08	0.32	0.13	0.14	0.19	0.05	0.05	0.28
PD	316H	22	0.04	0.04	0.14	0.06	0.07	0.43	0.19	0.20	0.24	0.07	0.08	0.36
PD	316H	23	0.34	0.06	0.62	0.59	0.44	0.75	0.46	0.48	0.29	0.31	0.34	0.43
PD	316H	24	1.08	1.51	1.47	3.33	1.58	1.18	1.04	1.08	0.14	0.96	1.04	0.22
PD	316H	25	0.06	0.43	0.10	0.10	0.29	0.48	0.23	0.24	0.25	0.10	0.11	0.38
PD	316H	26	0.04	0.11	0.09	0.04	0.08	0.47	0.21	0.22	0.27	0.08	0.09	0.39
PD	316H	27	0.10	0.94	0.13	0.41	0.77	1.14	0.65	0.68	0.49	0.34	0.37	0.80
PD	316H	28	0.03	0.05	0.06	0.07	0.04	0.26	0.11	0.11	0.15	0.05	0.05	0.21
PD	316H	29	0.05	0.11	0.06	0.06	0.07	0.33	0.14	0.14	0.19	0.06	0.06	0.28
PD	316H	30	0.05	0.10	0.07	0.03	0.07	0.55	0.25	0.26	0.30	0.10	0.11	0.44
PE	316H	1	0.02	0.07	0.10	0.02	0.06	0.27	0.10	0.11	0.17	0.04	0.04	0.24
PE	316H	2	0.13	0.03	0.14	0.09	0.06	0.34	0.18	0.18	0.16	0.10	0.11	0.24
PE	316H	3	0.08	0.03	0.16	0.04	0.09	0.64	0.31	0.32	0.33	0.13	0.14	0.51
PE	316H	4	0.35	0.02	0.16	0.20	0.12	0.34	0.26	0.27	0.08	0.22	0.23	0.13
PE	316H	5	0.03	0.02	0.10	0.02	0.06	0.34	0.14	0.14	0.20	0.05	0.05	0.29
PE	316H	6	0.03	0.02	0.07	0.02	0.03	0.84	0.41	0.43	0.43	0.17	0.18	0.68
PE	316H	7	0.02	0.02	0.11	0.02	0.06	0.30	0.13	0.13	0.17	0.04	0.05	0.26
PE	316H	8	1.39	0.67	0.57	1.25	0.61	1.27	1.09	1.13	0.18	1.00	1.07	0.27
PE	316H	9	0.03	0.03	0.10	0.04	0.04	0.75	0.36	0.38	0.39	0.14	0.15	0.61
PE	316H	10	0.03	0.08	0.07	0.04	0.04	0.81	0.39	0.41	0.42	0.16	0.17	0.65
PE	316H	11	0.02	0.17	0.11	0.04	0.12	0.40	0.18	0.18	0.22	0.07	0.08	0.33
PE	316H	12	0.10	0.01	0.17	0.04	0.09	0.37	0.19	0.19	0.19	0.09	0.10	0.28
PE	316H	13	0.33	0.03	0.13	0.09	0.10	0.65	0.39	0.41	0.25	0.26	0.28	0.38
PE	316H	14	0.13	0.03	0.10	0.07	0.05	0.38	0.19	0.20	0.19	0.11	0.11	0.27
PE	316H	15	0.05	0.02	0.09	0.03	0.05	0.41	0.18	0.19	0.23	0.07	0.08	0.34
PE	316H	16	0.02	0.04	0.08	0.03	0.04	0.49	0.22	0.22	0.28	0.08	0.08	0.41
PE	316H	17	0.17	0.10	0.32	0.17	0.21	0.25	0.15	0.15	0.11	0.11	0.11	0.15
PE	316H	18	0.04	0.03	0.08	0.03	0.04	1.06	0.57	0.60	0.49	0.26	0.28	0.81
PE	316H	19	0.02	0.02	0.10	0.02	0.05	0.27	0.11	0.12	0.16	0.04	0.04	0.23
PE	316H	20	0.02	0.06	0.09	0.03	0.05	0.32	0.14	0.14	0.18	0.05	0.05	0.27
PE	316H	21	0.17	0.35	0.37	0.60	0.22	0.72	0.38	0.40	0.34	0.21	0.23	0.50
PE	316H	22	0.03	0.02	0.10	0.02	0.05	0.66	0.31	0.32	0.35	0.12	0.13	0.54
PE	316H	23	0.01	0.02	0.05	0.01	0.03	0.21	0.07	0.08	0.14	0.02	0.02	0.19
PE	316H	24	1.32	0.61	0.94	1.33	0.75	1.45	1.28	1.33	0.16	1.20	1.29	0.25
PE	316H	25	0.03	0.02	0.12	0.02	0.06	0.56	0.25	0.26	0.31	0.09	0.10	0.47
PE	316H	26	0.03	0.03	0.10	0.03	0.04	0.46	0.21	0.22	0.25	0.08	0.09	0.38
PE	316H	27	0.01	0.05	0.05	0.02	0.03	0.11	0.04	0.04	0.07	0.01	0.01	0.10
PE	316H	28	0.01	0.01	0.09	0.02	0.05	0.28	0.11	0.12	0.17	0.03	0.04	0.25
PE	316H	29	0.01	0.02	0.06	0.02	0.03	0.28	0.11	0.11	0.17	0.03	0.04	0.25

PE	316H	30	0.01	0.00	0.04	0.02	0.02	0.12	0.04	0.05	0.08	0.02	0.02	0.10
PF	316H	1	0.02	0.02	0.15	0.02	0.09	0.20	0.08	0.08	0.12	0.03	0.03	0.17
PF	316H	2	0.09	0.56	0.13	0.16	0.38	0.30	0.17	0.18	0.12	0.12	0.12	0.18
PF	316H	3	0.10	0.19	0.20	0.23	0.13	0.21	0.11	0.11	0.10	0.07	0.07	0.14
PF	316H	4	0.02	0.08	0.10	0.03	0.06	0.33	0.14	0.14	0.19	0.06	0.06	0.27
PF	316H	5	0.02	0.06	0.14	0.04	0.07	0.29	0.13	0.13	0.16	0.06	0.06	0.23
PF	316H	6	0.03	0.06	0.10	0.03	0.07	0.14	0.07	0.07	0.07	0.04	0.04	0.10
PF	316H	7	0.01	0.04	0.05	0.02	0.03	0.11	0.04	0.04	0.07	0.02	0.02	0.09
PF	316H	8	0.02	0.06	0.09	0.03	0.05	0.22	0.09	0.10	0.12	0.04	0.04	0.18
PF	316H	9	0.02	0.08	0.10	0.02	0.07	0.17	0.08	0.08	0.10	0.03	0.04	0.14
PF	316H	10	0.18	0.43	0.15	0.46	0.21	0.58	0.33	0.35	0.25	0.22	0.24	0.36
PF	316H	11	1.09	0.62	1.54	0.74	0.94	1.28	1.08	1.12	0.20	0.99	1.06	0.29
PF	316H	12	0.02	0.07	0.08	0.05	0.05	0.23	0.09	0.09	0.14	0.03	0.04	0.19
PF	316H	13	0.01	0.05	0.12	0.02	0.08	0.14	0.05	0.06	0.08	0.02	0.02	0.12
PF	316H	14	0.02	0.07	0.10	0.03	0.07	0.18	0.07	0.07	0.11	0.03	0.03	0.16
PF	316H	15	0.01	0.01	0.06	0.03	0.03	0.10	0.03	0.04	0.07	0.01	0.01	0.09
PF	316H	16	1.76	1.28	2.34	1.70	1.45	2.04	1.97	2.04	0.07	1.93	2.07	0.11
PF	316H	17	0.01	0.01	0.07	0.02	0.03	0.20	0.07	0.07	0.13	0.02	0.02	0.18
PF	316H	18	0.02	0.04	0.08	0.03	0.03	0.36	0.15	0.16	0.21	0.05	0.06	0.30
PF	316H	19	0.02	0.10	0.06	0.04	0.06	0.19	0.08	0.08	0.11	0.03	0.04	0.16
PF	316H	20	0.01	0.08	0.06	0.03	0.06	0.12	0.05	0.05	0.07	0.02	0.02	0.10
PF	316H	21	1.29	1.08	1.63	1.20	0.81	1.45	1.34	1.39	0.11	1.30	1.39	0.16
PF	316H	22	0.03	0.12	0.10	0.08	0.07	0.33	0.14	0.14	0.19	0.05	0.06	0.27
PF	316H	23	1.56	2.80	1.71	4.94	1.74	1.56	1.43	1.48	0.13	1.37	1.47	0.19
PF	316H	24	0.03	0.20	0.07	0.09	0.12	0.19	0.08	0.08	0.11	0.04	0.04	0.15
PF	316H	25	0.02	0.05	0.06	0.04	0.03	0.15	0.05	0.05	0.09	0.02	0.02	0.13
PF	316H	26	0.02	0.04	0.09	0.03	0.04	0.12	0.05	0.06	0.07	0.03	0.03	0.10
PF	316H	27	0.04	0.13	0.08	0.12	0.06	0.15	0.08	0.08	0.07	0.05	0.05	0.10
PF	316H	28	0.04	0.10	0.09	0.03	0.07	0.18	0.09	0.09	0.09	0.05	0.06	0.13
PF	316H	29	0.02	0.11	0.09	0.07	0.07	0.22	0.10	0.10	0.12	0.04	0.05	0.18
PF	316H	30	0.06	0.08	0.04	0.04	0.06	0.13	0.08	0.08	0.05	0.06	0.06	0.08
PG	316H	1	0.02	0.05	0.14	0.02	0.08	0.29	0.12	0.13	0.17	0.04	0.05	0.25
PG	316H	2	0.02	0.01	0.12	0.04	0.06	0.21	0.09	0.09	0.13	0.03	0.03	0.18
PG	316H	3	0.03	0.11	0.10	0.04	0.07	0.66	0.31	0.32	0.35	0.12	0.13	0.53
PG	316H	3	0.02	0.05	0.08	0.03	0.05	0.13	0.07	0.07	0.06	0.04	0.05	0.09
PG	316H	4	0.05	0.03	0.06	0.02	0.03	0.27	0.12	0.12	0.16	0.04	0.05	0.23
PG	316H	4	0.06	0.51	0.13	0.16	0.32	0.49	0.38	0.39	0.11	0.33	0.35	0.16
PG	316H	5	0.02	0.06	0.12	0.03	0.07	0.79	0.53	0.55	0.26	0.41	0.44	0.38
PG	316H	5	0.02	0.08	0.09	0.04	0.05	0.41	0.19	0.19	0.22	0.09	0.09	0.32
PG	316H	6	0.48	0.51	0.73	0.82	0.52	0.21	0.09	0.10	0.12	0.04	0.04	0.18
PG	316H	7	0.40	1.06	0.39	1.48	0.63	0.28	0.12	0.13	0.16	0.05	0.05	0.23
PG	316H	8	0.05	0.39	0.14	0.18	0.23	0.40	0.18	0.18	0.22	0.07	0.07	0.33
PG	316H	9	0.02	0.05	0.11	0.04	0.04	0.17	0.06	0.07	0.10	0.02	0.02	0.15
PG	316H	9	0.02	0.02	0.08	0.04	0.04	0.19	0.07	0.07	0.12	0.02	0.02	0.16
PG	316H	10	0.02	0.12	0.12	0.04	0.10	0.29	0.14	0.15	0.15	0.08	0.08	0.22
PG	316H	11	0.03	0.06	0.11	0.03	0.05	0.32	0.13	0.14	0.19	0.05	0.05	0.28
PG	316H	16	0.76	0.46	1.06	0.58	0.68	1.22	0.91	0.94	0.31	0.75	0.81	0.46
PG	316H	17	0.01	0.02	0.07	0.03	0.03	0.25	0.10	0.10	0.16	0.03	0.03	0.22
PG	316H	18	0.10	0.16	0.23	0.20	0.16	0.22	0.12	0.12	0.10	0.07	0.08	0.15
PG	316H	20	0.02	0.07	0.09	0.06	0.04	0.27	0.11	0.11	0.16	0.04	0.04	0.23
PG	316H	21	0.02	0.07	0.11	0.03	0.07	0.50	0.21	0.22	0.29	0.07	0.08	0.42
PG	316H	22	0.02	0.03	0.07	0.02	0.04	0.34	0.14	0.15	0.20	0.05	0.05	0.29
PG	316H	22	0.01	0.05	0.07	0.02	0.04	0.13	0.05	0.05	0.08	0.02	0.02	0.11
PG	316H	23	0.01	0.07	0.06	0.03	0.05	0.15	0.06	0.06	0.09	0.02	0.02	0.13
PG	316H	24	0.02	0.02	0.10	0.02	0.05	0.21	0.09	0.09	0.13	0.03	0.03	0.18
PG	316H	25	0.07	0.39	0.12	0.18	0.21	0.78	0.40	0.42	0.38	0.19	0.21	0.58
PG	316H	26	0.31	0.81	0.92	0.97	0.50	0.47	0.35	0.37	0.12	0.30	0.33	0.17
PG	316H	27	0.02	0.03	0.06	0.05	0.02	0.13	0.05	0.05	0.08	0.02	0.02	0.11
PG	316H	28	0.02	0.14	0.10	0.08	0.09	0.19	0.08	0.08	0.11	0.04	0.04	0.15
PG	316H	29	0.02	0.14	0.09	0.08	0.10	0.33	0.14	0.14	0.19	0.05	0.06	0.28
PG	316H	30	0.02	0.08	0.11	0.04	0.06	0.19	0.09	0.09	0.10	0.04	0.04	0.15